Integrated Detector Arrays
for High Resolution Far-Infrared Imaging

Thesis by
Dean Paul Neikirk

In Partial Fulfillment of the Requirements
for the Degree of
Doctor of Philosophy

California Institute of Technology
Pasadena, California

1984

(Submitted October 31, 1983)

Acknowledgments

It is difficult to acknowledge all those people who make a thesis such as this possible. First, I would like to thank my advisor, David Rutledge, for providing me direction when I most needed it, and leaving me to find my own way whenever possible. It would have been very difficult to find a person with whom I could have worked better. From my pre-Tech years at OSU, I would like to thank Dr. Jim Choike for providing an excellent role model, and showing true enthusiasm for the teaching profession. I am also deeply indebted to Dr. N.C. Luhmann and his group at UCLA, specifically Tony Peebles, Hyeon Park, and Peter Young, for their assistance in making all the far-infrared measurements, and providing equipment and support at Caltech. In the construction of my various Rube Goldberg contraptions, I would like to thank the CES shop, without whom nothing would have been built. And to AZ, to whom I owe my present position, my heartfelt thanks.

To all those that contributed a little bit of non-technical life to my tenure in Steele, I am grateful: to the front office, Linda and Cindy, who really keep things moving; to our secretary Joyce, for her southern accent and outlook, that made me feel at home; and to Dale, Dave, and Robb Rutledge, who with their construction projects helped keep me in contact with my previous occupation. I would also like to recognize the folks from the sub-basement of Noyes, who helped form my first impressions of Caltech. And finally, to my parents and family, for their support over the years.

Integrated Detector Arrays
for High Resolution Far-Infrared Imaging

Abstract

Imaging systems designed to operate in the millimeter and submillimeter portion of the spectrum (often referred to as the far-infrared) require the development of focal plane detector arrays to simplify their construction. In this study the general characteristics of an antenna array intended to provide diffraction limited imaging are discussed. Two line-imaging bow-tie antenna arrays utilizing the hyperhemispherical substrate lens optical system and operating at 1.22mm and 119μm, are demonstrated. Two new far-infrared detectors, the bismuth air-bridge microbolometer and the bismuth-antimony microthermocouple, have been used with these arrays. Thermal models and performance data for these detectors are given. Finally, the photolithographic processes used to fabricate the detectors and antennas are discussed.

Contents

Chapter 1

Far-Infrared Sources and Detectors

In the last 10-15 years a great deal of effort has been applied to the development of millimeter and submillimeter receivers. Even today, the spectral region between roughly 100μm and 1mm has remained largely unexplored. The interest in this region, however, is quite high. In fusion research, the measurement of electron density, electron temperature, and magnetic field is most easily made through the use of submillimeter-waves [1]. For radar and surveillance, millimeter-waves penetrate smoke and haze better than the near-infrared, and, because of their shorter wavelength, could provide much higher resolution than conventional radar. In astronomy, some very exciting discoveries have just been made with the Infrared Astronomy Satellite (IRAS), which makes its observations in the 10-100μm range [2].

Workers in the far-infrared (FIR) portion of the spectrum have faced two serious problems: the lack of both reasonably powerful sources of radiation, and a sensitive means to detect them. The discovery of a far-infrared laser in 1964 by Crocker et al [3], followed by the development of cw FIR lasers by Chang and Bridges in 1970 [4][5], has done much to eliminate the first problem. Further work on these CO_2-pumped gas lasers [6] has led to a convenient, reliable, and powerful source of radiation throughout the FIR; by 1976, a review article listed laser activity in twenty-six polar gases, producing over 525 laser wavelengths, from 34.26μm to 1.96534mm [7]. Several other types of sources are now available [8], and research in this area is quite active.

The detection of millimeter and submillimeter-waves has also proved to be a challenge. The extension of classical microwave technology to these shorter wavelengths has been quite useful, but above 300GHz the increasing loss and mechanical complexity of metallic waveguide makes their application difficult. For wavelengths longer than 100μm, photodetectors based on the quantized absorption of photons are largely impractical, since the photon energies are so low (12.4meV for a 100μm photon). A hybrid technology using ideas from both the optical and microwave ends of the spectrum is appropriate in the FIR: a quasi-optical collection system (i.e. lenses or mirrors) coupled to planar antennas with integrated detectors [9][10][11][12]. The planar antennas have proved to be quite different from their low frequency counterparts [13][14][15]. The integrated detectors are also fairly unusual, ranging from superconducting tunnel junctions [16][17][18], to small area planar Schottky diodes [10][19], to microbolometers [20]. Much research and development remains to be done on these detectors, their antenna-coupling structures, and the associated optical systems.

Almost all the work done thus far on planar antennas and detectors has involved a single element. In many applications, however, a complete image of an extended object would be desired. With a single focal plane detector this can only be done by scanning the optical system. This technique is well established in the FIR: Hollinger et al [21] have developed a scanning system for 90GHz, and many other systems have also been designed and implemented (for example, ref. 22, 23, 24). Scanning systems, however, cannot image rapidly moving objects or changing scenes since they see only one point at a time. In plasma interferometry, for example, the time evolution of the electron density on a microsecond time scale is of interest, requiring that the entire image be scanned at a 100kHz-1MHz rate. Integration to improve signal-to-noise when scenes are static is also often restricted, because the total time to form the image is the product of the number of image points and the individual integration time at each point. An attractive solution in these cases would be an array of detectors and associated antennas arranged so that scanning is either unnecessary or considerably reduced. Such an antenna array would be placed in the image plane of an optical system, acting as the 'film' for a far-infrared camera.

A fairly limited amount of work has been done on imaging arrays for millimeter and submillimeter use. Gillespie and Phillips [25] proposed an array of feed horns to be placed in the focal plane of a parabolic reflector, and discussed the advantages of such a system for astronomical observations. Yngvesson et al [26] have discussed the possible aperture efficiencies in prime-focus-fed paraboloids in conjunction with an array of various planar feed elements: twin-dipoles, Vivaldis, and slots. Parrish et al [11] have made a resonant twin-dipole antenna, and using a GaAs beamlead diode, measured its pattern at 132GHz. They have also proposed the use of such an antenna as an imaging array element.

The need for a high resolution imaging system operating in the far-infrared has been the driving force behind this study. The general characteristics necessary for diffraction limited imaging are discussed in the first section of Chapter 2. Chapter 2 also describes a particular imaging system using the hyperhemispherical substrate lens, which takes advantage of the unique properties of dielectric-supported antennas. The first successful demonstrations of line-imaging systems, operating at 1.22mm and 119μm, conclude Chapter 2.

Chapter 3 is devoted to a discussion of a particularly useful far-infrared detector, the bismuth microbolometer. This is a thermal detector that can be easily integrated with an antenna, providing sensitive video detection and reasonably high speed. Two new variations on the basic microbolometer have been developed: the air-bridge microbolometer, which has substantially improved the sensitivity of the bolometer; and the bismuth-antimony microthermocouple, which allows the sensitivity of the microbolometer to be maintained at low modulation frequencies. Thermal models describing the operation of these detectors are also given.

Finally, Chapter 4 presents work on a particular integrated-circuit fabrication technique: lift-off patterning. This process is essential in the production of these planar antennas and detectors. The special lithographic preparation of patterns is discussed, including: chlorobenzene-modified photoresist; back-side flood-exposure technique for transparent substrates; plasma-formed fluorocarbon layers on photoresist; and multi-layer resist structures.

References

[1] N.C. Luhmann, Jr., 'Instrumentation and techniques for plasma diagnostics: an overview,' in **Infrared and Millimeter Waves, Vol. 2** (K.J. Button, ed., Academic Press, New York, 1979).

[2] J. Eberhart, 'Vega and co.: what's being born out there?' Science News **124**, 116 (1983).

[3] A. Crocker, H.A. Gebbie, M.F. Kimmitt, and L.E.S. Mathias, 'Stimulated emission in the far infra-red,' Nature **201**, 250 (1964).

[4] T.Y. Chang and T.J. Bridges, 'Laser action at 452, 496, and 541μm in optically pumped CH_3F,' Optics Comm. **1**, 423 (1970).

[5] T.Y. Chang, T.J. Bridges, and E.G. Burkhardt, 'cw submillimeter laser action in optically pumped methyl fluoride, methyl alcohol, and vinyl chloride gases,' Appl. Phys. Lett. **17**, 249 (1970).

[6] D.T. Hodges, F.B. Foote, and R.D. Reel, 'Efficient high-power operation of the cw far-infrared waveguide laser,' Appl. Phys. Lett. **29**, 662 (1976).

[7] M. Rosenbluh, R.J. Temkin, and K.J. Button, 'Submillimeter laser wavelength tables,' Applied Optics **15**, 2635 (1976).

[8] K.J. Button, ed., **Infrared and Millimeter Waves: Vol. 1, Sources of Radiation** (Academic Press, New York, 1979).

[9] D.B. Rutledge and S.E. Schwarz, 'Planar multimode detector arrays for infrared millimeter-wave applications,' IEEE J. Quantum Electron. **QE-17**, 407 (1981).

[10] B.J. Clifton, G.D. Alley, R.A. Murphy, and I.H. Mroczkowski, 'High-performance quasi-optical GaAs monolithic mixer at 110GHz,' IEEE Trans. Electron Devices **28**,155 (1981).

[11] P.T. Parrish, T.C.L.G. Sollner, R.H. Matthews, H.R. Fetterman, C.D. Parker, P.E. Tannenwald, and A.G. Cardiasmenos, 'Printed dipole-Schottky diode millimeter wave antenna array,' SPIE Proceedings Vol. 337, Millimeter Wave Technology, May 6-7, 1982.

[12] C. Yao, S.E. Schwarz, and B.J. Blumenstock, 'Monolithic integration of a dielectric millimeter-wave antenna and mixer diode: an embrionic millimeter-wave IC,' IEEE Trans. Microwave Theory Tech. **30**, 1241 (1982).

[13] C.R. Brewitt-Taylor, D.J. Gunton, and H.D. Rees, 'Planar antennas on a dielectric surface,' Electron Lett. **17**, 729 (1981).

[14] N. Engheta, C.H. Papas, and C. Elachi, 'Radiation

patterns of interfacial dipole antennas,' Radio Science **17**, 1557 (1982).

[15] D.B. Rutledge, D.P. Neikirk, and D.P. Kasilingam, 'Integrated-Circuit Antennas,' in **Infrared and Millimeter Waves**, Vol. 10 (K.J. Button, ed., Academic Press, New York, 1983).

[16] G.J. Dolan, T.G. Phillips, and D.P. Woody, 'Low-noise 115-GHz mixing in superconducting oxide-barrier tunnel junctions,' Appl. Phys. Lett. **34**, 347 (1979).

[17] W.C. Danchi, F. Habbal, and M. Tinkham, 'ac Josephson effect in small area superconducting tunnel junctions at 604Ghz,' Appl. Phys. Lett. **41**, 883 (1982).

[18] K.E. Irwin, S.E. Schwarz, and T. Van Duzer, 'Planar antenna-coupled SIS devices for detection and mixing,' 6th Int. Conf. Infrared Millimeter Waves, IEEE cat. no. 81CH1645-1 MTT, M-4-2 (1981).

[19] Z. Rav-Noy, C.-E. Zah, U. Shreter, D.B. Rutledge, T.-C. Wang, S.E. Schwarz, and T.F. Kuech, 'Monolithic Schottky diode imaging arrays at 94GHz,' Int. Conf. Infrared Millimeter Waves, Dec. 12-17, 1983.

[20] T.-L. Hwang, S.E. Schwarz, and D.B. Rutledge, 'Microbolometers for infrared detection,' Appl. Phys. Lett. **34**, 773 (1979).

[21] J.P. Hollinger, J.E. Kenney, and B.E. Troy Jr., 'A versatile millimeter-wave imaging system,' IEEE Trans. Microwave Theory Tech. **MTT-24**, 786 (1976).

[22] D.T. Hodges, F.B. Foote, E.E. Reber, and R.L.

Schellenbaum, 'Near-millimeter wave radiometric imaging,' 4th Int. Conf. Infrared Millimeter Waves Their Appl., IEEE Cat. No. 79CH1384-7 MTT, 51 (1979)

[23] J. Waldman, H.R. Fetterman, P.E. Duffy, T.G. Bryant, and P.E. Tannenwald, 'Submillimeter model measurements and their applications to millimeter radar systems,' 4th Int. Conf. Infrared Millimeter Waves Their Appl., IEEE Cat. No. 79CH1384-7 MTT, 49 (1979).

[24] J.A. Gagliano and J.J. McSheehy, 'Airborne millimeter wave radiometer for 94/183GHz high altitude atmospheric measurements,' 6th Int. Conf. Infrared Millimeter Waves, IEEE Cat. No. 81CH1645-1 MTT, Th-4-6 (1981).

[25] A.R. Gillespie and T.G. Phillips, 'Array detectors for millimetre line astronomy,' Astron. Astrophys. 73, 14 (1979).

[26] K.S. Yngvesson, T.L Korzeniowski, R.H. Mathews, P.T. Parrish, and T.C.L.G. Sollner, 'Planar millimeter wave antennas with application to monolithic receivers,' SPIE Proceedings Vol. 337, Millimeter Wave Technology (1982).

Chapter 2

High Resolution Imaging Antenna Arrays

The appropriate characteristics of an antenna array are largely determined by the intended application. In applications where the source is an extended object and only low spatial resolution is required, maximum sensitivity is attained with the use of multimode antennas and an optical system which images large object areas onto each antenna [1]. For an n-element multimode antenna, the received power per unit bandwidth is nkT, where T is the effective brightness temperature of the object (fig. 1a). Since the n-element antenna has only one pair of terminals, it yields an output signal that corresponds to the average effective temperature; no information is obtained about the intensity variations across the portion of the source imaged onto one antenna.

In many applications requiring imaging the entire system must deliver nearly diffraction limited resolution. For instance, Gordon et al [2] point out that for target recognition using near-millimeter imaging systems the maximum range is almost always limited by resolution. Here a sacrifice of resolution due to limitations in the focal plane detector array means loss of operating range. These systems should no longer map large object areas onto a single antenna; ideally they should map a single object point source onto one antenna in the array (fig. 1b).

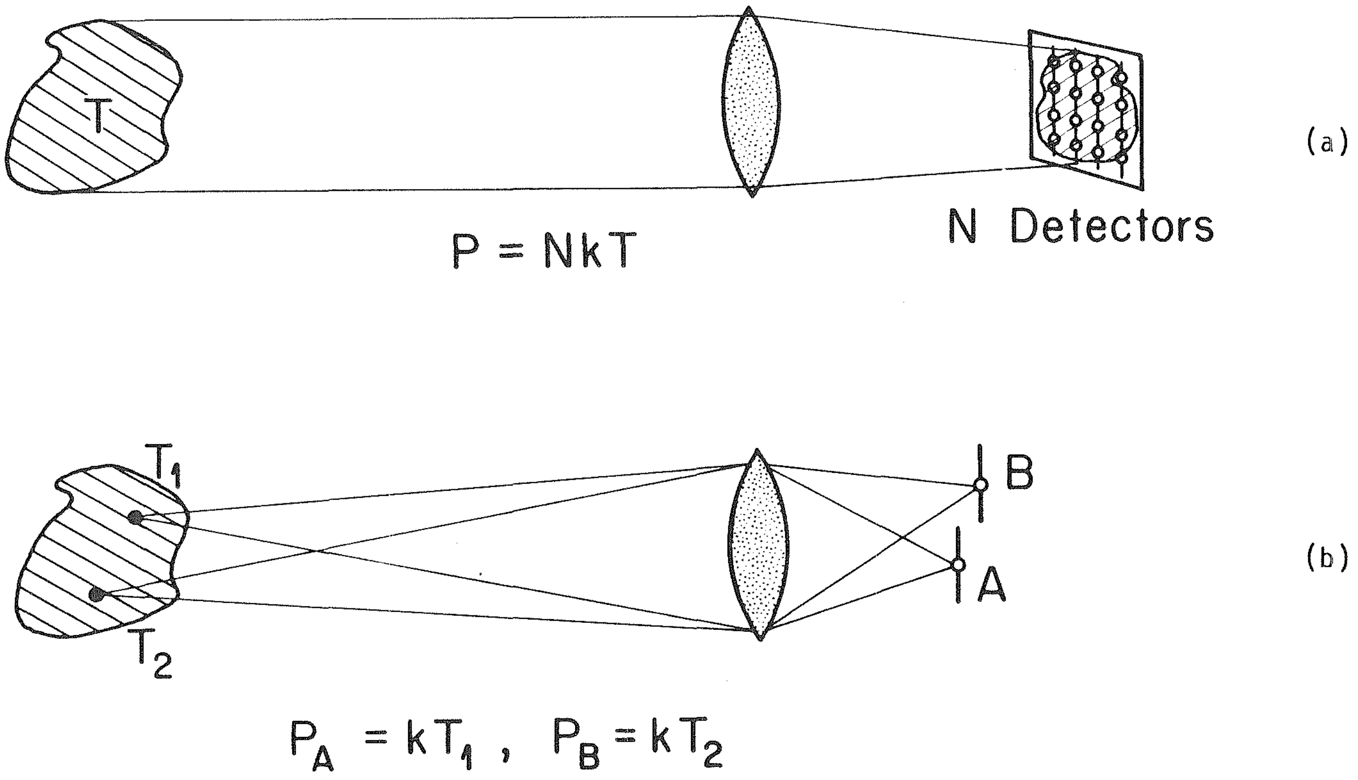

Figure 1: (a) A multimode antenna can be used to collect a large amount of power from an extended source, but does not produce an image. (b) Single mode antennas necessary for high resolution imaging.

Sampling for Diffraction-Limited Imaging

In order to determine the appropriate sampling interval for a high resolution imaging antenna array we apply some of the results of the Fourier analysis of optical systems. One important characteristic of such systems is their behavior as low pass filters; that is, no matter how high the spatial frequency components of an object are, because of diffraction, an image of the object contains only frequency components less than some system cut-off frequency f_o. This is simply a statement of the fact that all imaging systems have finite resolving power. Elementary sampling theory now assures us that we can exactly reconstruct this bandwidth-limited image if we satisfy the Nyquist criterion by sampling at twice f_o. In one dimension a reconstruction algorithm is given by the Whittaker-Shannon sampling theorem

$$g(x) = \sum_{n=-\infty}^{+\infty} g\left(\frac{n}{2f_o}\right) \operatorname{sinc}\left[2f_o\left(x - \frac{n}{2f_o}\right)\right] \qquad (1)$$

where $g(x)$ is the image (either the complex field, $\mathbf{E}$, or the intensity, $\mathbf{I}$), $g(n/2f_o)$ are the sampled image points separated by $1/(2f_o)$, f_o is the spatial cut-off frequency appropriate for $g(x)$, and $\operatorname{sinc}(x) = (\sin\pi x)/(\pi x)$ [3]. Note that there is a simple relation between the cut-off frequency for $\mathbf{E}(x)$ and $\mathbf{I}(x)$; if the optical system passed all spatial Fourier components of the field $\mathbf{E}(x)$ up to a cut-off f_o, then since the intensity $\mathbf{I}(x)$ is given by the square of $\mathbf{E}$, $\mathbf{I}(x)$

will contain frequency components up to $2f_o$. The Whittaker-Shannon sampling theorem then tells us that if we measure **E** at points separated by $1/(2f_o)$ we can completely reconstruct **E**(x), and from this obtain the image intensity by squaring. However, if we measure the intensity directly, in order to reconstruct I(x) we must sample at points separated by $1/(4f_o)$, since the spectrum of I extends to $2f_o$. With video detection, which yields only the intensity, we must sample the image twice as often as with heterodyne detection, which yields the complex field.

It remains to be seen what the value of the cut-off frequency for fields is. To determine this consider the generalized optical system in fig. 2. Here O is an object point and O′ the corresponding image point. The frequency response is described by the coherent transfer function, and for a diffraction limited system the cut-off frequency is in the image plane

$$f_o = (n_1 \sin\theta_1)/\lambda \qquad (2)$$

where n_1 is the index of refraction of the medium in which the image is formed, θ_1 is half the angle subtended by the exit pupil, and λ is the vacuum wavelength [4]. For objects far from the entrance pupil of the system (in terms of focal lengths) the image point approaches the focal point, and the f-number of the optics is then related to θ_1 by [5]

$$f^{\#} = 1/(2\sin\theta_1) \ . \qquad (3)$$

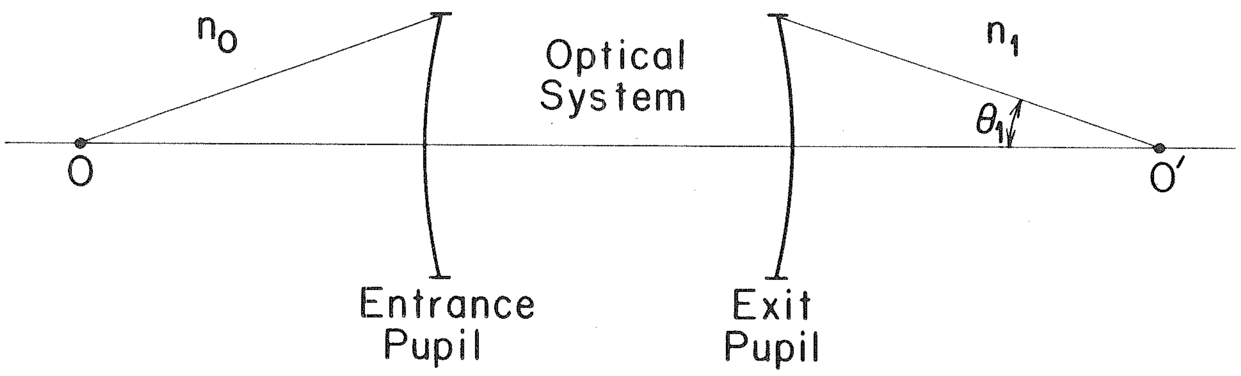

Figure 2: 'Black box' optical system showing the extreme ray path into the entrance pupil and out of the exit pupil.

We can now find the proper sampling interval T for an antenna array that allows exact reconstruction of a diffraction limited image:

$$T_E = \frac{1}{2f_0} = \frac{\lambda}{2n_1\sin\theta_1} = \frac{\lambda}{n_1} f^{\#} \qquad \text{(field detection)(4a)}$$

$$T_I = \frac{1}{4f_0} = \frac{\lambda}{4n_1\sin\theta_1} = \frac{\lambda}{2n_1} f^{\#} . \qquad \text{(intensity detection)(4b)}$$

In terms of the radius of the first dark ring of the Airy pattern, r_a, these are

$$T_E = r_a/1.22 \qquad \text{(field detection)} \qquad (5a)$$

$$T_I = r_a/2.44 \quad . \qquad \text{(intensity detection)(5b)}$$

For $\theta_1 = 30^\circ$ (i.e. f/1 optics) the maximum antenna spacing would be

$$T_E = \lambda/n_1 \qquad \text{(field detection)} \qquad (6a)$$

$$T_I = \lambda/(2n_1) \quad . \qquad \text{(intensity detection)(6b)}$$

Note that the highest possible resolution would be delivered by an imaging system with θ_1 equal to 90°. In this case the antenna elements should be spaced by

$$T_E = \lambda/(2n_1) \qquad \text{(field detection)} \qquad (7a)$$

$$T_I = \lambda/(4n_1) \quad . \qquad \text{(intensity detection)(7b)}$$

This case is representative of the fact that even for an infinitely large lens the image plane resolution is limited by the evanescent-wave phenomenon to the order of a dielectric wavelength [6].

One consequence of these sampling requirements in low f-number systems is the small size (in terms of wavelengths) of the elements in a planar array. This would preclude the use of such antennas as the long V or tapered slot line [7][8][9], since their physical extent is usually five to ten wavelengths.

We have found that it is possible to determine the appropriate antenna spacing for an array that must deliver diffraction limited performance, and that it depends on the type of detection used. We should also consider the effect of the type of illumination on the imaging system. That is, when the object appears coherent (such as in an active system where the illuminating beam is coherent, or in a passive system viewing a coherent source) the system performance will be different than when the object appears to be incoherent (for example, a passive system viewing an object in its own blackbody radiation) [10]. For coherent illumination the results thus far, specifically eq. 2 and eq. 4, clearly apply without modification. In terms of the required image plane sampling interval, then, the remaining question is the meaning of field (heterodyne) detection of an incoherent source. For a totally incoherent (time and space) extended object the time average of the image field, $\langle \mathbf{E}(x) \rangle$, is zero, but the time average of the magnitude squared gives the image intensity, I(x), which is not zero. In addition, because of the presence of the optical system, the degree of spatial coherence between points x_1 and x_2 in the image plane is

$$\mu(x_1, x_2) = \frac{1}{\sqrt{I(x_1)I(x_2)}} \langle E(x_1,t)E^*(x_2,t) \rangle \tag{8}$$

$$\cong \frac{2J_1(u)}{u} \quad , \quad u = \frac{2\pi n_1 \sin\Theta_1}{\bar{\lambda}} h' ,$$

where h' is the distance between x_1 and x_2, n_1 and Θ_1 are defined as before, and $\bar{\lambda}$ is the mean wavelength of the quasi-monochromatic source (an incoherent source cannot be purely monochromatic) [11]. Here μ equal to zero would indicate total incoherence between the two points, and equal to one total coherence. In general there is partial coherence between points in the image, even though the object was totally incoherent.

Since $\langle E(x,t) \rangle$ is zero, the meaningful quantity is the time averaged intensity distribution in the image plane,

$$I(x) = \langle I(x,t) \rangle = \langle |E(x,t)|^2 \rangle \quad . \tag{9}$$

Using the Whittaker-Shannon sampling theorem this is:

$$I(x) = \langle \sum_{-\infty}^{+\infty} I(\frac{n}{4f_0},t)\text{sinc}\left[4f_0(x - \frac{n}{4f_0})\right] \rangle$$

$$= \sum_{-\infty}^{+\infty} I(\frac{n}{4f_0})\text{sinc}\left[4f_0(x - \frac{n}{4f_0})\right] \qquad \text{(intensity detection)} \tag{10a}$$

or with field detection:

$$I(x) = \langle \left| \sum_{-\infty}^{+\infty} E(\frac{n}{2f_0},t)\text{sinc}\left[2f_0(x - \frac{n}{2f_0})\right] \right|^2 \rangle \quad . \tag{10b}$$

Note that in order to use field detection to reconstruct an image of an incoherent source the sampling theorem must be used to interpolate before squaring and time averaging is performed, since partial spatial coherence is present in the image plane, and so from eq. 8,

$$\langle |E(x_1,t) + E(x_2,t)|^2 \rangle \neq \langle |E(x_1,t)|^2 \rangle + \langle |E(x_2,t)|^2 \rangle . \quad (11)$$

For incoherent objects, then, the sampling interval must be that appropriate for intensity detection, $1/(4f_o)$, allowing time averaging of each point followed by reconstruction of the image, or if field detection is used while sampling at $1/(2f_o)$, the interpolation must be done on an instantaneous basis, followed by time averaging to obtain $I(x)$. With this warning, the appropriate sampling interval for an antenna array delivering diffraction limited performance is given by eq. 4, independent of the illumination.

These sampling restrictions are not an unfamiliar result in imaging systems. A similar constraint applies in scanned imaging systems that use a single detector. In these the scanning mirror converts the image into a serial data stream; there is now a correspondence between a particular image point and time. If the data are then sampled at discrete intervals (such as with an analog-to-digital converter) one effectively samples the image at discrete points. In order to maintain the spatial resolution the scanned distance between samples should be no more than one-half the half-power beamwidth of the system [12]. This may be the pattern of a receiving antenna or the Airy pattern of an optical system. Since the half-power beamwidth of an Airy pattern is quite close to its first null radius, this statement is actually equivalent to eq. 5b. Failure to satisfy the sampling requirements will result in loss of resolving power and aliasing in the image reconstruction, often in the form of Moiré patterns (spurious low frequency intensity variations in the reconstruction). In order to avoid aliasing errors, which cannot readily be removed by processing, it is better to increase the system f-number to match the actual sampling interval [13].

Having found the proper element spacing for an imaging antenna array, we can also infer some of the needed individual antenna element characteristics. First, in a system designed to yield diffraction limited resolution, the antennas in the array should be single mode. To see this, we calculate the power per unit bandwidth available in a single diffraction limited spot of an image. Consider the optical system in fig. 3, which forms an image of an extended body with brightness B. The Rayleigh-Jeans law gives

$$B = 2kT/\lambda^2 \tag{12}$$

for an effective temperature T. The total energy collected by the lens is

$$E = B\Omega_o \pi l^2/4 \tag{13}$$

where Ω_o is the solid angle subtended by the object and l is the diameter of the lens opening [14]. Since the solid angle

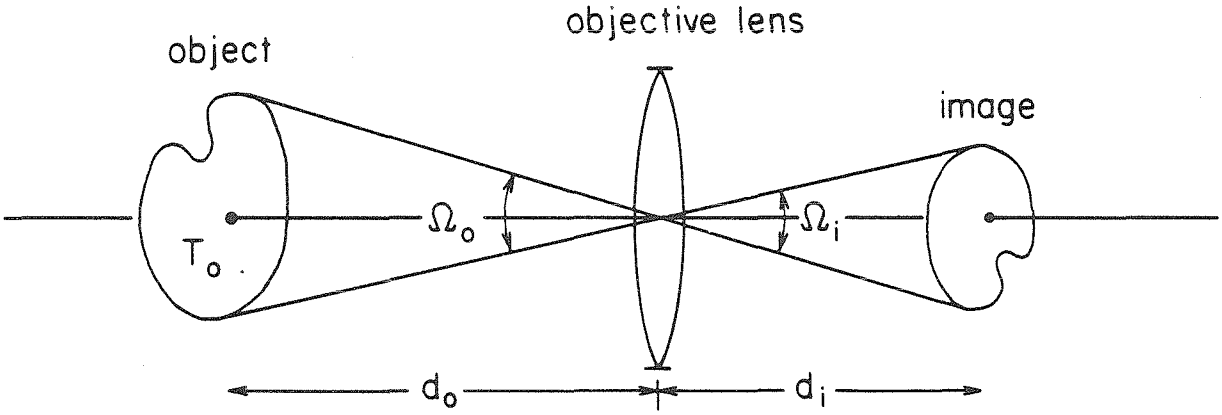

Figure 3: Image formed of a body whose effective brightness temperature is T_o.

subtended by the image is equal to that subtended by the object the energy density in the image plane is

$$\frac{E}{\Omega_0 d_i^{\,2}} = \frac{\pi l^2 kT}{2 d_i^{\,2} \lambda^2} \tag{14}$$

where d_i is the image distance (see fig. 3). The energy available in a single diffraction limited spot is just this energy density multiplied by the area of the spot. The spot size is given by the Airy pattern for the lens [15],

$$A(r) = \left[2 \, \frac{J_1(\frac{\pi l r}{\lambda d_i})}{\frac{\pi l r}{\lambda d_i}} \right] \; . \tag{15}$$

The effective area of the spot is then

$$2\pi \int_0^\infty A(r) r dr = \frac{4 d_i^2 \lambda^2}{\pi l^2} \; . \tag{16}$$

Using eq. 14 and 16 the energy available to a detector viewing a single diffraction limited spot is 2kT. For a receiver responding to only one polarization this is reduced by a factor of one-half: kT for each polarization. A single-mode antenna can receive precisely this amount of power per unit bandwidth [16]. We can now see there is no advantage in using a multimode antenna for high resolution imaging. In fact, since an n-detector multimode antenna has a noise equivalent power $(n)^{1/2}$ larger than a single-detector antenna [1], a single mode antenna is actually more sensitive in these systems.

Another fairly fundamental requirement for an array element is the match between the antenna beamwidth and the optical system f-number. All of the preceding diffraction limits have been stated in terms of Θ_1, the half-angle subtended by the exit pupil (see fig. 2), and have assumed uniform illumination of the exit pupil. This implies that the antenna pattern should have 3dB points at approximately Θ_1. If the pattern is appreciably narrower than this, the system resolution will be limited by the antenna beamwidth, not the size of the exit pupil. In this case decreasing the f-number of the optics will neither improve overall resolution or collection efficiency. When the element beamwidth is considerably larger than the optical system Θ_1, the spill-over will decrease the system efficiency; an improvement in both resolution and efficiency would occur if the f-number of the optics is decreased (remembering that the antenna spacing must be close enough together to yield proper sampling).

For efficient collection of power in the image plane we would also like the antenna array to cover the entire image. Since the element spacing is T, if each antenna has an effective area A_{eff} of approximately $(T)^2$, the array would collect almost all the power in the image. Now the gain, g, of a single mode antenna is [17]

$$g = 4\pi(n_1)^2 A_{eff}/\lambda^2 \quad . \tag{17}$$

Setting A_{eff} equal to $(T)^2$ and using T from eq. 4 we find

$$g_E = \pi/\sin^2\Theta_1 \qquad \text{(field detection)} \qquad (18a)$$

$$g_I = \pi/4\sin^2\Theta_1 \quad . \qquad \text{(intensity detection)} \qquad (18b)$$

An f/1 optical system giving efficient, diffraction limited performance would then require an antenna array with the following characteristics:

element spacing:

$$T_E = \lambda/n_1 \qquad \text{(field detection)}$$

$$T_I = \lambda/2n_1 \qquad \text{(intensity detection)}$$

element beamwidth (3dB to 3dB): 60°

element gain:

$$g = 12 \qquad \text{(field detection)}$$

$$g = 3 \quad . \qquad \text{(intensity detection)}$$

Modified Bow-Tie Antennas

The actual choice of an antenna for a far-infrared array is strongly influenced by the techniques used to fabricate it. Since the individual elements and their associated detectors are quite small the use of integrated-circuit processing techniques are usually required. This in turn means the antennas must be planar structures, supported on a dielectric substrate. The presence of the dielectric has been found to play a dominant role in the behavior of the antenna. One very important effect is the tendency of antennas on dielectrics to radiate much more power into the dielectric than into the air, roughly in the ratio $\varepsilon_r^{3/2}$:1 [18][19][20][21]. By reciprocity this implies such antennas will be more sensitive to radiation from the dielectric side of the antenna.

Another effect that must be considered in these antennas is surface wave losses. When the front and back faces of the dielectric substrate are parallel the substrate acts like a waveguide, and may cause significant loss due to coupling between the antenna and guide modes [21]. This loss is illustrated by fig. 4, which shows that the power radiated by the antenna at angles greater than the critical angle is trapped by total internal reflection as a surface wave. By making the substrate very thin most of the guide modes can be cut-off, and surface wave losses reduced. The efficiency of dipoles, microstrip dipoles, and slots on thin substrates has been discussed by Alexopoulos et al [22].

It is also possible to avoid surface wave losses by curving the back side of the substrate to prevent total internal reflection. This is most easily done by placing on the back side of the substrate a lens with the same dielectric constant [18][23]. As shown in fig. 5, rays leaving the antenna are now incident on the back surface at near normal incidence. This approach also allows an image to be focused through the substrate lens, taking advantage of

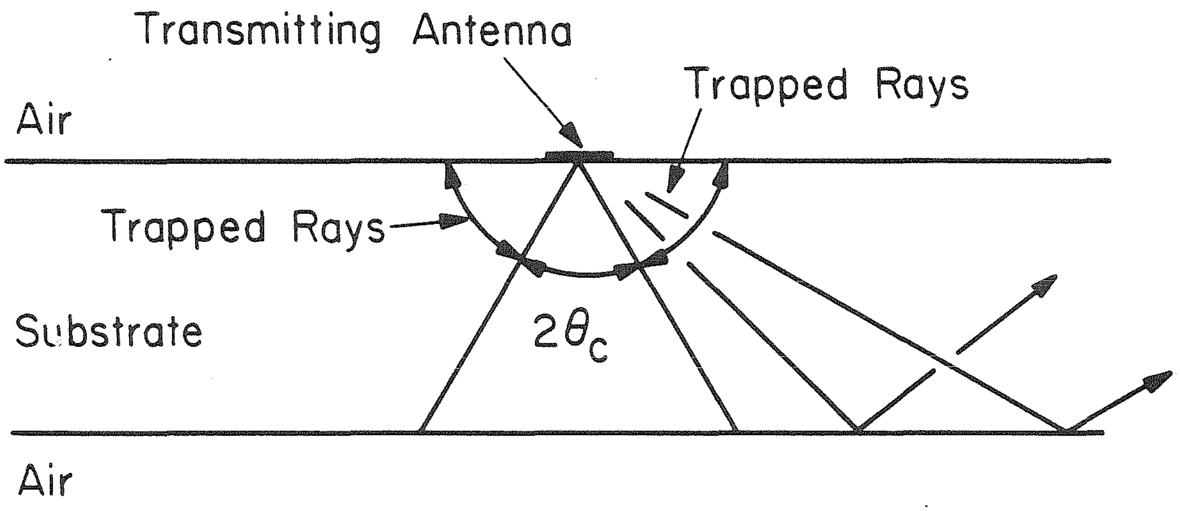

Figure 4: Transmitting antenna on a dielectric substrate, showing the rays that are trapped as surface waves.

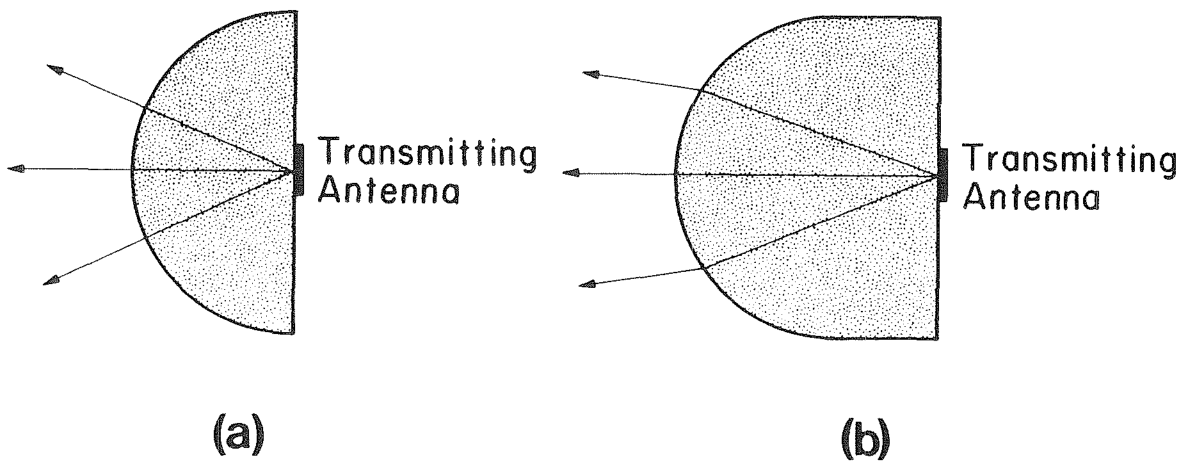

Figure 5: Substrate lenses to prevent surface wave losses; (a) hemisphere (b) hyperhemisphere.

the antenna's strong coupling to the dielectric.

The specific antenna used in the arrays in this study was a modified bow-tie antenna [20]. Figure 6 shows two elements of an array, along with typical dimensions. Such antennas have a variety of attractive features. In a bow-tie on a dielectric there is continuous radiation as a wave propagates up the bow arm. Simulations of the array at 3GHz on $\varepsilon_r = 4$ substrates indicate very little current propagates as far as two dielectric wavelengths up the bow. This makes it convenient to extend the bow arms to form low frequency leads, with automatic isolation between low and high frequencies.

Microwave simulations have also shown the bow-tie is non-resonant, with an impedance of about 150Ω resistive for a 60° bow angle on $\varepsilon_r = 4$ substrates [20]. Figure 7 shows a typical impedance measurement set up for a bow-tie. The measurements are made by first cutting adhesive-backed copper foil to form one bow arm. This is applied to a dielectric substrate with the tip of the bow at the bottom edge of the substrate. The block is placed on a ground plane through which the pin of a SMA connector protrudes. The pin is soldered to the tip of the bow, serving as the microwave feed. The assembly is attached to a HP 8743B Reflection-Transmission Test Unit, and the impedance measured with a HP 8410A Network Analyzer. The impedance was found to be a very weak function of frequency for an octave frequency sweep, 2-4GHz. The impedance has also been measured at 94GHz

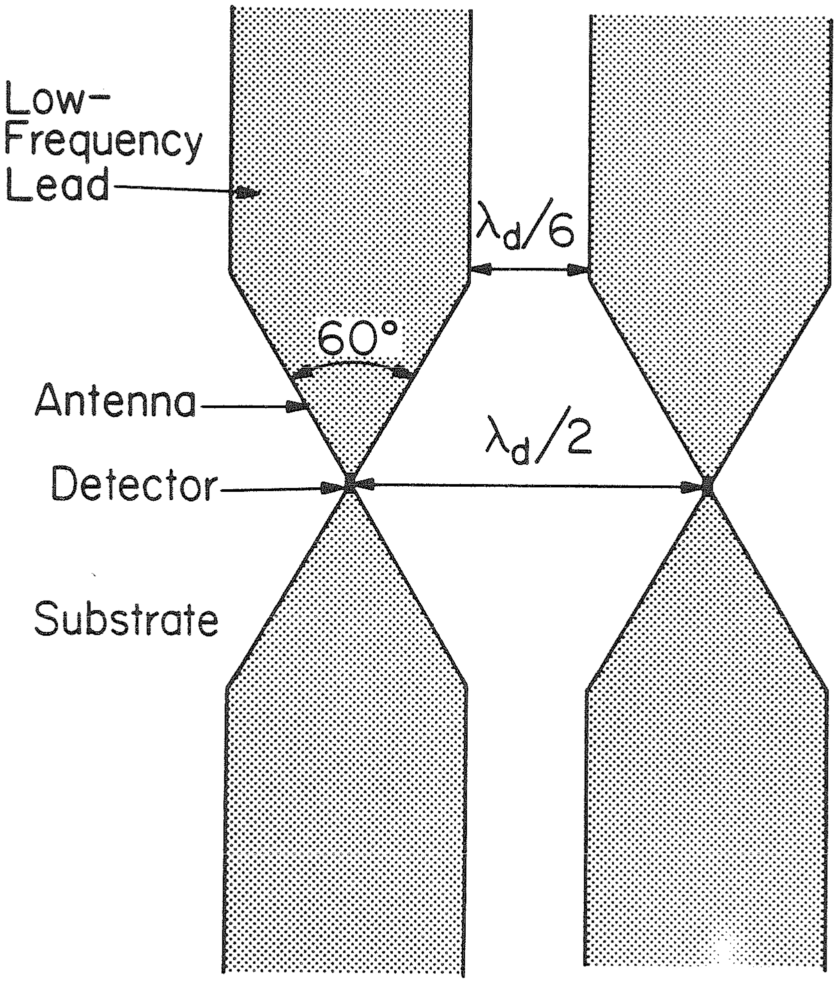

Figure 6: Bow tie antenna design for $\varepsilon_r = 4$ substrates; λ_d is the wavelength in the dielectric.

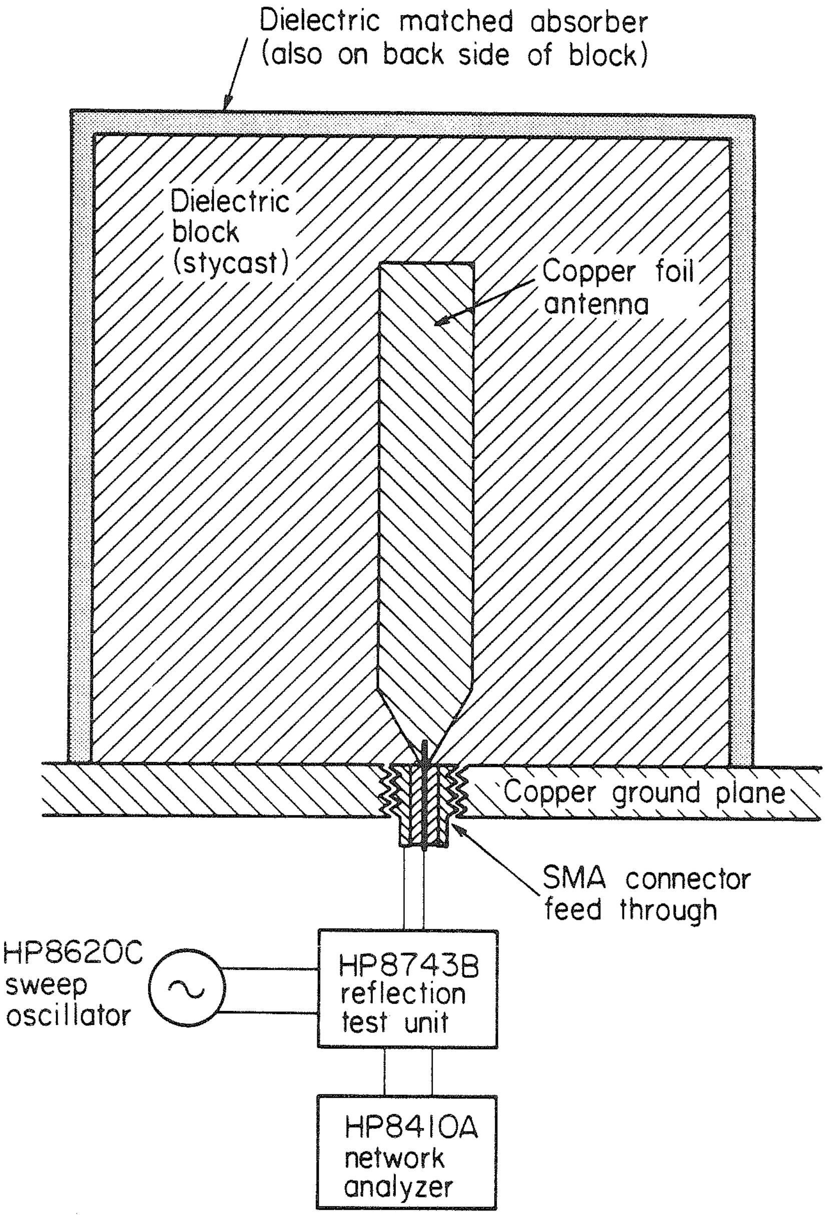

Figure 7: Set up used to measure impedances of bow tie antennas in a microwave simulation.

(see chapter 3), and was consistent with the 3GHz model.

Hyperhemispherical Substrate Lens

As mentioned earlier, the use of a lens on the back side of the antenna substrate both prevents surface wave losses and allows the radiation to be focused onto the antennas from their high gain side. One particularly useful configuration for this lens is the hyperhemisphere. This particular lens is aplanatic; that is, if all the rays in an optical system are being focused to a point, the hyperhemispherical lens can be added to the system, and all the rays will still be brought to a single focused point [24]. This type of lens has been used in oil-immersion microscope objectives, and also as an immersion lens to increase the sensitivity of infrared detectors [25].

To see how a hyperhemispherical lens works, consider fig. 8. Here an optical system is bringing a wave to a focus at the point P_o. A single spherical lens of radius R and index of refraction n_1 is then inserted into the system, with its center O located a distance n_1R/n_o from the point P_o. We need to find where the rays converging towards P_o now go. For the ray indicated, the angle of incidence at the lens is ϕ_o, and the angle of refraction is ϕ_1, so by Snell's law

$$n_o \sin\phi_o = n_1 \sin\phi_1 \quad . \qquad (19)$$

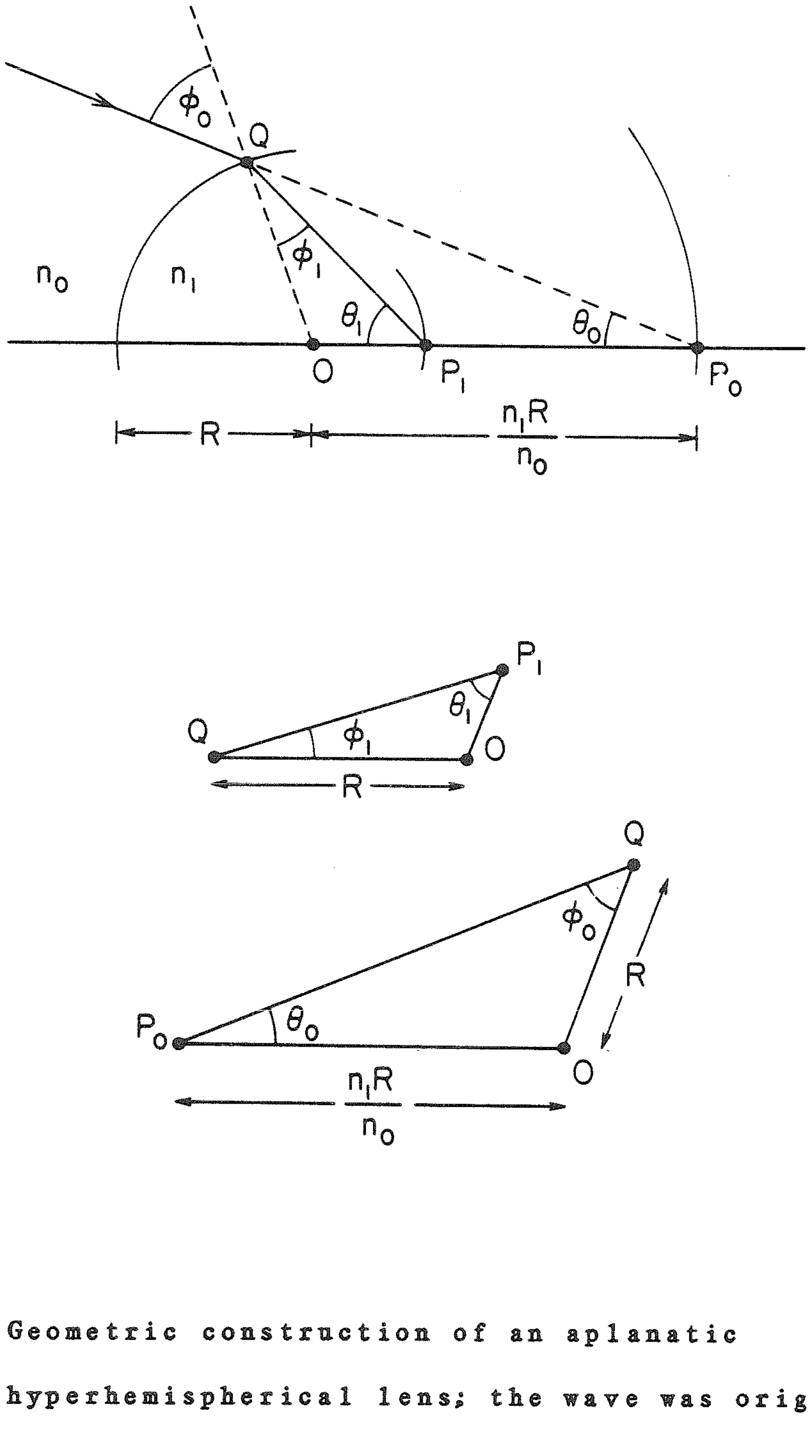

Figure 8: Geometric construction of an aplanatic hyperhemispherical lens; the wave was originally converging towards the point P_o, and after refraction converges toward P_1.

Now the law of sines gives

$$\frac{\sin\phi_0}{OP_0} = \frac{\sin\Theta_0}{OQ} \qquad (20)$$

but we chose $OP_0 = n_1R/n_0$, and OQ is just the lens radius R. Equation 20 then becomes

$$n_0\sin\phi_0 = n_1\sin\Theta_0 \quad . \qquad (21)$$

Combining eqs. 19 and 21 we find

$$\phi_1 = \Theta_0 \qquad (22)$$

and this requires

$$\phi_0 = \Theta_1 \quad . \qquad (23)$$

The triangles QP_1O and P_0QO are therefore similar, which implies

$$OP_1/OQ = OQ/OP_0 \quad . \qquad (24)$$

Substituting the values for OQ and OP_0 we finally find

$$OP_1 = n_0R/n_1 \quad . \qquad (25)$$

Since the argument used is true for any angle ϕ_0 this implies all rays that are converging towards the point P_0 will, after refraction by the lens, continue to converge towards the single point P_1. This lens is therefore an aplanatic surface for the two points. The lens is actually aplanatic for the entire surface located n_1R/n_0 from the center of the lens, bringing the rays to a focus on the surface n_0R/n_1 from the center.

Figures 9 and 10 show how the hyperhemispherical substrate lens is used in an optical system. The lens is made so that, when combined with the antenna substrate, the antennas lie in a plane R/n_1 from the center of the lens. In fig. 9 rays parallel to the optical axis are shown being focused by the substrate lens-objective lens system. Recall that all our earlier sampling criteria were written in terms of half the angle subtended by the exit pupil of the optical system; fig. 9 shows that this angle is given by θ_1. We can also write the sampling criteria for objects many focal lengths from the objective lens in terms of the system f-number, which is from eq. 3

$$f^{\#}_s = 1/2\sin\theta_1 \quad . \tag{26}$$

The objective lens f-number is

$$f^{\#}_o = 1/2\sin\theta_o \quad . \tag{27}$$

Using eqs. 19, 22, and 23 we find that

$$\sin\theta_1/\sin\theta_o = n_1 \tag{28}$$

so for this optical system

$$f^{\#}_s = f^{\#}_o/n_1 \quad . \tag{29}$$

For our system, then, the two lens combination has an f-number that is a factor of n_1, the substrate index of refraction, smaller than the objective lens alone.

Another property of the hyperhemisphere is the reduction of image size, as illustrated by fig. 10. The relation between the size of the virtual image h_v and the real image h_i is most easily found by considering the ray which passes through the center of the substrate lens. This ray defines two similar triangles; the heights are h_i and h_v, with bases R/n_1 and n_1R, respectively. Since the triangles are similar, the height h_i must be $h_v/(n_1)^2$. Thus the image formed by a substrate lens-objective lens combination is a factor of

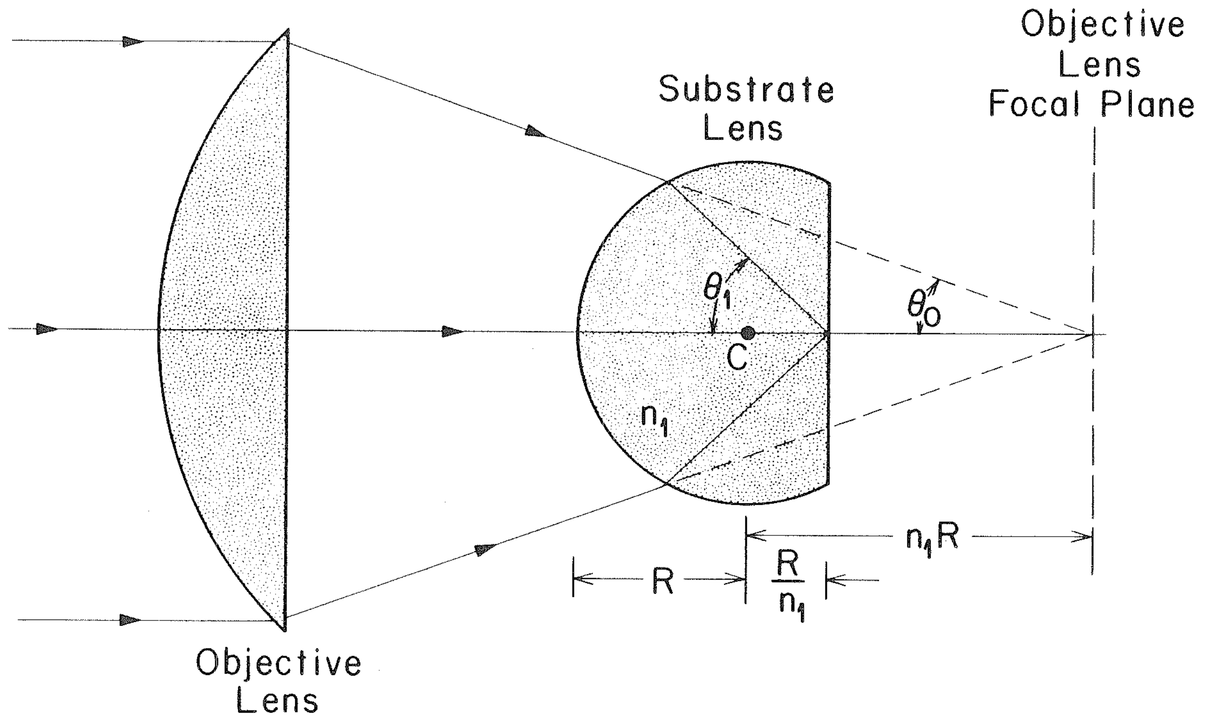

Figure 9: Substrate lens-objective lens optical system showing an incident plane wave being focused.

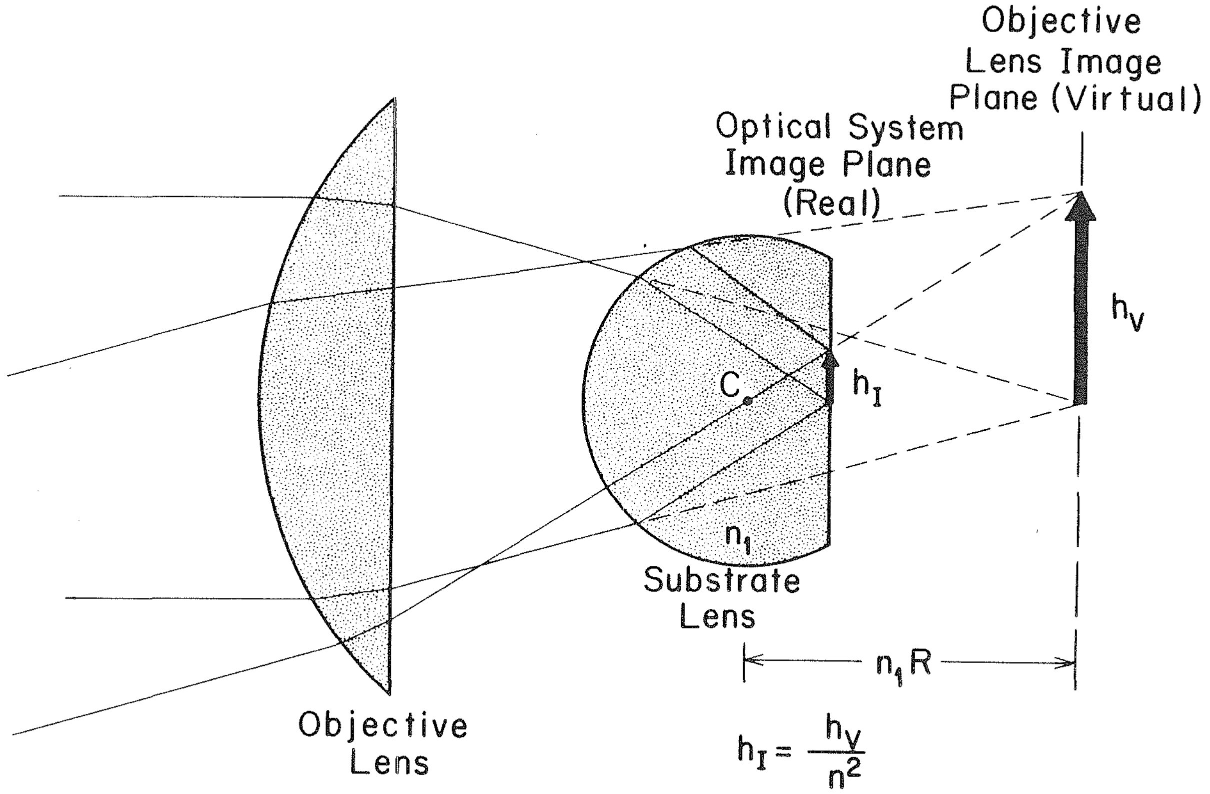

Figure 10: Relation between image size for an objective lens alone (h_v) and the substrate lens-objective lens combination (h_i).

$(n_1)^2$ smaller than the image formed by the objective lens alone.

1.22mm Antenna Array

Several different arrays have been made that utilize the substrate lens coupling scheme and modified bow-tie antenna. The first of these was designed to operate at a wavelength of 1.22mm (a laser line of $C^{13}H_3F$). For wavelengths longer than 0.5mm the absorption loss in high purity fused silica is acceptable (2dB/cm at 0.5mm); in fact, at 1mm the loss is fairly small, about 0.5dB/cm [26]. Because of this, the 1.22mm array was constructed on fused quartz, with a dielectric constant of 3.83 [27].

Extensive microwave modeling of bow-tie arrays on $\varepsilon_r = 4$ substrates has been performed [20]; these results were used as a guide in designing the 1.22mm array. Antenna pattern measurements indicated a beamwidth of about 60° ($\Theta_1 = 30^\circ$), so from eq. 3 the optical system f-number should be about f/1. Using the index of refraction for quartz (1.96) and intensity detection, the proper sampling interval (eq. 4b) is then 312μm; the actual array has bow-ties on 310μm centers. Figure 6 shows the design used, and fig. 11 shows a photomicrograph of an array.

The array is fabricated using conventional contact photolithography and lift-off [chapter 4]. The substrate material is either Heraeus-Amersil T22 Suprasil-W1 or T12 Optosil-1, 1/16in thick. The antennas are evaporated silver,

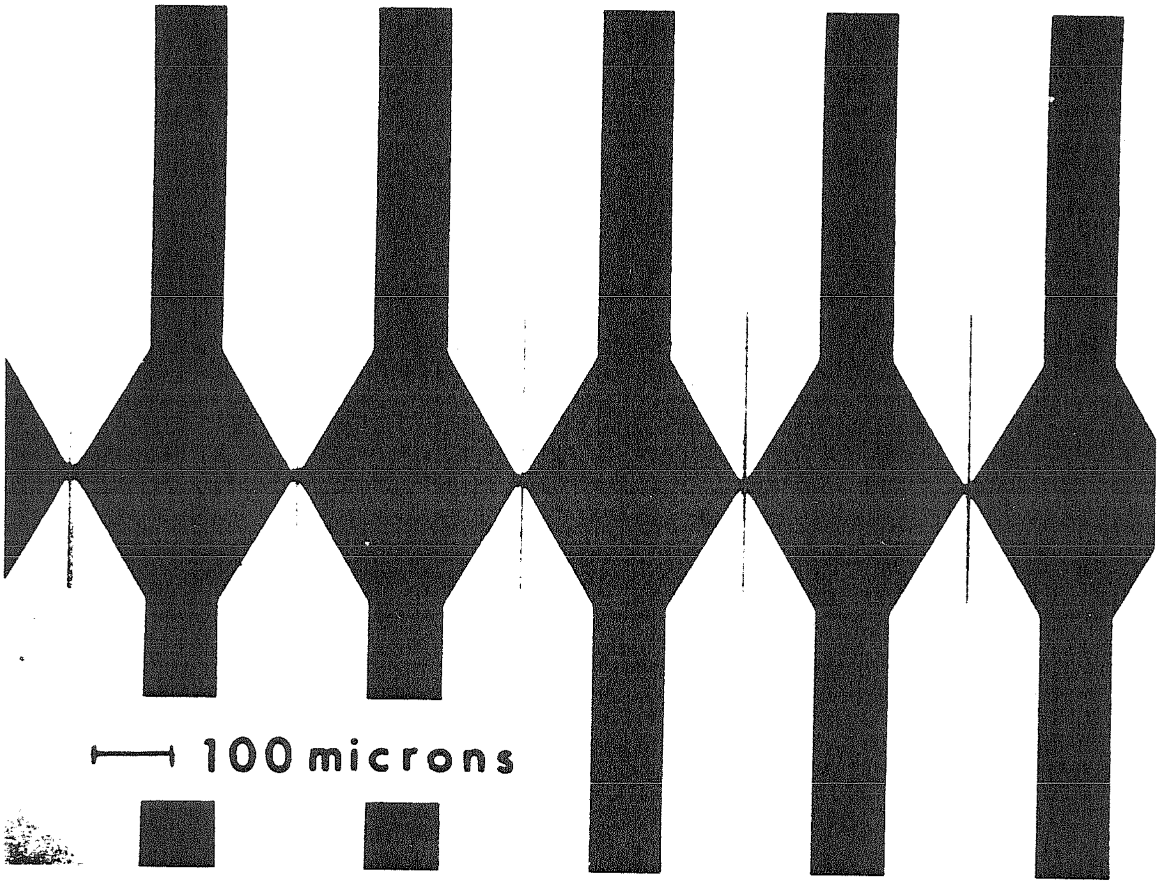

Figure 11: Photomicrograph of a bow tie array designed for $\varepsilon_r = 4$ substrates, f/1 optics, and $\lambda = 1.22$mm.

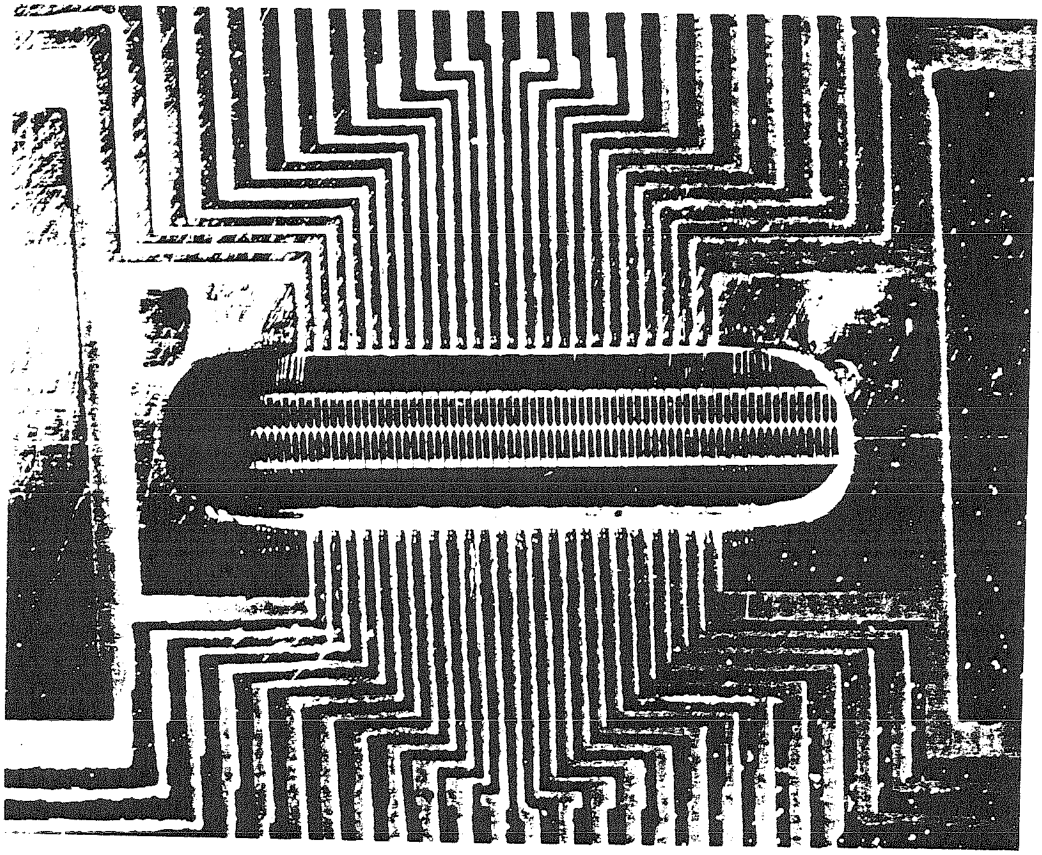

Figure 12: 1.22mm bow tie array mounted in a chip carrier; the sensing line is 15mm long.

75-100nm thick, with bismuth microbolometer or bismuth-antimony microthermocouple detectors [chapter 3]. The 60° bow angle gives an antenna impedance of 150Ω which is nearly matched by a typical bolometer resistance of 100-200Ω. The antenna array chip is mounted on a high density chip carrier and wire bonds are used to complete the low frequency connections (fig. 12). Typically between sixteen and thirty-two antennas are electrically connected, giving a sensing line in the image plane of 5mm to 10mm.

The optical system used is shown in fig. 13. The objective lens was made of a methylpentene polymer, poly 4-methyl pentene-1, usually referred to as TPX, a trade name for the material made by Imperial Chemical Industries. At 10 wavenumbers (i.e. 1mm wavelength) the absorption coefficient is approximately 0.08/cm (0.34dB/cm) [28]. The lens is a hyperbolic aspheric, corrected for spherical aberration, with a focal length of 70mm and diameter of 50mm (f/1.4). By equation 29 this gives a system f-number of f/0.7. The substrate lens was made from Dynasil UV 1000 fused silica and has a radius of 6.62mm; the total thickness of the substrate lens-antenna chip is 10mm, in accordance with the design rules for the aplanatic hyperhemisphere (eq. 25). The substrate lens-chip is mounted on an x-y-z translation stack, allowing alignment and focusing of the system. The source for these experiments was a CO_2-pumped methyl-fluoride gas laser. The CO_2 pump laser was grating tuned to the 9P32 line, with an output power of 30-50W. The methyl-fluoride

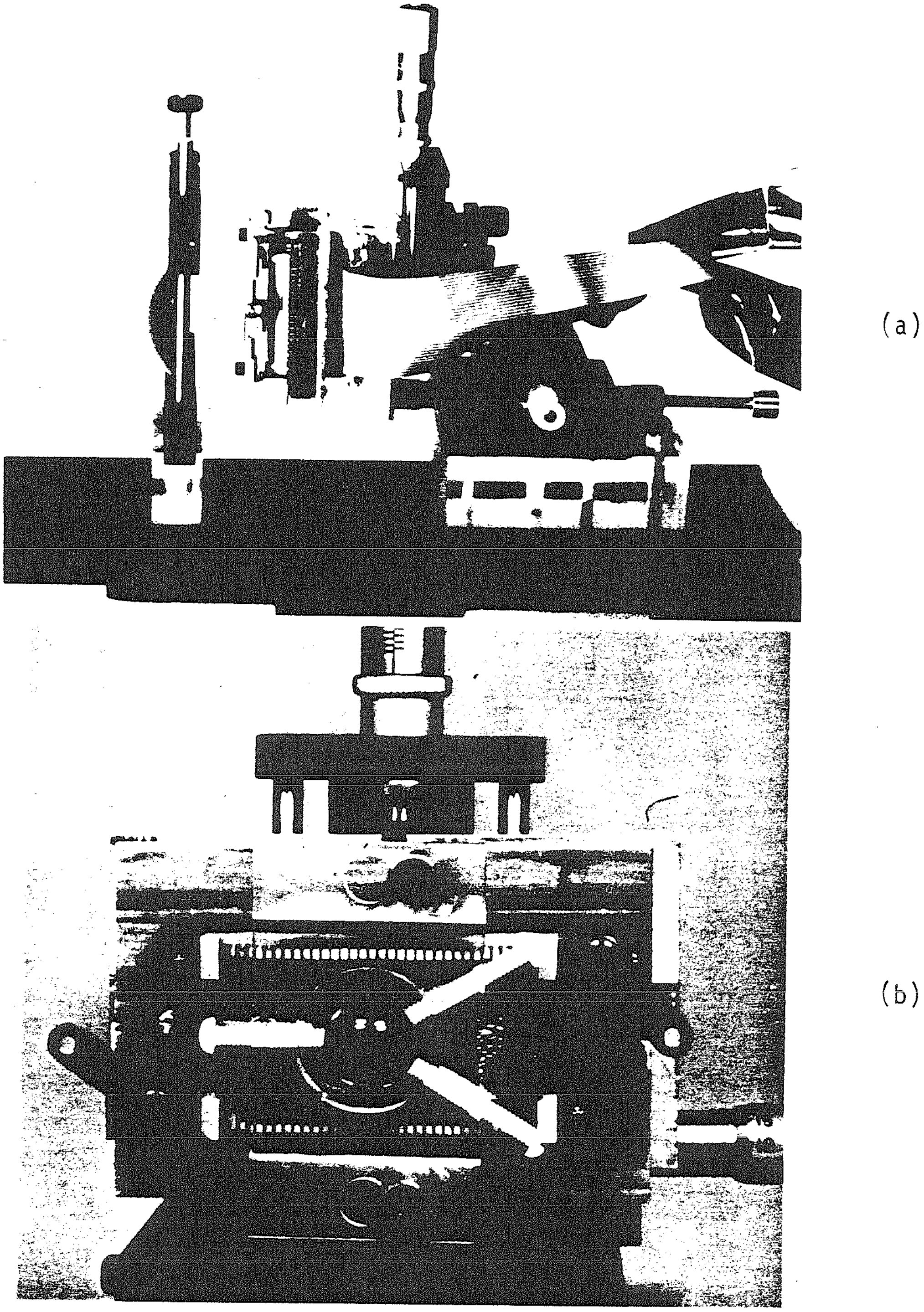

Figure 13: (a) Complete imaging system used at 1.22mm; the TPX objective lens is on the left. (b) Close-up of the substrate lens and chip carrier.

lased at 1.22mm, providing 1-3mW of output power.

A variety of tests have been used to examine the system performance. As a routine part of the alignment procedure the system spot response is measured. This is most easily done by first translating the substrate lens and array relative to the objective lens until a maximum signal is obtained from a single antenna. The entire optical system is then rotated about the objective lens while the signal from the antenna is monitored (fig. 14). Ideally the pattern obtained would be an Airy spot of angular size appropriate to the entrance pupil [29]:

$$I(\Theta) \propto \left[\frac{2J_1\left(\frac{kl\sin\Theta}{2}\right)}{\frac{kl\sin\Theta}{2}} \right]^2 \qquad (30)$$

where l is the diameter of the objective lens, Θ is the angle between the optical axis and the incoming plane-wave, and $k = 2\pi/\lambda$. Figure 15 shows a typical measured spot response in both the E- and H-plane of the antenna (E-plane corresponds to a rotation axis parallel to the imaging line, and H-plane perpendicular to it). Also shown is the Airy pattern for the 50mm diameter objective lens. Since the sidelobe levels are quite sensitive to alignment, an iterative procedure that decreases the sidelobes while maintaining the peak signal is a convenient way to properly align the two lenses in the optical system.

The angular field of view of this system has also been measured. Using the same rotation technique (fig. 14) used

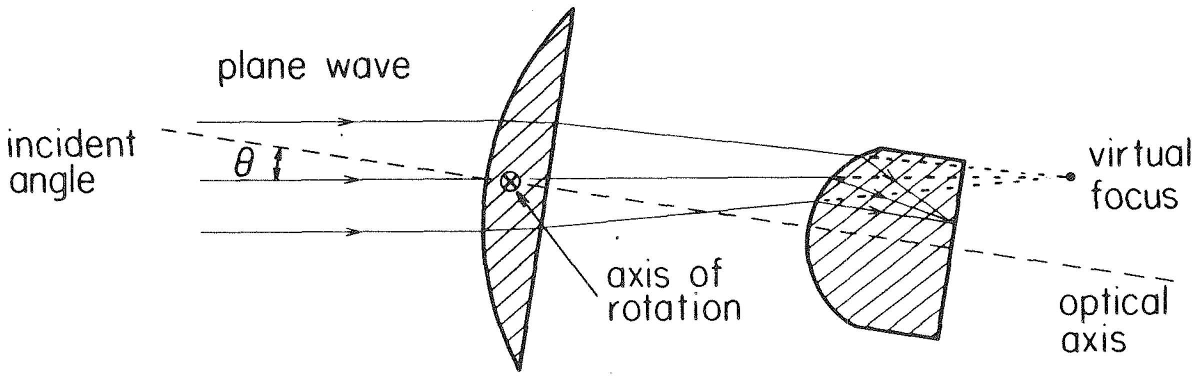

Figure 14: Rotation used to measure system spot responses.

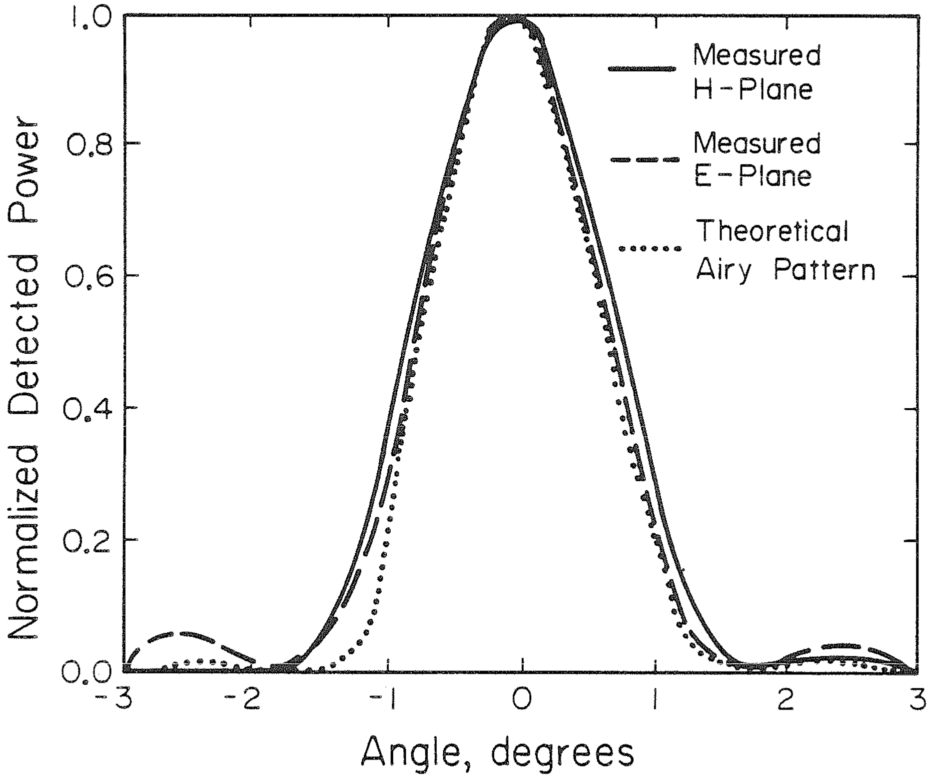

Figure 15: Spot response for the 1.22mm system. The Airy pattern is for a 50mm diameter entrance pupil.

for the spot response it is possible to shift the focused spot from one antenna to the next. Figure 16 shows the angular separation between the antennas. The relative strength of the signal from each antenna at its peak angle is also shown (this curve is not normalized for variations in detector responsivity, but this normally does not exceed 10%). The field of view is roughly eight degrees (and eight antennas). Because of the finite size of the substrate lens, rays that enter the objective lens at angles greater than 5° to the optical axis actually miss the substrate lens. The observed field of view is thus limited by the relatively small substrate lens used.

Another test to determine the resolving power of the array has also been performed. The experiment is essentially an attempt to resolve two spots separated by slightly more than the Rayleigh distance; in this case two 9.5mm holes 28.6mm apart drilled in a copper plate and illuminated from behind with the 1.22mm laser. The Rayleigh criterion for resolution of two incoherent point sources is

$$\delta\Theta = (1.22)\lambda/l \tag{31}$$

where $\delta\Theta$ is the minimum angular separation of the two point sources, and l and λ are defined as before [30]; for this system $\delta\Theta = 1.7^{\circ}$. In the experiment the 'pinholes' were 81cm from the objective lens, which gives an angular separation of 2°, about 20% larger than the Rayleigh criterion. One key feature, however, is the fact that the two holes are

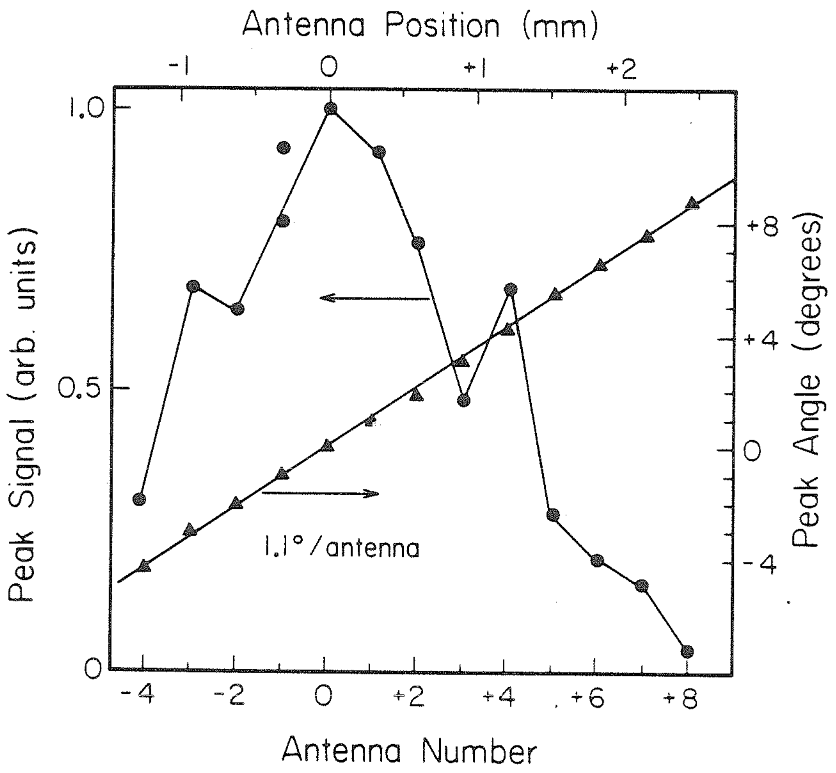

Figure 16: Angular field of view of the 1.22mm system.

coherently illuminated. The image formed will depend strongly on the relative phase difference between the two spots. It was possible in the test to vary this phase difference by placing a stack of fused quartz cover slips over one hole. For a stack thickness t the phase difference between the two holes is

$$\delta = 2\pi t(n - 1)/\lambda \qquad (32)$$

where n is the index of the quartz. Three different cases were tested: in phase (no cover slips); phase quadrature ($\delta = \pi/2$, t = 0.318mm); and phase opposition ($\delta = \pi$, t = 0.635mm). Figure 17 shows the results of these measurements. Note that when the points are in phase quadrature the expected image will be identical to that produced by two incoherent spots [31], and since they are separated by more than the Rayleigh distance, should be clearly resolved. The sampled image produced by the antenna array, after reconstruction by sinc interpolation (eq. 1), yields an image in which the two spots are easily resolved. It is clear the array is capable of delivering nearly diffraction limited performance.

The approximate coupling efficiency of the optical system-antenna combination has also been determined. It is possible to independently measure the intrinsic responsivity of a bismuth microbolometer [chapter 3]. For a far-infrared measurement the system was aligned and focused on the laser to yield the maximum signal from a single antenna, and the

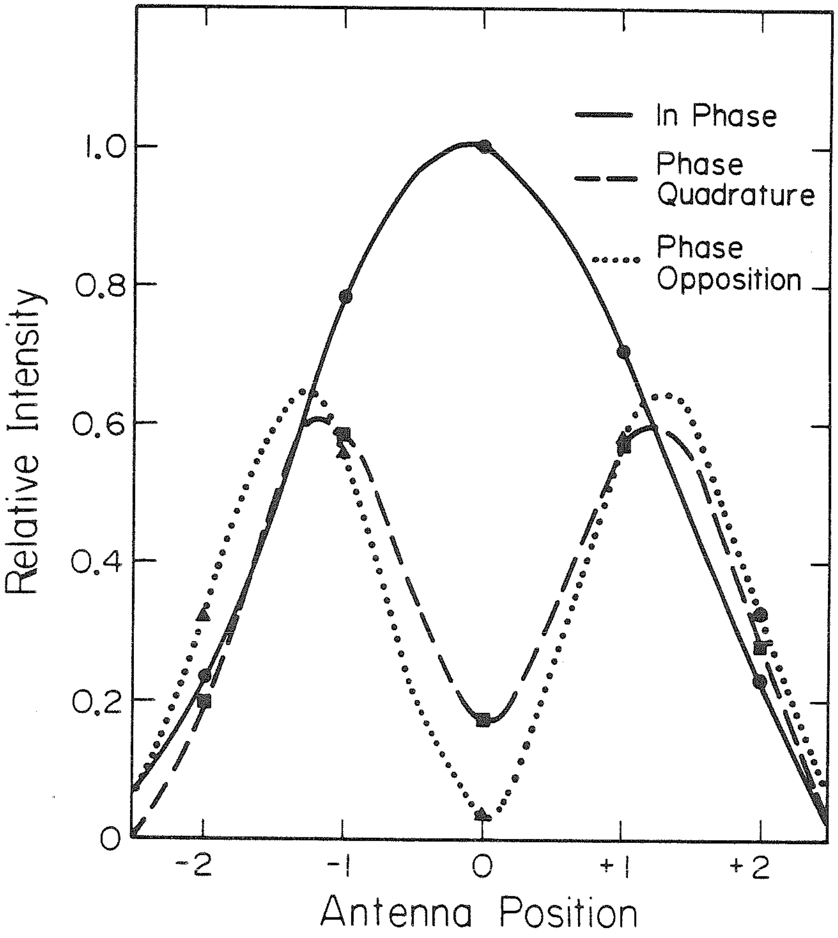

Figure 17: Image of two coherently illuminated pinholes. The sampled data points are indicated, and the lines are sinc interpolations between the points.

magnitude of the signal recorded. By dividing this voltage by the detector responsivity we have a measure of the power coupled into it. The total power from the laser was then measured with a Scientech 3620 power meter. We found that about 25% of this power is coupled into a single antenna, with an additional 10% into each of its neighbors. Since the bow-tie is quite broadband, this array can also be used at shorter wavelengths. An efficiency measurement at 496µm (using an off-axis parabolic reflector as the objective lens) gave about 10% coupling into the center antenna.

119µm Antenna Array

It is not practical to use fused quartz as a substrate material for wavelengths much shorter than 500µm. The absorption loss at 100 wavenumbers (i.e. 100µm wavelength) is quite large, with an absorption coefficient of about 16/cm (69dB/cm) [32]. From the point of view of absorption loss, silicon becomes an attractive material, with a loss of about 2dB/cm [32]. Silicon does, however, have a much higher index of refraction, 3.41, and this has a considerable effect on the antenna array [21]. Microwave modeling was once again used on $\varepsilon_r = 12$ substrates to determine some of the characteristics of the array design in fig. 18. The antenna patterns were somewhat narrower than those on $\varepsilon_r = 4$ substrates, with an E-plane 3dB beamwidth of about 40°, and H-plane beamwidth of 50° [33]. The impedance for a 60° bow angle is now 80Ω [20].

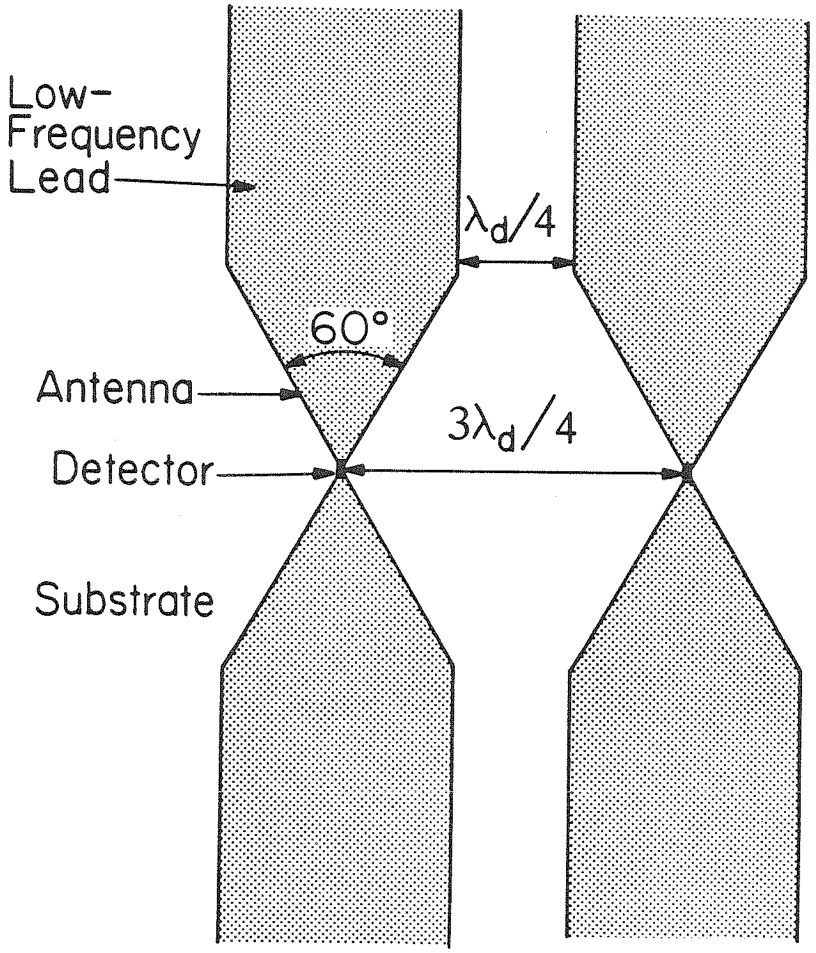

Figure 18: Bow tie antenna array design for $\varepsilon_r = 12$ substrates, f/1.4 optics, and $\lambda = 119\mu m$.

Figure 19 shows the array fabricated for use in an imaging system operating at 119μm (a very strong laser line of CH_3OH). The sampling interval in this array is 25μm; from eq. 4b this is matched to a system f-number of f/1.4 for a silicon substrate with $n = 3.41$. The antennas and detectors are fabricated with the same techniques used for the 1.22mm array. There are thirty antennas in the array, which is wire bonded into a commercial chip carrier and mounted in a dual-in-line package (fig. 20).

The optical system used is quite similar to that used at 1.22mm, except the substrate lens is now made of silicon, with a radius of 3.88mm. The total thickness of the substrate lens-antenna chip is 5mm, again in accordance with hyperhemispherical design rules (eq. 25). The objective lens is still TPX, with a focal length of 65mm and diameter 50mm. The entrance pupil in this system, however, is not limited by the diameter of the objective lens. The substrate lens is actually not a complete hyperhemisphere, but had a maximum diameter of 7.6mm, which limited the value of Θ_1 in fig. 9 to 73° (giving a system f-number of f/0.5). From eqs. 26 and 29 this gives an effective objective lens f-number of f/1.8, or an effective entrance pupil of 36mm.

The spot response for the 119μm system was measured in exactly the same way as it was for the 1.22mm array, and typical results are shown in fig. 21. Note the patterns are considerably narrower than the 1.22mm spot since the wavelength is now much shorter. For comparison, two

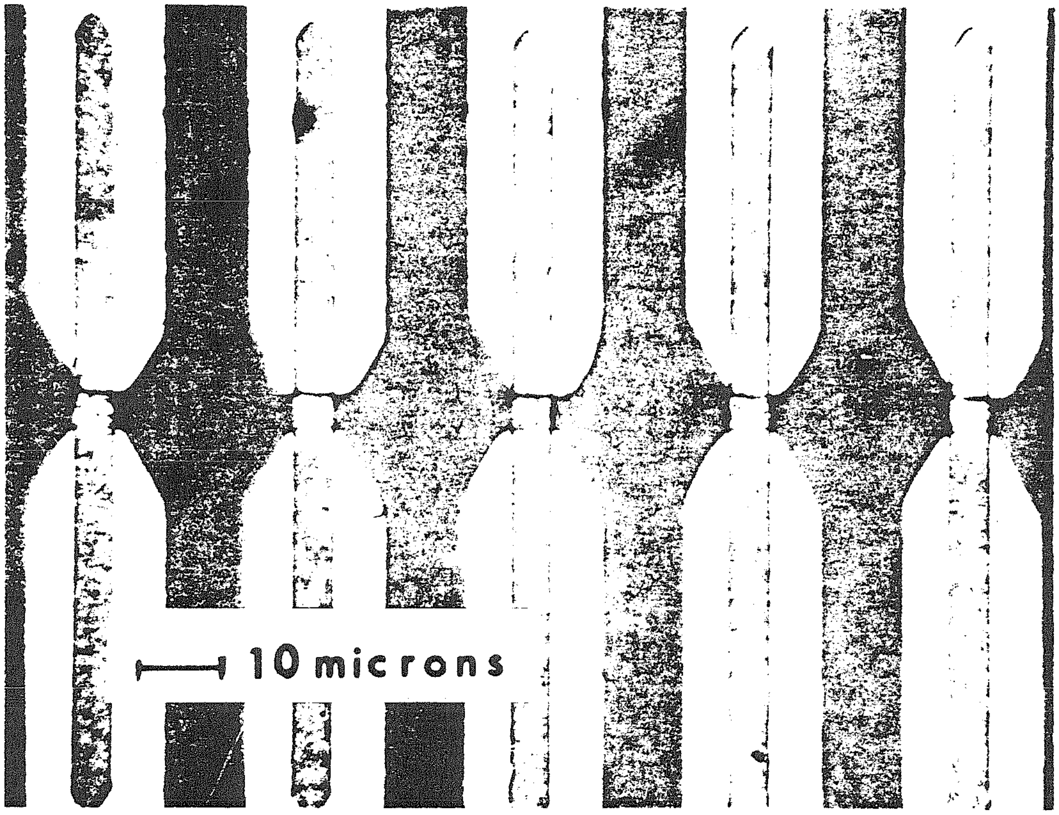

Figure 19: Photomicrograph of the 119μm array. The narrow dark strips are bismuth, and the bow ties silver.

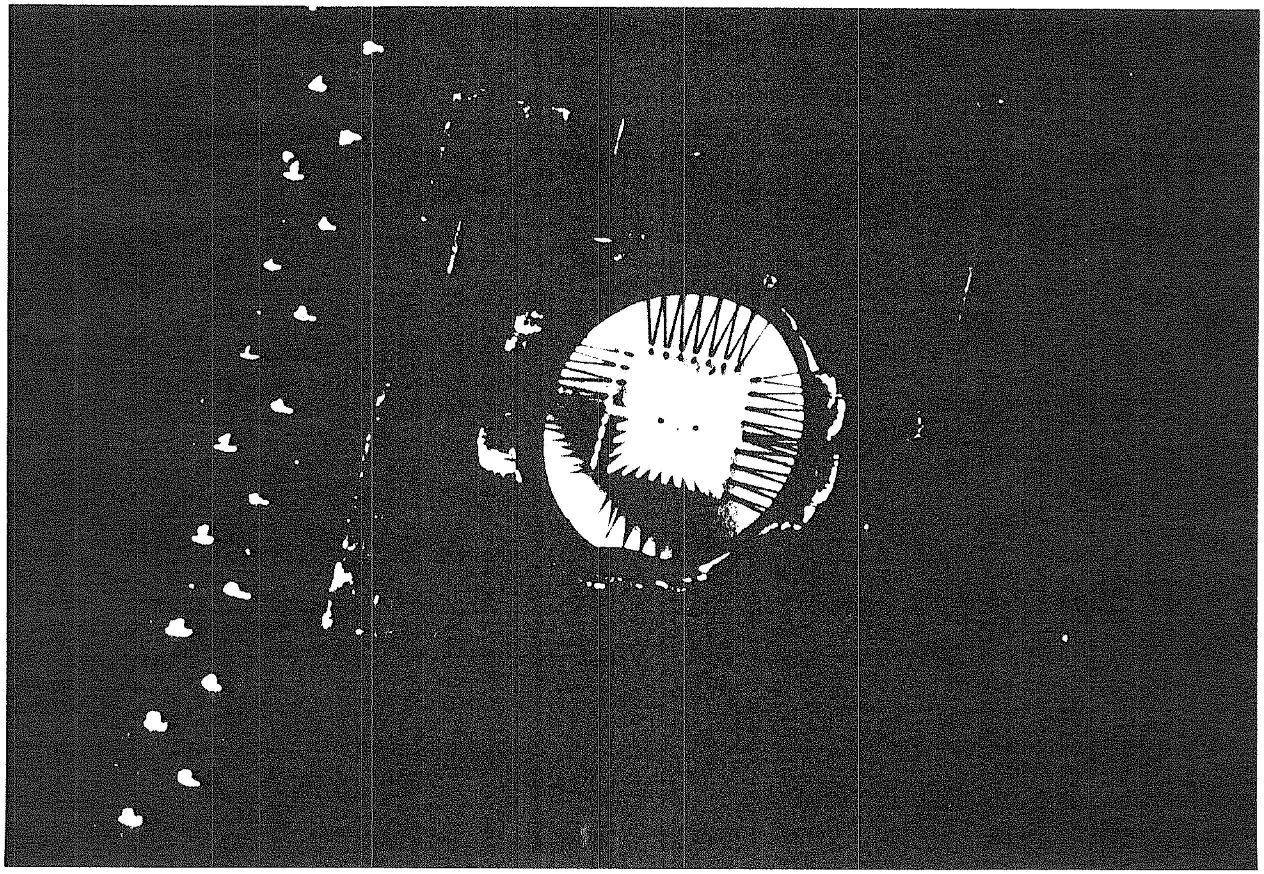

Figure 20: 119µm antenna array mounted in its chip carrier. The sensing line is .75mm long, and is barely visible in the center of the chip.

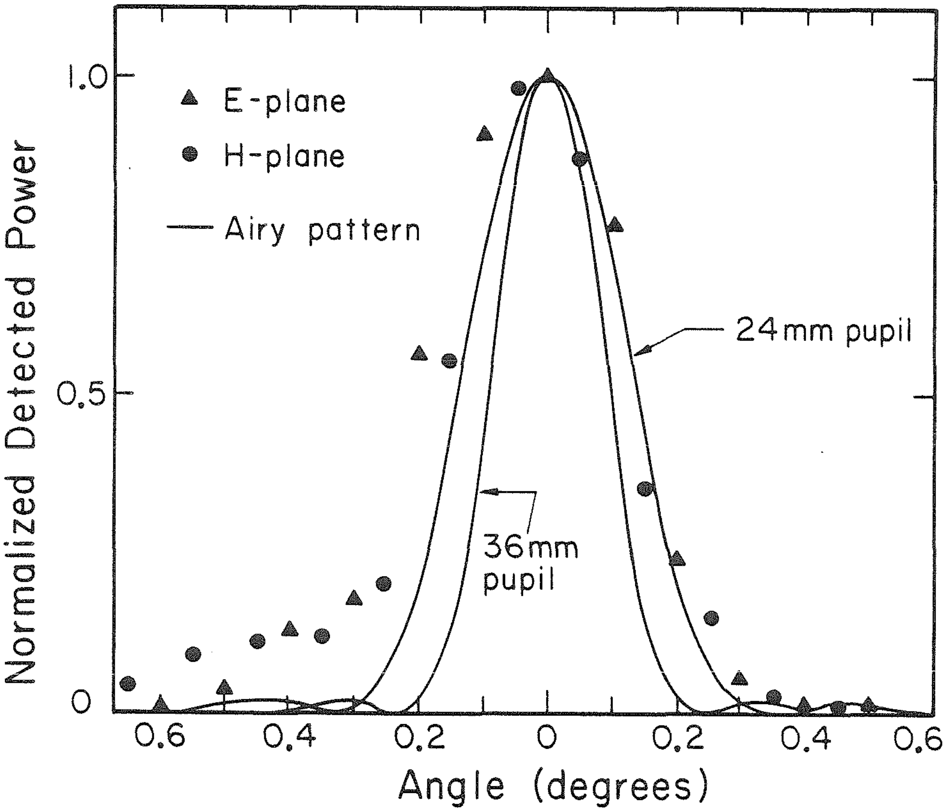

Figure 21: Angular spot response for the 119μm system.

different Airy patterns are also shown in fig. 21. One is found using eq. 30 and a value for l of 36mm, the substrate lens-limited entrance pupil. The other pattern is determined by assuming the antenna pattern limits Θ_1 to a value of 40° (instead of the 73° angle from the substrate lens). This gives, from eqs. 26 and 29, an entrance pupil of 24mm. These comparisons indicate the entrance pupil of this system is probably limited by the antenna beamwidth, which is consistent with the microwave modeling results.

Figure 22 shows the angular field of view for this array and optical system. The full field of view is approximately five degrees, with an angular separation between adjacent antennas of 0.24°. As in the 1.22mm system the field is limited by the small substrate lens used, but in this case the effect is not caused by rays completely missing the lens. Figure 23 illustrates the problem. Shown are the results of a ray-tracing program for rays that are incident at a small angle to the optical axis (as in fig. 14). Because of the small radius of curvature and high index of refraction of the substrate lens rays are incident in the antenna plane at fairly large angles; for example, the main ray incident at 2.5° will be incident in the antenna plane at 26°. This in turn means the response measured from the antenna will be small due to its lower gain at these angles. By increasing the radius of the substrate lens the antenna plane angles decrease, and the field of view should increase. Figure 24 compares the antenna angles for the 3.88mm radius lens and a

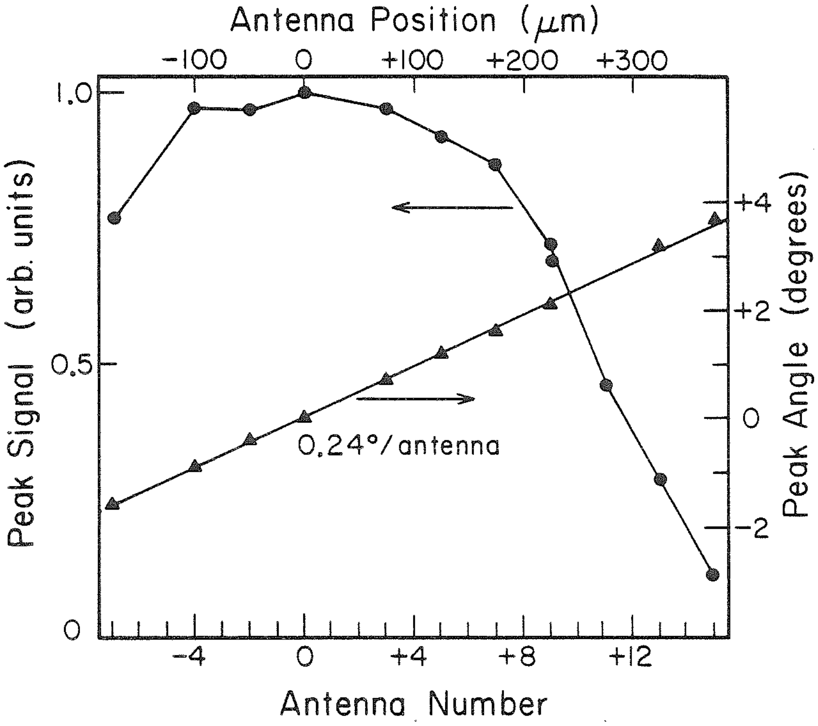

Figure 22: Angular field of view for the 119μm system.

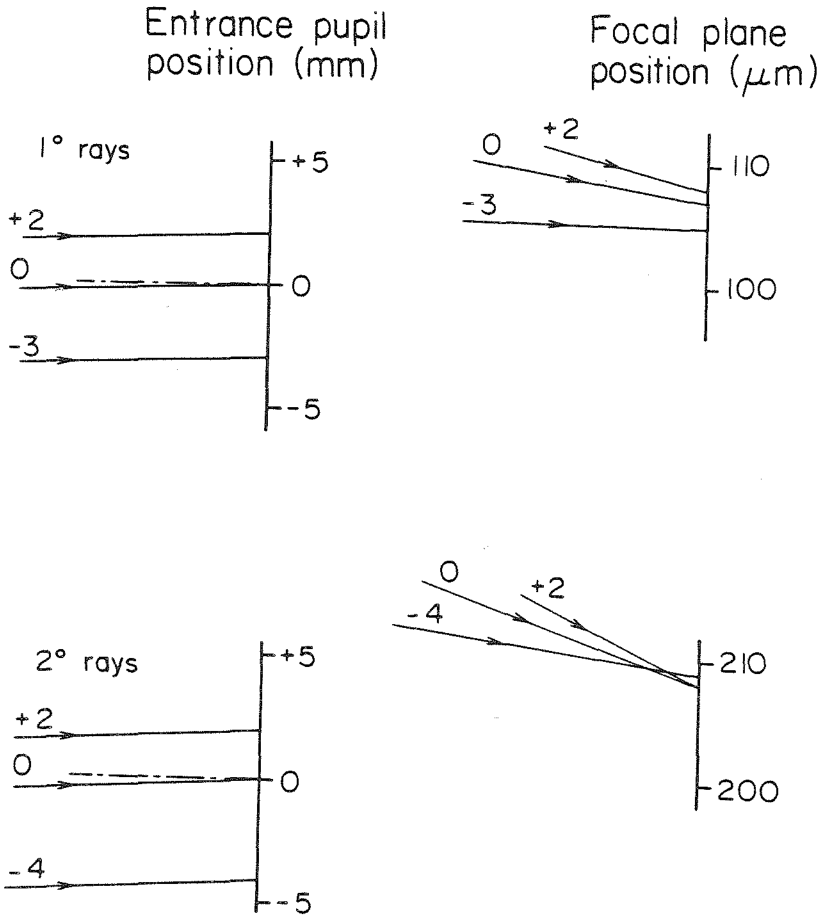

Figure 23: Ray tracing results for the 119μm optical system. The rays are incident from the left at either 1° or 2°; their paths when they reach the antenna plane are indicated on the right.

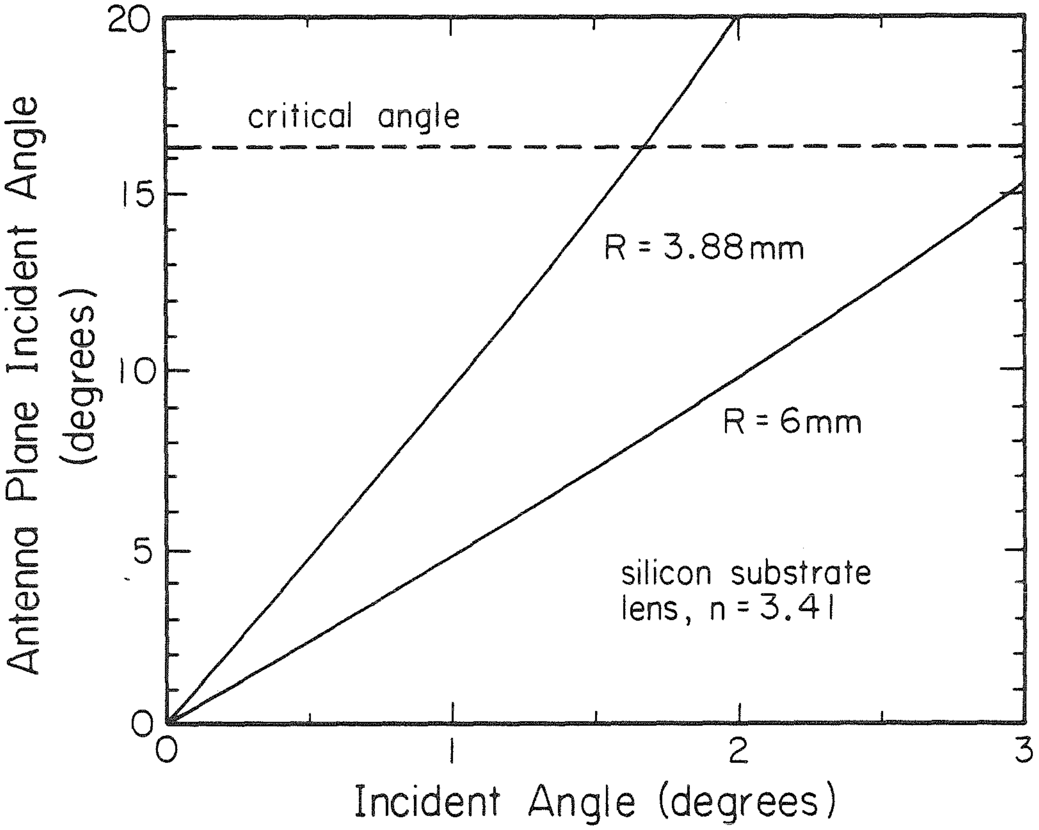

Figure 24: Antenna plane incident angle versus objective lens incident angle for two different radii silicon substrate lenses. The ray traced is the main ray (the ray which passes through the center of the objective lens).

6mm radius lens; the angles are reduced by about a factor of two, so with such a lens the field of view should roughly double.

At 25µm, the sampling interval of this array is designed to match a system f-number of f/1.4 (and therefore an objective lens f/5.1 by eq. 29). In fact, the system used here had an f-number of f/0.5 assuming the substrate lens limited the entrance pupil, or f/0.8 taking an antenna beamwidth-limited $\theta_1 = 40^\circ$. In terms of image reconstruction, then, the resolution of the system is actually limited by sampling, not by either the small substrate lens or antenna beamwidth. A sampling interval of 9µm would actually be required to obtain diffraction limited performance for a f/0.5 system. We can find the effective cut-off frequency f_c by inverting eq. 4b (assuming video detection) and substituting our sampling interval, 25µm,

$$f_c = 1/4T = 10(\mathrm{mm})^{-1} \quad . \tag{33}$$

Using the cut-off frequency given by eq. 2 with $\theta_1 = 73^\circ$ (substrate lens limited) we find $f_o = 27(\mathrm{mm})^{-1}$, or with an angle $\theta_1 = 40^\circ$ (antenna limited), $f_o = 18(\mathrm{mm})^{-1}$. Thus, the resolving power of the system is two to three times lower because of the undersampling. Figure 25 shows an image made with this array and optical system. The object was a bar target with 6mm period, 50cm from the objective lens, illuminated coherently with the 119µm laser. For this object and object distance the fundamental spatial frequency of the image of the target is $13(\mathrm{mm})^{-1}$, slightly higher than the sampling cut-off frequency, but well within the passband of the optical system, whether limited by either the substrate lens or antenna beamwidth. The object was resolved, but the number of samples is just barely adequate for image reconstruction. This demonstrates that when a focal-plane imaging antenna array is operated in a low f-number optical system the overall resolution can be severely limited if the sampling interval of the array is too large.

The efficiency for this system has also been measured, using the same techniques used for the 1.22mm array. The system response at 119µm was found to be about 60 times smaller than the intrinsic detector response. This indicates the optical system-antenna losses were about 18dB. These losses can be accounted for. The TPX used in the objective lens has a measured absorption loss of 4dB/cm. The path length for this lens was 2cm, so 8dB is lost here. The silicon substrate lens is also fairly lossy. For its 5mm path length, using an absorption coefficient of 2dB/cm from Randall and Rawcliffe [32], roughly 1dB is absorbed by the lens. In addition, because of the large index of refraction, another 1.5dB should be reflected off the lens. An attempt to directly measure the power transmitted through the silicon lens was also made: the signal from a 5mm x 5mm pyroelectric detector was recorded with and without the substrate lens in front of it. This indicated a 5.4dB loss. Assuming an intermediate value for the substrate lens loss of 3dB, the

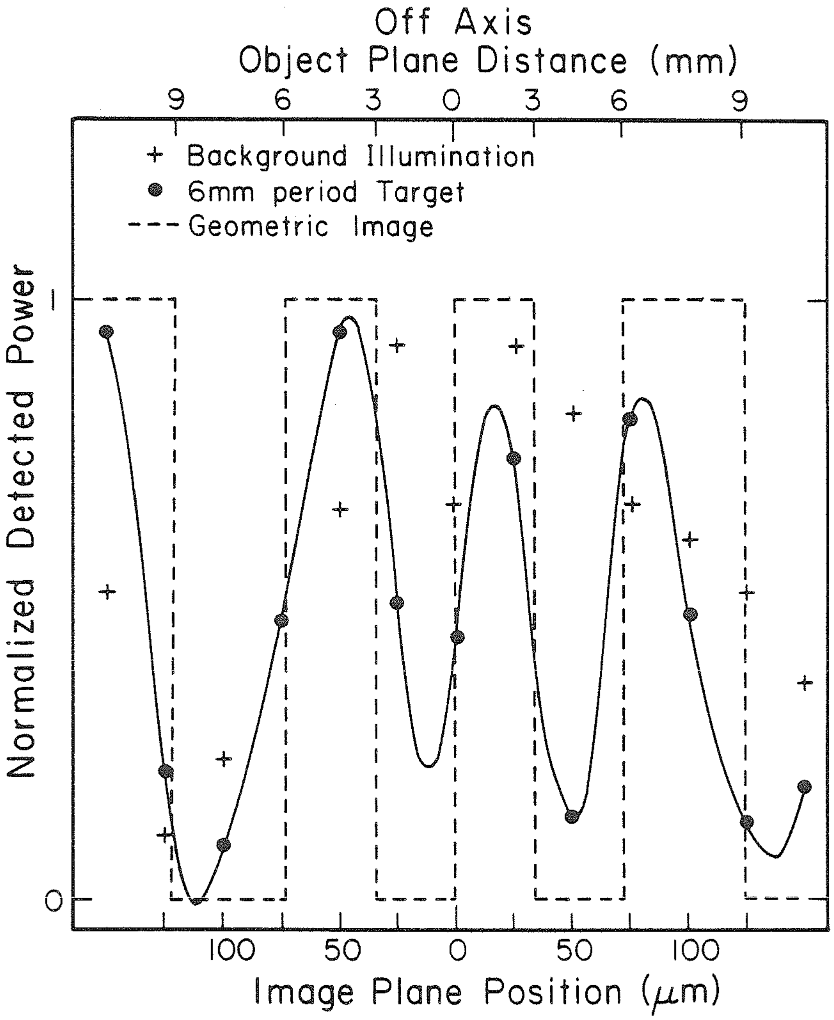

Figure 25: Image of a bar target made with the 119μm array. The solid line is the sinc interpolation from the data points.

remaining system loss is 7dB. This would imply about a 20% coupling efficiency into a single antenna. The main source of loss is clearly the TPX objective lens; the use of reflecting optics should correct this.

References

[1] Rutledge, D.B., and S.E. Schwarz, 'Planar multimode detector arrays for infrared millimeter-wave applications,' IEEE J. Quantum Electron. **QE-17**, 407 (1981).

[2] Gordon, G.A., R.L. Hartman, and P.W. Kruse, 'Imaging-mode operation of active NMMW systems,' in **Infrared and Millimeter Waves**,vol. 4 (K.J. Button and J.C. Wiltse, eds., Academic Press, New York, 1981).

[3] Goodman, J.W., **Introduction to Fourier Optics** (McGraw-Hill, New York, 1968), p. 25.

[4] Born, M., and E. Wolf, **Principles of Optics** (Pergamon Press, 6th ed., Oxford, 1980), p. 484.

[5] Born and Wolf, p.168.

[6] Goodman, p.133.

[7] Gibson, P.J., 'The Vivaldi aerial,' 9th Eur. Microwave Conf., 101 (1979).

[8] Prasad, S.N., and S. Mahapatra, 'A novel MIC slot-line antenna,' 9th Eur. Microwave Conf., 120 (1979).

[9] Rutledge, D.B., S.E. Schwarz, T.L. Hwang, D.J. Angelakos, K.K. Mei, and S. Yokota, 'Antennas and waveguides for far-infrared integrated circuits,' IEEE J. of Quantum Electron. **QE-16**, 508 (1980).

[10] Goodman, pp. 125-133.

[11] Born and Wolf, p. 509, p. 521.

[12] Hollinger, J.P., J.E. Kenney, and B.E. Troy Jr., 'A versatile millimeter-wave imaging system,' IEEE Trans. Microwave Theory Tech. **MTT-24**, 786 (1976).

[13] McGillem, C.D., and T.E. Riemer, 'Moirė patterns and two-dimensional aliasing in line scanner data aquisition systems,' IEEE Trans. Geosci. Electron. **GE-12**, 1 (1974).

[14] Jenkins, F.A., and H.E. White, **Fundamentals of Optics** (4th edition, McGraw-Hill, New York, 1976), p. 192.

[15] Goodman, p. 64.

[16] Oliver, B.M., 'Thermal and quantum noise,' Proceedings of the IEEE **53**, 436 (1965).

[17] Ramo, S., J.R. Whinnery, and T. Van Duzer, **Fields and Waves in Communication Electronics** (John Wiley and Sons, New York, 1965), p. 717.

[18] Brewitt-Taylor, C.R., D.J. Gunton, and H.D. Rees, 'Planar antennas on a dielectric surface,' Electron Lett. **17**, 729 (1981).

[19] Engheta, N., C.H. Papas, and C. Elachi, 'Radiation patterns of interfacial dipole antennas,' Radio Science **17**, 1557 (1982).

[20] Rutledge, D.B., and M.S. Muha, 'Imaging antenna arrays,' IEEE Trans. Antennas and Propagat. **AP-30**, 535 (1982).

[21] Rutledge, D.B., D.P. Neikirk, and D.P. Kasilingam, 'Integrated-Circuit Antennas,' in **Infrared and Millimeter Waves, Vol. 10** (K.J. Button, ed., Academic Press, New York,

1983).

[22] Alexopoulos, N.G., P.B. Katehi, and D.B. Rutledge, 'Substrate optimization for integrated circuit antennas,' IEEE Trans. Microwave Theory and Tech. **MTT-31**, 550 (1983).

[23] Neikirk, D.P., D.B. Rutledge, M.S. Muha, H. Park, and C.-X. Yu, 'Progress in millimeter-wave integrated-circuit imaging antenna arrays,' Proc. SPIE **317**, 206 (1981).

[24] Jenkins and White, pp. 166-167.

[25] Jones, R.C., 'Immersed radiation detectors,' Applied Optics **1**, 607 (1962).

[26] Mons, K.K., and A.J. Sievers, 'Plexiglass: a convenient transmission filter for the FIR spectral region,' Applied Optics **14**, 1054 (1975).

[27] Afsar, M.N., and K.J. Button, 'Millimeter and submillimeter wave measurements of complex optical and dielectric parameters of materials,' Int. J. Infrared and Millimeter Waves **2**, 1029 (1981).

[28] Chantry, G.W., J.W. Fleming, P.M. Smith, M. Cudby, and H.A. Willis, 'Far infrared and millimeter wave absorption spectra of some low-loss polymers,' Chem. Phys. Lett. **10**, 473 (1971).

[29] Born and Wolf, p. 396.

[30] Jenkins and White, p. 330.

[31] Goodman, p. 131.

[32] Randall, C.M., and R.D. Rawcliffe, 'Refractive indices of germanium, silicon, and fused quartz in the far infrared,' Applied Optics **6**, 1889 (1967).

[33] Neikirk, D.P., P.P. Tong, D.B. Rutledge, H. Park, and P.E. Young, 'Imaging antenna array at 119μm,' Appl. Phys. Lett. 41, 329 (1982).

Chapter 3

Microbolometers for Far-Infrared Detection

A microbolometer differs from more conventional thermal detectors because of its physically small size: typically four micrometers square and 100 nm thick. A small device like this has a large thermal impedance, so by using an antenna to couple far-infrared radiation into it large temperature rises can be achieved (fig. 1). This in turn means the microbolometer will have a large responsivity. In addition, since the thermal mass is also small, the detector can be quite fast. Two basic types of bolometers have been made: the air-bridge microbolometer (fig. 2a) [1], and the more conventional substrate-supported bolometer (Fig. 2b) [2]. A variation that takes advantage of the same thermal properties, but avoids the necessity of biasing, is the bismuth-antimony microthermocouple [3].

Thermal Models

The first microbolometers were substrate-supported devices. In these bolometers the conduction of heat out of the detector into both the substrate and the metal antenna structure are important. An exact solution to the thermal diffusion equation is quite difficult since several interrelated conduction pathways are available. The most obvious path is directly into the substrate material. Another important source of heat loss is direct conduction

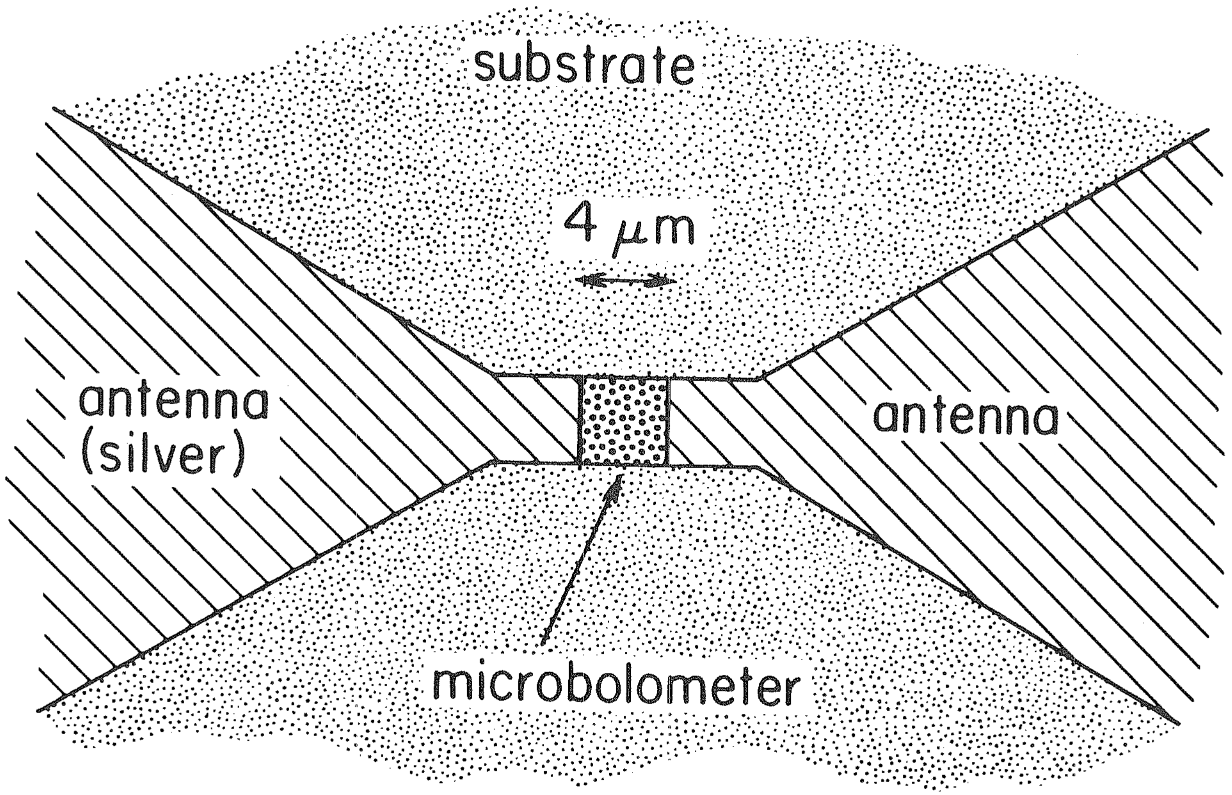

Figure 1: Schematic view of an antenna-coupled microbolometer.

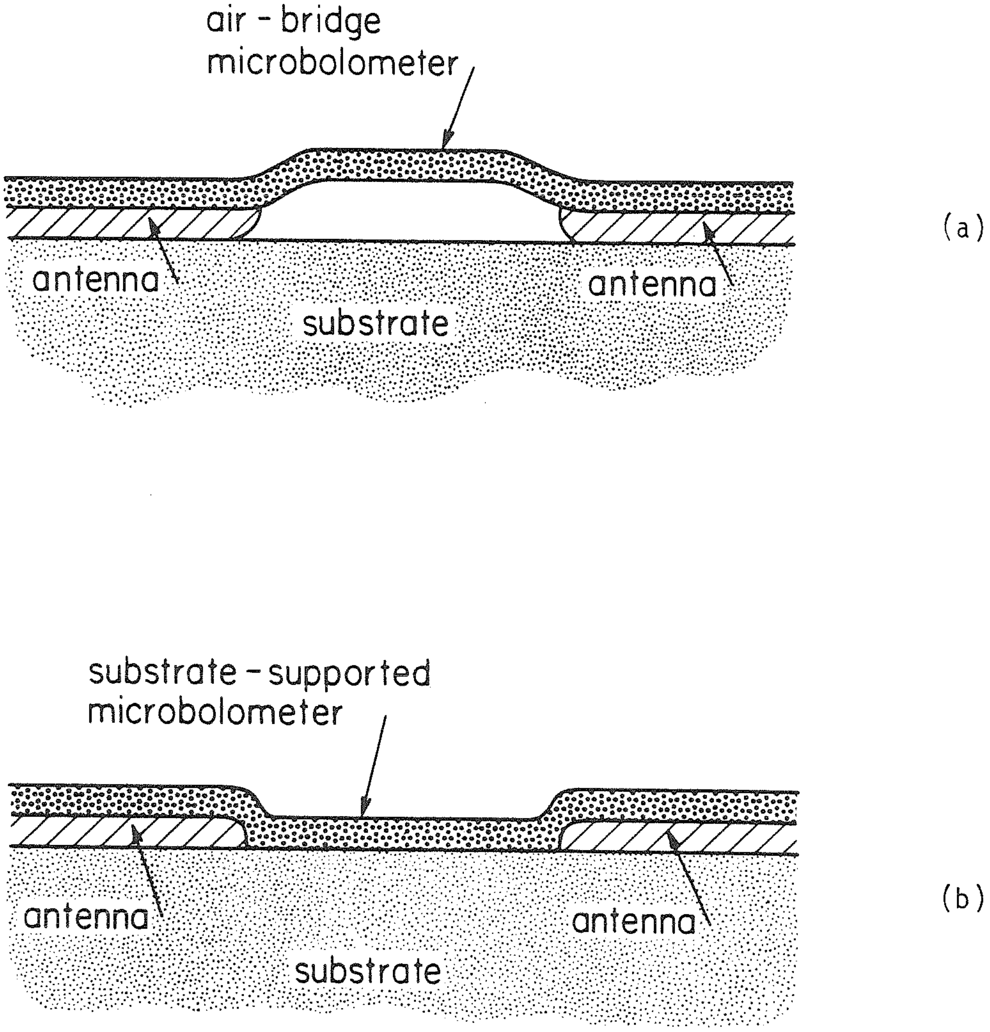

Figure 2: Cross-sectional view of an (a) air-bridge and (b) substrate-supported microbolometer.

into the antenna, which is usually a metal with high electrical conductivity, and therefore very high thermal conductivity. Less obvious, but probably important for small detectors with large antennas, is conduction from the bolometer into the substrate, and from there back into the metal antenna. Finally, if the thermal conductivity of the bolometer material itself is small, this may contribute significantly to heat retention in the bolometer.

The original work by Hwang et al [2] used a considerably simplified but physically helpful thermal model, which we follow here. In order to calculate the conductance into the substrate the presence of the metal antenna is ignored. The contact between bolometer and substrate is taken to be a hemisphere of radius a, which is at a temperature $\phi_o e^{i\omega t}$. The thermal diffusion equation giving the temperature of the substrate is then

$$\frac{1}{r^2}\frac{\partial}{\partial r}\left(r^2\frac{\partial\phi_s}{\partial r}\right) = \frac{\rho_s C_s}{K_s} i\omega\phi_s \tag{1}$$

which is solved subject to the boundary condition that $\phi_s = \phi_o$ for $r = a$. Here K_s is the substrate thermal conductivity, ρ_s its density, and C_s its specific heat. The solution is

$$\phi_s = \phi_o(a/r)\exp[-(r - a)/L_s] \tag{2}$$

where L_s is the complex thermal diffusion length for the substrate, $L_s = (K_s/i\omega\rho_s C_s)^{1/2}$. The total substrate conductance is given by

$$G_s(\omega) = \frac{K_s}{\phi_0} \int_{\text{contact}} \nabla\phi \cdot d\mathbf{s} \qquad (3)$$

which is here

$$G_s(\omega) = 2\pi K_s a(1 + a/L_s) \quad . \qquad (4)$$

The total conductance **G** is taken to be this substrate conductance plus a frequency independent contribution from the metal antenna, G_m. The thermal impedance for the device is then

$$Z_t(\omega) = [G_m + G_s(\omega) + i\omega t w \ell \rho_b C_b]^{-1} \qquad (5)$$

where t is the bolometer thickness, w its width, and ℓ its length; ρ_b is the bolometer material density, and C_b its specific heat. Finally, the responsivity **R** of the detector is given by

$$\mathbf{R} = \alpha |Z_t| V_b \qquad (6)$$

where α is the temperature coefficient of resistance of the bolometer material, and V_b is the dc bias voltage across the device. From eq. 5 we find

$$|Z_t| = \{ [G_{dc} + \pi(2K_s\rho_sC_s\omega)^{1/2}a^2]^2 + [tw\ell\rho_bC_b\omega + \pi(2K_s\rho_sC_s\omega)^{1/2}a^2]^2 \}^{-1/2} \qquad (7)$$

where G_{dc} is the total dc conductance out of the bolometer, due to both the substrate and metal contacts.

Hwang et al [2] have also discussed the frequency response of this type of microbolometer. For low frequencies when $L_s >> a$ (i.e. $f << K_s/2\pi a^2 \rho_s C_s$), the thermal impedance is independent of frequency, and is given by $1/G_{dc}$. At higher frequencies when $L_s << a$ the impedance varies like L_s, that is $f^{-1/2}$. At still higher frequencies the thermal capacitance of the bolometer itself becomes important, and $Z_t \propto f^{-1}$. Note also that both the low frequency response and the speed of the detector increase as the device size decreases. In contrast, as the substrate thermal conductivity decreases the low frequency response increases, but the speed would be expected to decrease.

A microbolometer's performance can be improved by increasing its thermal impedance. The air-bridge bolometer does this by suspending the device in the air above the substrate. The only conduction path is now out the ends of the detector into the metal antenna. We can model this bolometer in a particularly simple manner: a uniform bar of material in which power is dissipated uniformly, and whose ends are attached to perfect heat sinks (the metal of the antenna). The thermal diffusion equation describing the temperature rise ϕ in the device is

$$\frac{\partial^2 \phi}{\partial x^2} = \frac{\rho_b C_b}{K_b} \frac{\partial \phi}{\partial t} - \frac{P_o}{2tw\ell K_b}(1 + e^{i\omega t}) \qquad (8)$$

where ρ_b, C_b, t, w, and ℓ are defined as before, K_b is the bolometer material thermal conductivity, and P_o is the peak power dissipated in the bolometer. This equation is solved subject to the boundary condition that ϕ is zero at the ends of the detector. The solution is integrated over x to obtain the average temperature rise in the device

$$\langle \phi \rangle = \frac{P_o}{24twK_b}\left[1 + 24\left(\frac{L_b}{\ell}\right)^3\left(\frac{\ell}{2L_b} - \tanh\frac{\ell}{2L_b}\right)e^{i\omega t}\right] \qquad (9)$$

where L_b is the thermal diffusion length in the bolometer material, $L_b = (K_b/i\omega\rho_bC_b)^{1/2}$. The ratio of the time-varying temperature and time-varying power yields the thermal impedance of the air-bridge bolometer,

$$Z_t(\omega) = 2\frac{\ell}{twK_b}\left(\frac{L_b}{\ell}\right)^3\left(\frac{\ell}{2L_b} - \tanh\frac{\ell}{2L_b}\right) \quad . \qquad (10)$$

It is possible to plot a universal frequency response curve for the air-bridge bolometer, as shown in fig. 3. For low frequencies when the thermal diffusion length L_b is much larger than the bolometer length ℓ(i.e. $f < K_b/2\pi\ell^2\rho_bC_b$) the thermal impedance is independent of frequency, and $Z_t = \ell/12K_btw$. At high frequencies L_b becomes much smaller than ℓ, and $Z_t = 1/i\omega\ell tw\rho_bC_b$. These are the same limiting values as a thermal circuit consisting of a resistance $\ell/12K_btw$ in parallel with a thermal capacitance $\ell tw\rho_bC_b$. Unlike the substrate-supported bolometers, the air-bridge response changes quite abruptly from flat to a 1/f roll-off. The speed of the detector is determined by $(R_tC_t)^{-1}$, which is $12K_b/\rho_bC_b\ell^2$. Note that the speed depends on only one dimension of the bolometer, the length ℓ. It should also be noted that for fixed dimensions the thermal conductance

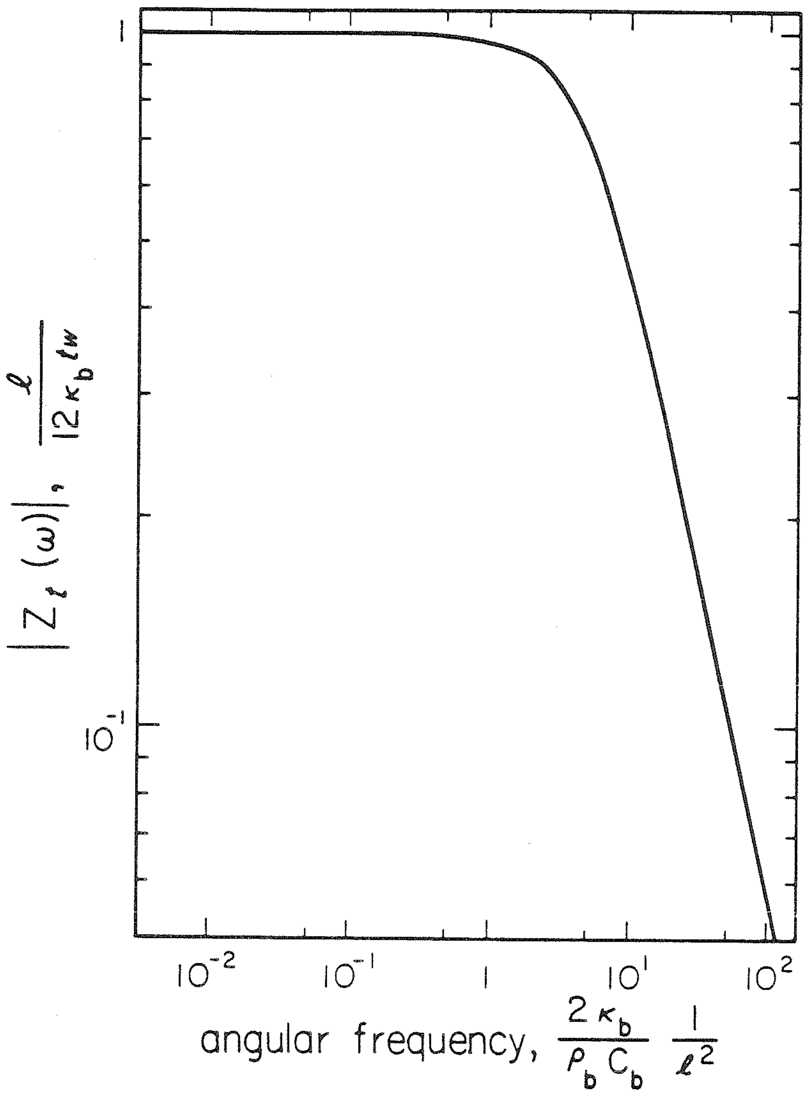

Figure 3: Frequency response curve of an air-bridge microbolometer. The speed depends on only one device dimension, the length ℓ .

out of an air-bridge bolometer is always less than that out of a substrate-supported device.

Materials for Antenna-coupled Bolometers

The choice of a material for use in a microbolometer is strongly dependent on the electrical impedance desired. If we assume that the antenna is best matched by a resistance R_a, for a material with electrical conductivity σ we must have device dimensions that satisfy

$$\ell/(tw) = \sigma R_a \quad . \tag{11}$$

At the same time we want to maximize the thermal resistance to increase the detector response. For an air-bridge bolometer we found that the thermal resistance is proportional to ℓ/twK_b, but using eq. 11 this is just $\sigma R_a/K_b$. Since R_a is fixed by the antenna we should use a material which gives a large value for σ/K_b.

The ratio of the electrical conductivity to the thermal conductivity, σ/K, is very nearly the same constant for most metals; the two properties are fundamentally related. This relation is embodied in the Wiedemann-Franz law, which gives

$$\frac{\sigma}{K} = \frac{3}{\pi^2}\left(\frac{e}{k_B}\right)^2\frac{1}{T} \tag{12}$$

where k_B is Boltzmann's constant, e the electron charge, and T the absolute temperature [4]. Because of this, for fixed device resistance, almost all metals would give the same bolometer thermal resistance.

The other material constant that enters into the responsivity of the detector is the temperature coefficient of resistance α; the larger α the larger the responsivity. Once again, however, this is very nearly the same for all metals. Since the resistivity ρ of most metals near room temperature is proportional to temperature, and using the definition of α,

$$\alpha = \frac{1}{\rho} \frac{d\rho}{dT} \tag{13}$$

we find that $\alpha = 1/T$ [5]. For 300 K this gives a temperature coefficient of about $0.003 K^{-1}$; almost every metallic element is within a factor of two of this value.

A search for materials with a large temperature coefficient α usually leads to a consideration of semiconducting materials. For intrinsic semiconductors the carrier concentration varies exponentially with temperature, and their resistivity is proportional to $\exp(E_g/2kT)$. This gives $\alpha = -E_g/2kT^2$, where E_g is the band gap of the material. At room temperature for a 1 eV band gap this is about $0.06 K^{-1}$, about twenty times larger than that of a metal. Unfortunately this increase in α is more than offset by a decrease in the material conductivity σ, since the quantity we must really maximize is $\alpha\sigma/K$. The conductivity in an intrinsic semiconductor is usually 10^3 to 10^6 times smaller than that of a typical metal, with a thermal conductivity 2 to 10 times smaller. This yields a figure of merit $\alpha\sigma/K$ that is actually smaller than a typical metal. If the semiconductor is doped to increase its conductivity the resistivity is no longer proportional to $\exp(E_g/2kT)$. The carrier concentration is now set by the dopant concentration, and is only weakly temperature dependent at room temperature. From fairly basic considerations, then, a semiconducting material is unlikely to provide any advantages as a microbolometer material.

It would seem that almost any metallic material would make an equally good bolometer. There is one practical constraint, however, that has not been addressed. Generally the smaller the dimensions of a bolometer the better. Using a photolithographic process capable of producing a minimum feature size w_{min}, the best microbolometer will be roughly w_{min} wide and w_{min} long (i.e. one square). Since the desired resistance is R_a, we must have a thickness that yields a resistance per square of R_a. There is usually a minimum thickness, t_{min}, below which good evaporated layers are very difficult to produce, so the conductivity is constrained by

$$\sigma < (R_a t_{min})^{-1} \quad . \tag{14}$$

For a typical matching resistance of 100Ω and minimum thickness of 20nm this gives $\sigma < 5\text{x}10^3\ (\Omega\text{cm})^{-1}$. In comparison, the conductivity of copper is $6\text{x}10^5\ (\Omega\text{cm})^{-1}$, and for lead is $4.8\text{x}10^4\ (\Omega\text{cm})^{-1}$. This constraint is therefore quite serious, eliminating all the more common metals.

An examination of the elements shows very few with a conductivity low enough to satisfy the restriction above. Since it is also advantageous to avoid extremely large thicknesses (which increase the thermal mass and complicate the fabrication process), we can also find a lower bound on σ. Assuming this maximum thickness to be 0.5 μm, the minimum conductivity is approximately 200 $(\Omega\text{cm})^{-1}$. This eliminates several of the elements that satisfied eq. 14. One material which does cover this range of conductivities is thin-film bismuth.

The properties of thin-film bismuth are quite different from those of the bulk material. Its conductivity is typically two to ten times lower than the bulk, falling into the range desired for a microbolometer. The exact value of its conductivity depends on film thickness, substrate material, and substrate temperature during deposition, and somewhat less on evaporation rate. Table 1 summarizes some of the published data on thin-film bismuth. The range of resistivities obtained by different authors is fairly large, but under our deposition conditions we have found our values of the resistivity to be repeatable.

Both the resistivity and its temperature dependence were measured for several thicknesses of bismuth; representative values are shown in fig. 4. For the measurement silver or gold contact pads 100nm thick were first evaporated on glass substrates, leaving a 12.5mm space between them. Bismuth was then evaporated through a metal mask to leave a strip 2.5mm wide connecting the two contacts. The substrate was at room

Table I: REPORTED LITERATURE PROPERTIES OF THIN FILM BISMUTH

	Colombani and Huet [6]	Komnik et al [7]	Abrosimov et al [8]	Kawazu et al [9]	Joglekar et al [10]	this study
Substrate	Bi_2O_3	cleaved mica	polymer	(111) Si	glass	glass
substrate temperature	20^0C	80-110^0C	106^0C	100^0C	20^0C	20^0C
deposition rate		1-5 Å/sec	22 Å/sec	5 Å/sec	2 Å/sec	1-5 Å/sec
annealing	>300^0C	200^0C	none	none	none	100^0C +
crystal structure, grain size		mosaic single crystal	poly, 200-800 nm	poly, 200-300 nm	poly, 100 nm	poly, 100 nm
thicknesses	20-300 nm	75-500 nm	100-800 nm	100-3000 nm	20-100 nm	100-400 nm
resistivity at 20 °C	before anneal: 540 μΩ-cm after: 200μΩ-cm	200 nm: 260-100 μΩ-cm	100 nm: 300 μΩ-cm 200 nm: 150 μΩ-cm	200 nm: 200 μΩ-cm 500 nm: 160 μΩ-cm	100 nm: 1000 μΩ-cm	100 nm: 685 μΩ-cm 400 nm: 390 μΩ-cm

+ no irreversible change in resistivity for temperatures of 20-100^0C.

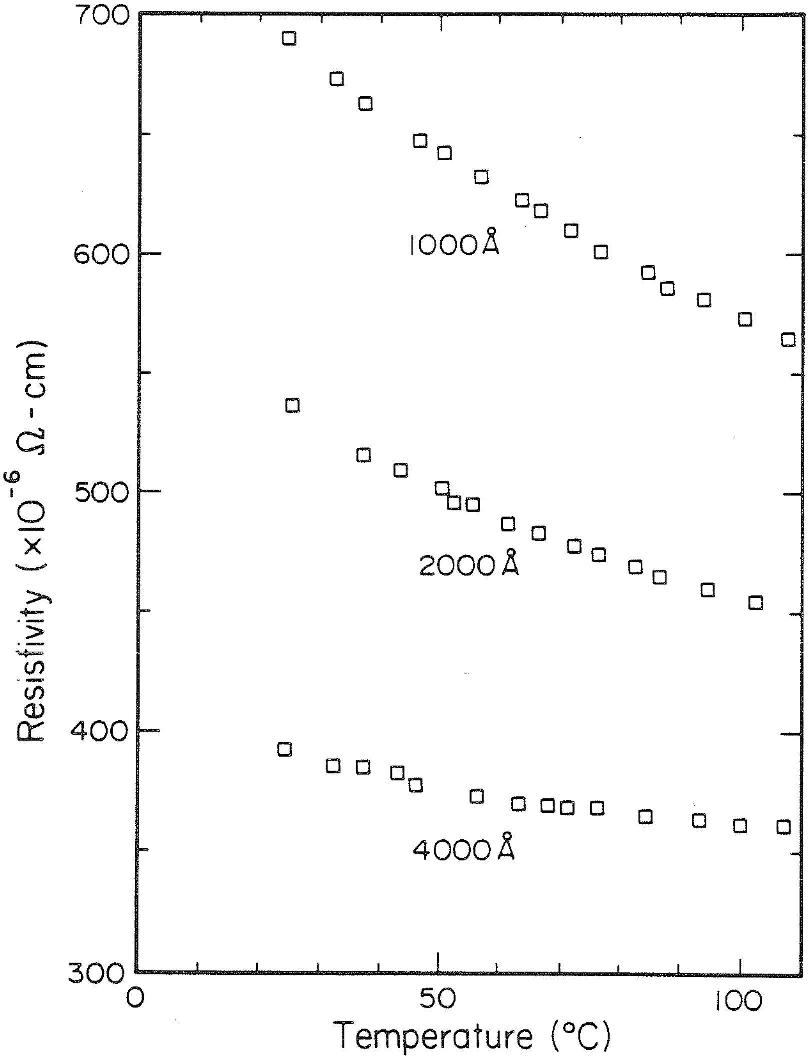

Figure 4: Resistivity versus temperature for several thicknesses of thin film bismuth.

temperature during the evaporation, which was done at a rate of 0.1-0.5nm/sec. The thickness was monitored with a crystal quartz thickness monitor. Resistance versus temperature measurements were done by soldering wire leads to the contacts, immersing the assembly in an oil bath, and placing the oil bath in an oven. The temperature of the oil bath was measured, and the resistance of the bismuth strip measured with a digital ohmmeter. Sample to sample variations were less than 2%. Note that the temperature coefficient of resistance for these bismuth films is negative, as has been discussed by Komnik et al [7]. Of practical interest for a microbolometer is the decrease in α from about $0.003K^{-1}$ at 100nm thickness to $0.0015K^{-1}$ at 400nm. In addition, the resistance per square for 100nm films is 69Ω, a convenient value for antenna matching.

Fabrication

Bismuth microbolometers have been made in several different ways. These techniques fall into two general categories, the two-step process and the single-step process. In a two-step process the antenna metalization is first defined. The bolometer photoresist pattern is then aligned to the antenna, the bismuth evaporated, and finally the lift-off performed. Single-step processing uses a photoresist-bridge [11][12][chapter 4] or groove [13] so that both the antenna and the bolometer can be formed with a single pattern in one vacuum evaporation step.

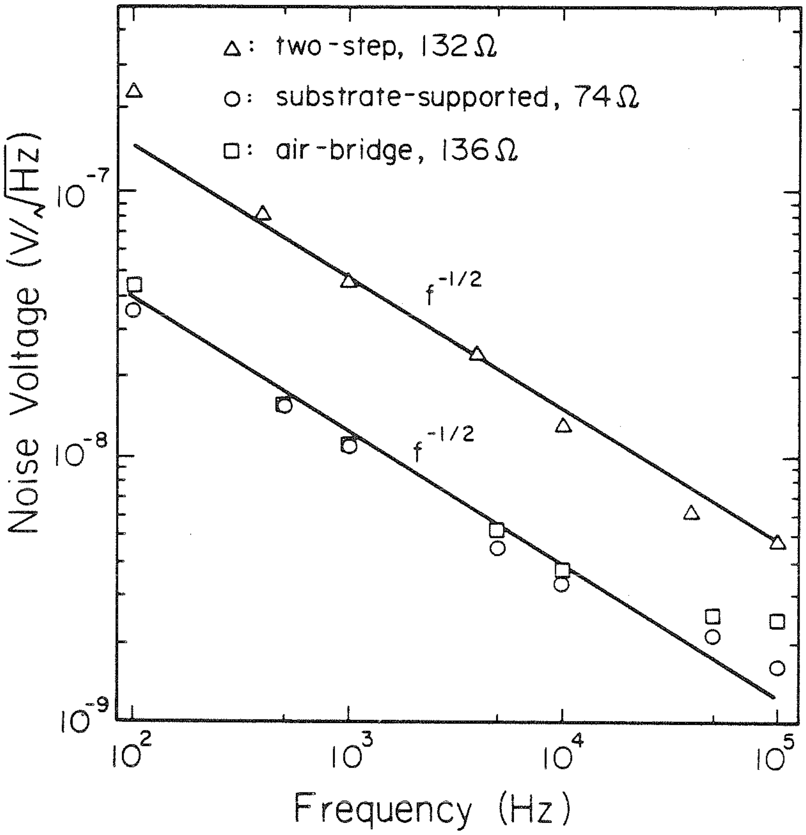

Figure 5: Noise spectra for air-bridge, substrate-supported, and two-step fabricated bismuth bolometers. The bias voltage across the devices was 0.1V.

Two-step processing has two major disadvantages. The first of these is technological: for small antennas and small detectors the alignment between them becomes very critical. The second is more fundamental: as shown in fig. 5 the low frequency 1/f-noise in a two-step bolometer is about four times larger than in a single-step detector. This is probably due to contamination of the first level metalization during the second photolithographic step.

The photoresist-bridge technique has been widely used to fabricate a variety of devices [14][15]. Figure 6 shows the general principle, and fig. 7 shows an SEM of a typical bridge. In this process the detector is formed under a bridge (which separates the two sides of the antenna metalization) by evaporating bismuth at an angle from both sides of the bridge. By evaporating different materials from each side it is also possible to form bi-metallic junctions, such as the bismuth-antimony thermocouple (fig. 8)[3]. Note that this type of process is self-registering; that is, the bolometer is aligned precisely to the antenna since the same photoresist structure patterns both .

A somewhat more elaborate bridge process is used to fabricate the air-bridge microbolometer. In the usual process the bridge is suspended above the substrate by another layer of uniformly exposed photoresist. This layer is then undercut during development to leave the bridge above the substrate. In order to make the air-bridge bolometer three layers of resist are used, with only the

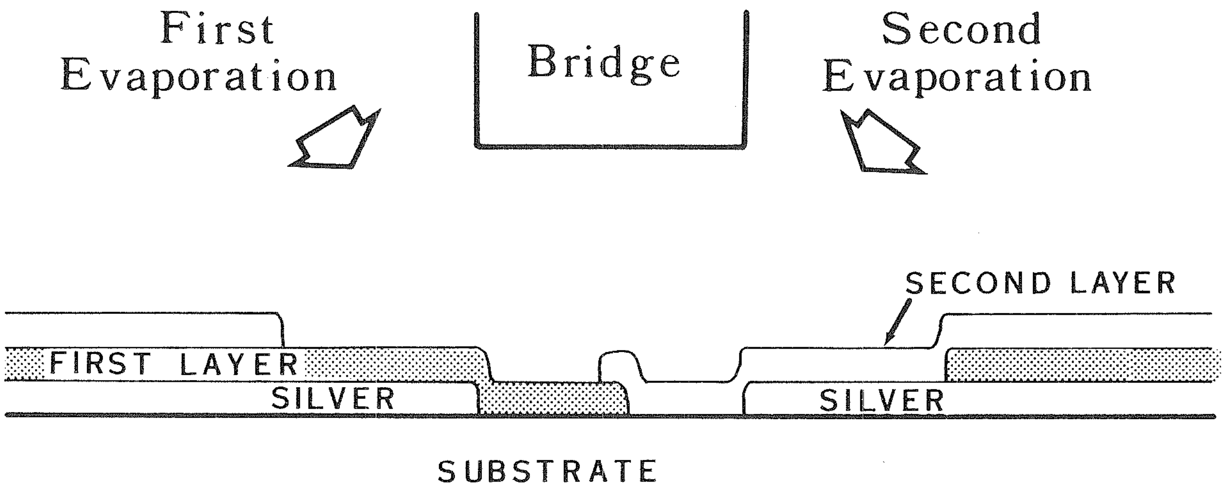

Figure 6: Illustration of the photoresist bridge fabrication technique. The antenna metalization (silver) is evaporated at normal incidence, followed by evaporation of the detector materials.

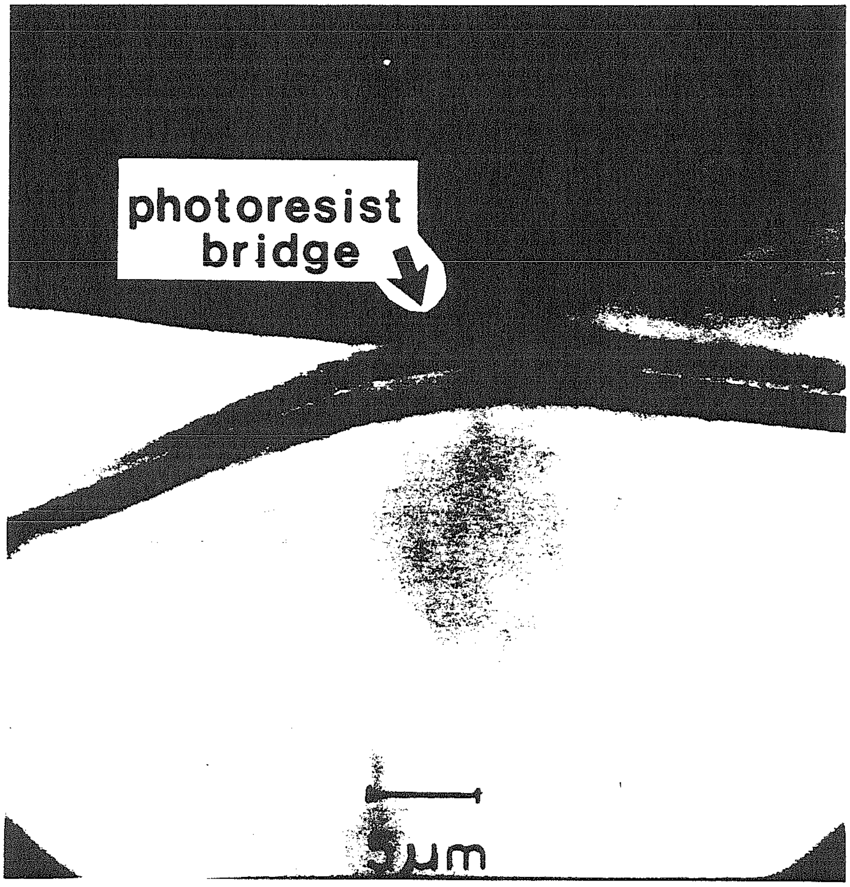

Figure 7: Photoresist bridge supported about 2µm above the substrate surface.

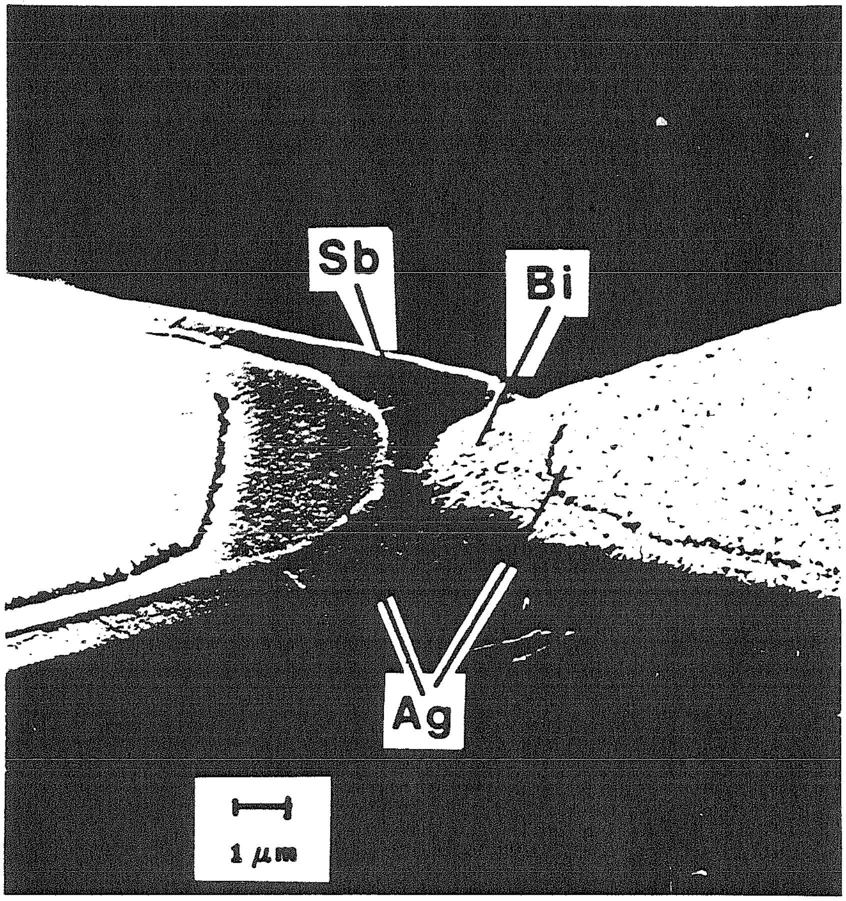

Figure 8: Bismuth-antimony microthermocouple.

middle layer flood exposed. Since we use transparent plasma-formed buffer layers [16][chapter 4] when the tri-layer resist is contact printed to form the bridge pattern an identical pattern is produced in the bottom layer. A finished photoresist structure is shown in fig. 9. The antenna is formed by evaporating silver at normal incidence to the substrate. Bismuth is then evaporated at a 50^o angle from each side of the bridge. The bolometer is thus formed under the bridge, but is supported above the substrate by the bottom resist layer (fig. 10). After evaporation the substrate is soaked in acetone for approximately one hour, which dissolves all the photoresist. Unwanted metal on the top layer of resist is removed, and the bolometer is left suspended by its ends above the substrate when the resist below it dissolves away. A finished air-bridge detector is shown in fig. 11.

Figure 12 shows the groove-fabrication process for substrate-supported bolometers. By using steep-angle evaporation of the antenna metal shadows are cast across narrow grooves connecting the two sides of the antenna. Bismuth is then evaporated at normal incidence to complete the connection. This process does allow the bismuth to be deposited at normal incidence, which tends to produce slightly better quality films. However, due to lithographic difficulties, the grooves are several times longer than they are wide. The bolometers are then somewhat larger than those

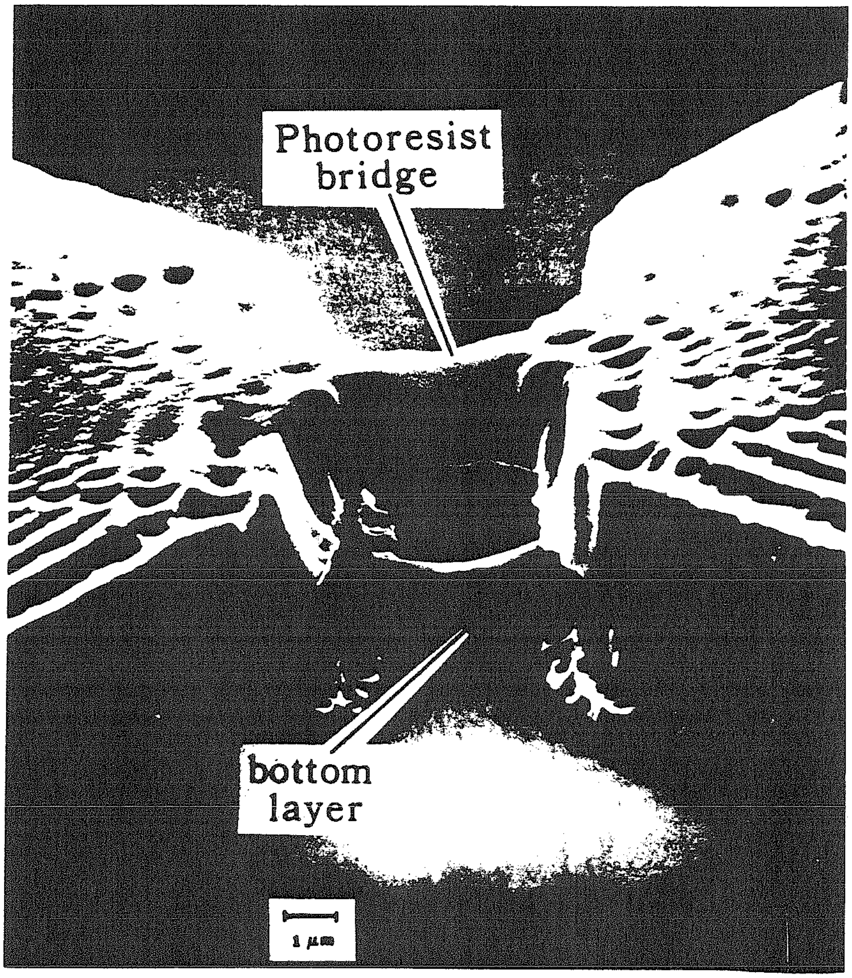

Figure 9: Photoresist bridge used to fabricate the air-bridge bolometer. The bottom layer is about 0.5μm thick, and the bridge is about 2μm above it.

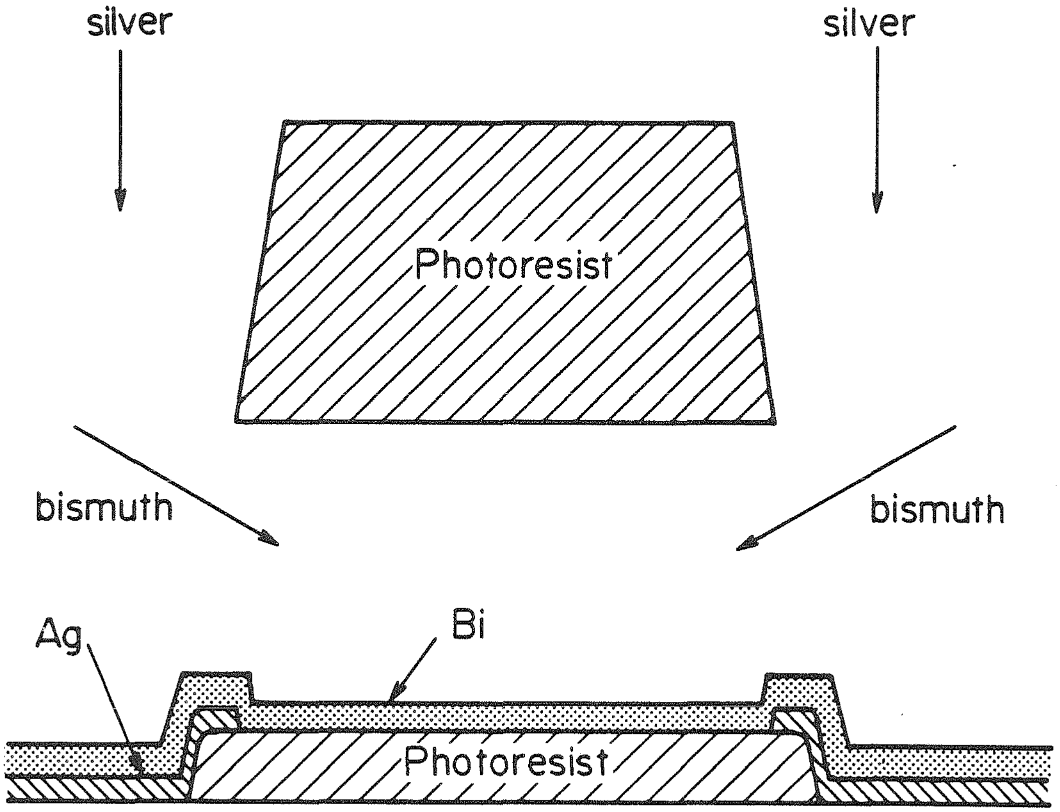

Figure 10: Evaporation sequence for the air-bridge microbolometer showing the photoresist pattern that supports the detector.

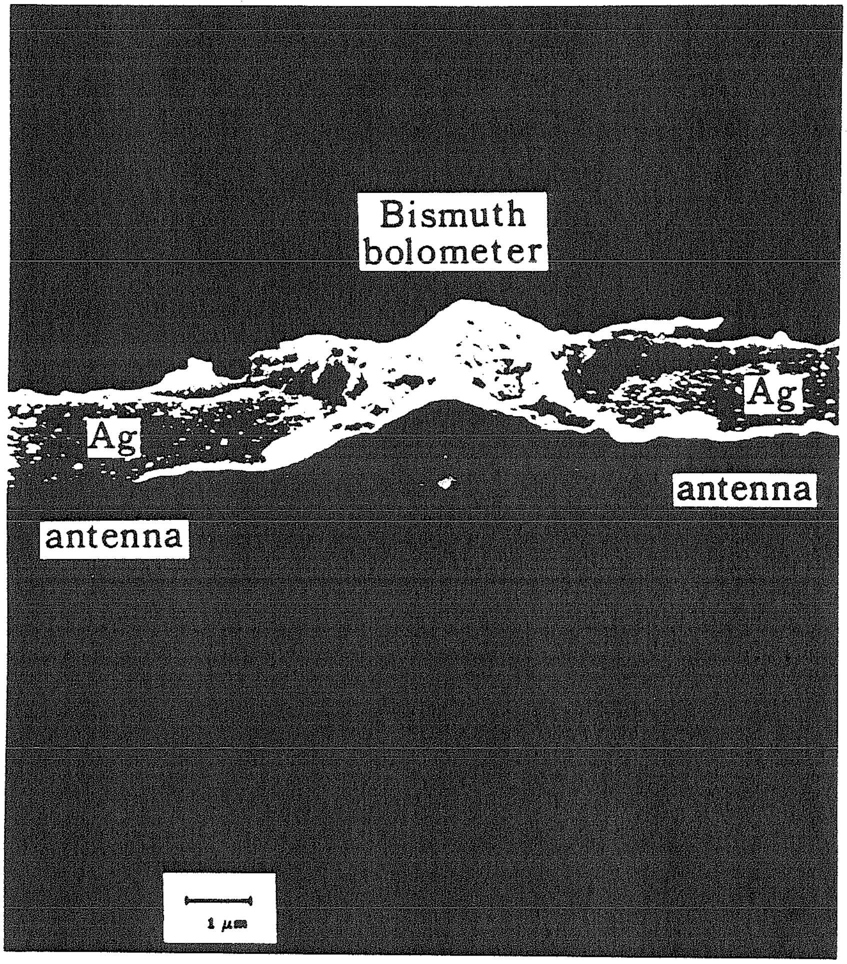

Figure 11: SEM of a finished air-bridge microbolometer.

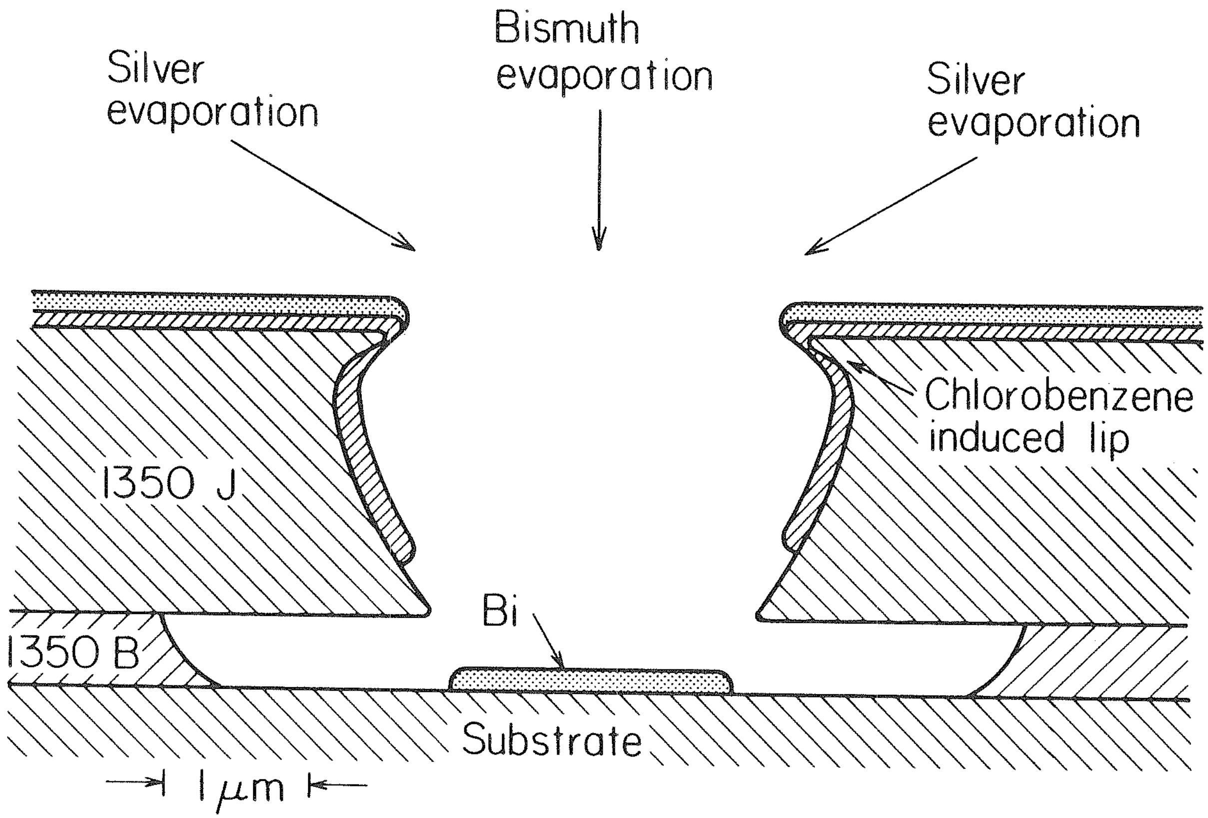

Figure 12: Groove fabrication process. The angle of the silver evaporation is chosen so no silver is deposited in the groove.

normally made with the bridge process, and are therefore less responsive.

Electrical Testing

Unlike many far-infrared detectors it is possible to accurately calibrate the bismuth microbolometer. This is done by first measuring the dc responsivity of the bolometer from its dc I-V curve. An ideal bolometer has a resistance that is just a linear function of the power dissipated in it,

$$R = R_o + \beta P \quad . \tag{15}$$

The voltage responsivity $\mathcal{R}$ of such a device with a constant bias current I_b applied to it is then

$$\mathcal{R}_{dc} = I_b \frac{dR}{dP} = I_b \beta \quad . \tag{16}$$

We can find β and R_o by measuring the dc I-V curve of the bolometer, since eq. 15 gives

$$(V/I) = R_o + \beta VI \quad . \tag{17}$$

Figure 13 shows a typical R-P plot for an air-bridge bolometer, along with the linear regression fit to the data; the correlation coefficients for these fits are usually better than 0.999. Note that we can also find the dc thermal impedance of the device once β is known using

$$| Z_{dc} | = \mathcal{R}_{dc}/(\alpha V_b) = I_b\beta/(\alpha V_b) \quad . \tag{18}$$

The frequency response of the microbolometer is found using the rf network shown in fig. 14. The circuit applies a 150MHz signal which is amplitude modulated at a frequency Δf.

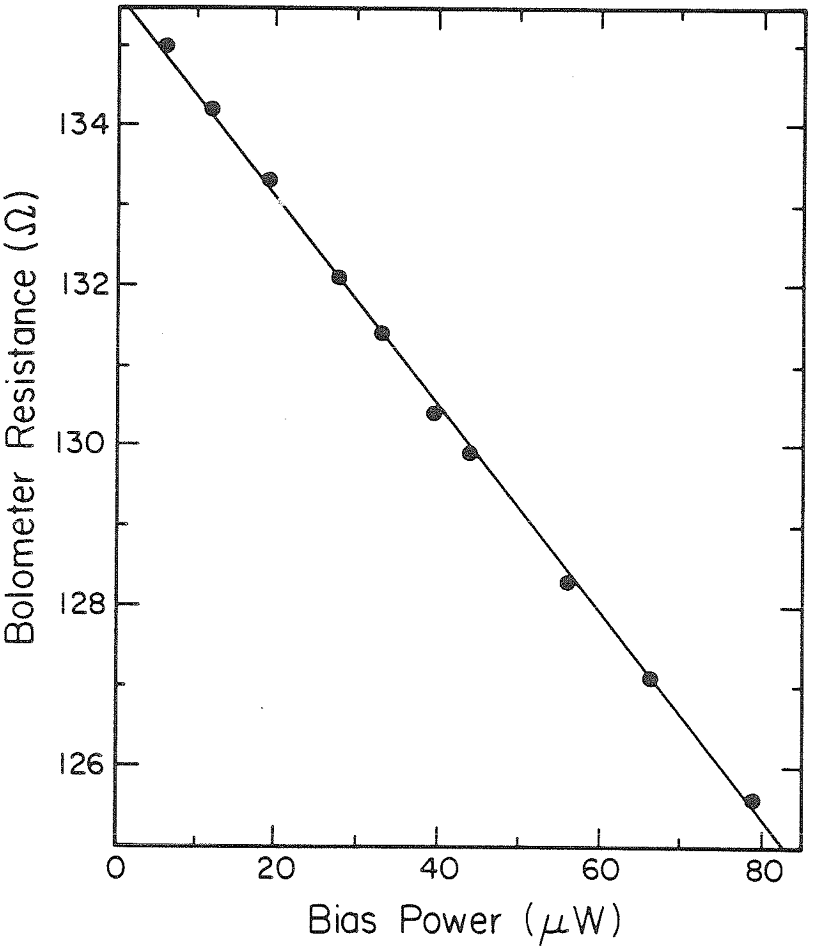

Figure 13: Resistance versus bias power for an air-bridge bolometer. The slope of the line multiplied by the bias current gives the detector responsivity.

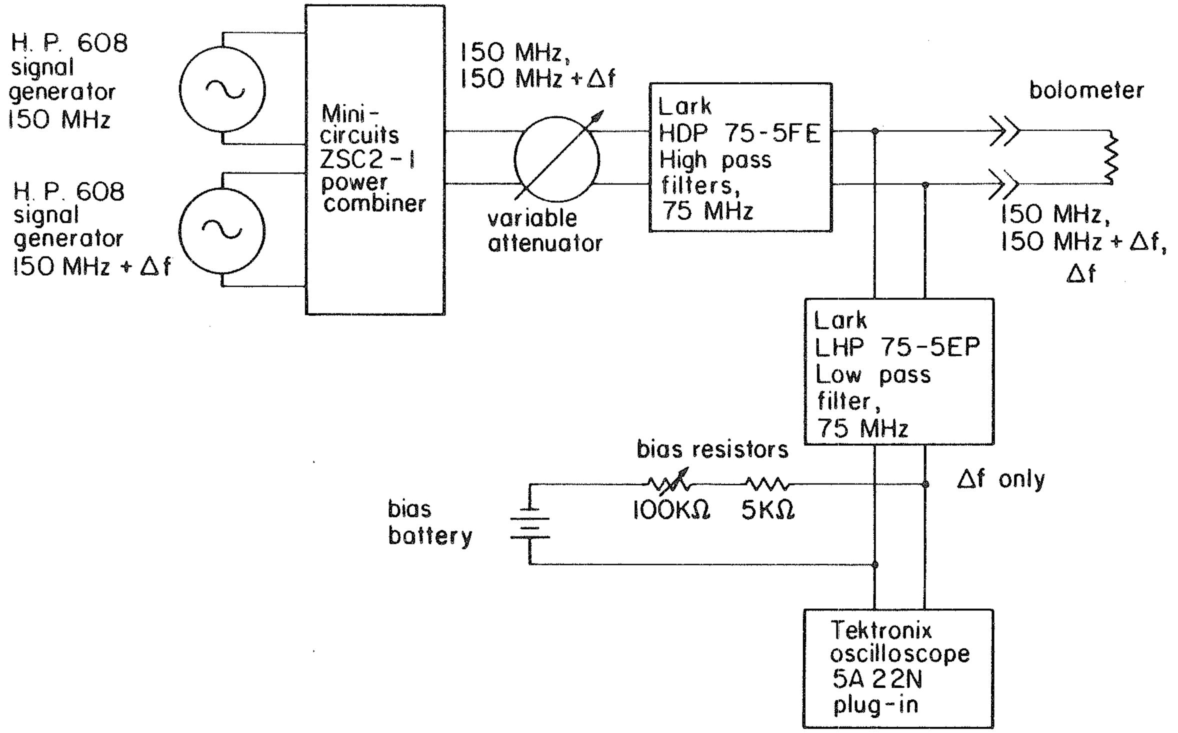

Figure 14: RF circuit used to measure bolometer frequency response.

The bolometer is too slow to respond to the 150MHz signal, and sees it as a modulated power input (the detector is now functioning just as it does in the far-infrared). By varying Δf and measuring the output signal from the detector its response curve is determined. In order to make an absolute measurement of the responsivity the rf power absorbed must be known. This is quite difficult to measure accurately. By placing a directional coupler in the input arm of the network reflections off the bolometer and its mount can be measured. For a device with a 50Ω resistance the reflection is typically 10dB down, but for larger resistances or a bad device mount the reflection may be quite large (up to 3dB). When reflections are taken into account the responsivities from the rf network are consistent with those determined from the dc R-P curve. The response curves are therefore normalized to the dc R-P responsivity, which can be measured quite accurately.

Bismuth Microbolometers

Figure 15 shows typical measured responsivities at 0.1V bias for both an air-bridge and a substrate-supported bolometer. The substrates were Pyrex glass microscope slides. Both detectors were 4μm long, 3.5μm wide, and 100nm thick. The substrate-supported bolometer was fabricated in exactly the same way as the air-bridge, but the bottom layer of resist was omitted. Electrical contacts to the bolometer were silver bow-tie antennas 100nm thick. The air-bridge had a resistance of 136Ω, and the substrate-supported bolometer 74Ω. Device to device variations in response on the same chip were about 10%.

For the air-bridge microbolometer all the physical constants and device dimensions in the thermal model are known, with the exception of the thermal conductivity of thin-film bismuth. As discussed earlier, the electrical properties of bismuth films are strongly dependent on thickness and deposition conditions, and Abrosimov et al [8] report similar effects for thermal properties. For this reason K_b is treated as an adjustable parameter, and eqs. 6 and 10 are then used to fit the measured responsivity. The thermal conductivity K_b can be found from the dc responsivity,

$$K_b = \alpha V_b \ell/(12R_{dc}tw) \quad . \tag{19}$$

For the device in fig. 15 $\alpha = -0.003K^{-1}$, $V_b = 0.1V$, $\ell/tw = 11.5\mu m^{-1}$, and $R_{dc} = 99V/W$, which gives a thermal conductivity of $2.9W(m\ K)^{-1}$. This value is about three times lower than bulk bismuth, but twice the value given by Abrosimov et al [8] for 100nm thick films. The excellent agreement between the measured high frequency responsivity and the predicted response with this value of K indicates that the simple thermal model used is valid for the air-bridge bolometer.

The model used for predicting the response of the substrate-supported bolometer is less exact than that of the air-bridge. The fitted line in fig. 15 is found using eq. 7

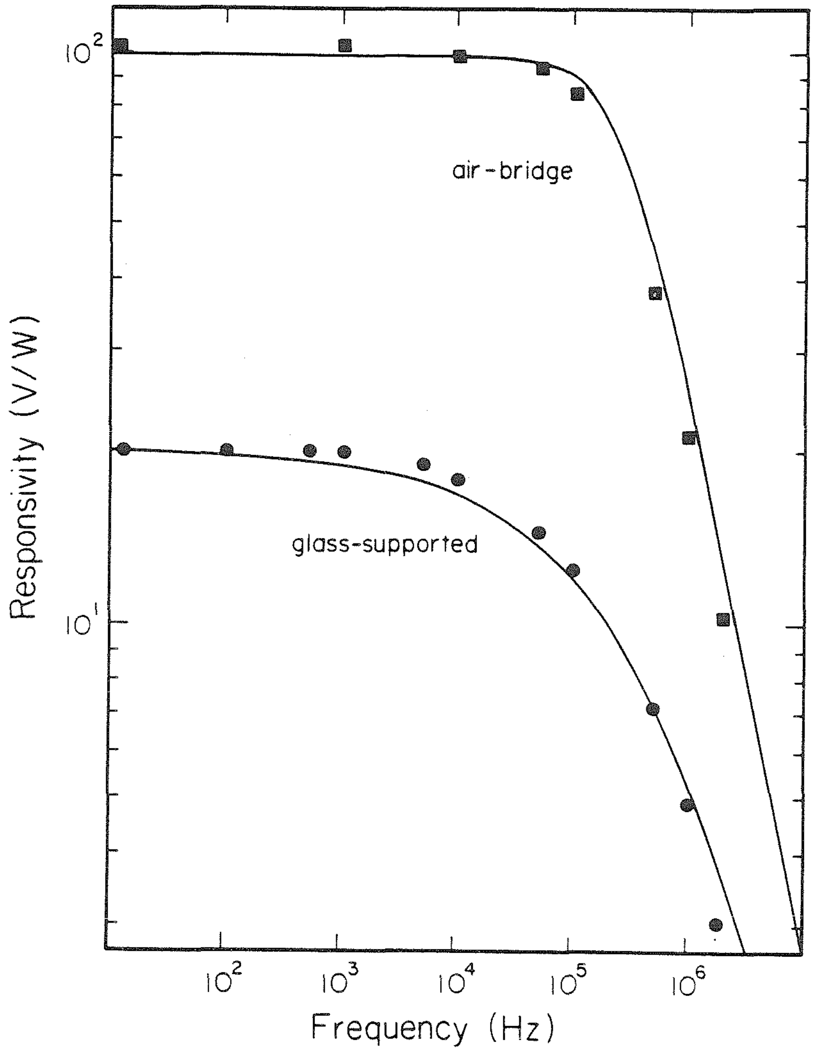

Figure 15: Responsivity of 4μm square air-bridge and glass-supported bismuth bolometers at 0.1V bias. The solid lines are fitted from eqs. 10 and 7.

and treating both G_{dc} and a as adjustable parameters. The dc conductance is found using eq. 18 to be $\alpha V_b/R_{dc}$, and a is chosen to obtain the best fit to the frequency response. For the bolometer in fig. 15 the value of G_{dc} is 1.5×10^{-5} W/K, and a is 1.35µm. The effect of the silver antenna can be seen by using a to calculate G_s at zero frequency from eq. 4 and noting that G_m is the difference between G_{dc} and G_s. Using the values for this bolometer we find the metal conductance is about 75% of that of the substrate, larger than the estimate of Hwang et al [2], who used 30%. It is clear the effect of the antenna metalization cannot be ignored if an accurate model of a substrate-supported microbolometer is desired. Unfortunately, the present model is of limited predictive value, since the relative effects of antenna metalization and substrate conductance depend on the device size and substrate thermal conductivity.

For substrate-supported detectors reductions in substrate thermal conductivity offer a simple way to increase response. One possibility is the use of a plastic to insulate the detector from the substrate. This approach has been used in a 119µm antenna array [17] that was fabricated on a silicon substrate. Since silicon has a large thermal conductivity (about one hundred times larger than fused quartz) bolometers made directly on it have very low responsivity. By using a 0.5µm thick layer of DuPont Pyralin 2555 (a polyimide) between the microbolometer and silicon substrate a detector responsivity of 3V/W at 0.1V bias was obtained. Comparable size devices on fused quartz gave 5V/W. From this we can see the excellent insulating properties of Pyralin, with a thermal conductivity of only $0.15W(m\ K)^{-1}$ [18]. Use of somewhat thicker layers on fused quartz should increase the dc response of substrate-supported bolometers over that given in fig. 15 [19].

The actual performance of the microbolometers as detectors is determined by their noise equivalent power (NEP). This is just the minimum input power which will yield a signal-to-noise ratio of 1:1 for a 1Hz output bandwidth. The NEP is found using

$$NEP = V_n/\mathcal{R} \qquad (20)$$

where V_n is the noise voltage divided by the square root of the detection bandwidth, and $\mathcal{R}$ is the responsivity. The noise voltage for these devices was measured with a PAR 124A lockin and 117 plug-in; fig. 5 shows the noise curves at 0.1V bias, corrected for amplifier noise. The noise equivalent power (at 0.1V bias) for the air-bridge and substrate-supported bolometers is given in fig. 16. The NEP below 50kHz is limited by 1/f noise and above 100kHz by the roll-off in the bolometer responsivity. Because of the reduced thermal conductance the air-bridge bolometer's NEP is over four times lower than the substrate-supported device.

Thermal detectors such as these have a fundamentally limited NEP, set by statistical fluctuations in the power

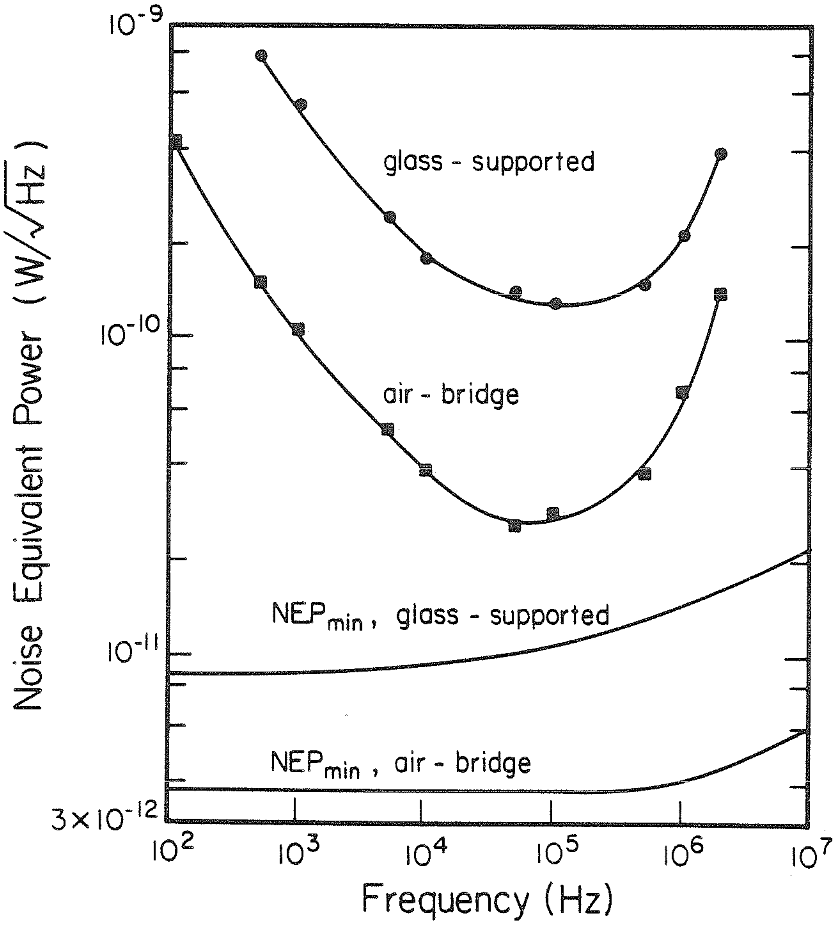

Figure 16: Electrical noise equivalent power for the detectors used in fig. 15. The curves labeled NEP_{min} are from eq. 22 using the fitted thermal data from fig. 15.

flow between the bolometer and its environment. The mean square value ΔW^2 of this fluctuation is given by

$$\Delta W^2 = 4k_B T^2 G \Delta f \tag{21}$$

where G is the thermal conductance out of the bolometer and Δf is the detection bandwidth [20]. In terms of the complex thermal impedance Z_t this gives the minimum noise equivalent power as

$$NEP_{min} = [\ 4k_B T^2 \mathrm{Re}(1/Z_t)\ ]^{1/2} \quad . \tag{22}$$

For the two thermal models discussed earlier Z_t is independent of frequency for low frequencies, so NEP_{min} is independent of frequency. At high frequencies $\mathrm{Re}(1/Z_t)$ varies like $f^{1/2}$, so the minimum NEP increases like $f^{1/4}$. Note that the detector responsivity decreases like f^{-1}, so its actual NEP will increase as f, faster than the fluctuation limit. Figure 16 also shows the fluctuation-limited NEP for the air-bridge and substrate-supported bolometers, based on the thermal impedances used to fit the data in fig. 15. At 100kHz the air-bridge is about a factor of seven from its fundamental limit, and the substrate-supported device a factor of 13 from its limit.

Bi-Sb Microthermocouples

One detector that avoids the low frequency noise problems of the bismuth microbolometer is the bismuth-antimony microthermocouple. Since this device does not require biasing the only source of noise is Johnson noise.

The device is fabricated using the same photoresist bridge techniques used for bolometers, but actually is quite different. Recall that a microbolometer effectively measures the average temperature of the entire device; the microthermocouple measures the peak temperature instead. Figure 17 illustrates this difference. We again assume the silver antenna acts as a perfect heat sink, so the two ends of the device are at the same temperature, T_o. The center of the detector where the Bi-Sb contact is located is at a temperature $T_o + \phi$. Because of the difference in thermal-emf for the two materials there will be an open circuit voltage across the junction

$$V = (\alpha_{Sb} - \alpha_{Bi})\phi \tag{23}$$

where α_{Sb} is the thermal-emf of antimony and α_{Bi} the thermal-emf of bismuth. The output signal then depends on the temperature difference between the center of the device and the ends.

As has been noted previously, both the electrical and thermal properties of thin-film bismuth are different from those of the bulk. It has also been reported by Johnson and Harris [21] that the thermal-emf of bismuth films thinner than 1μm decreases rapidly with decreasing thickness, to approximately -30μV/°C at 0.1μm (compared to a bulk value of -73μV/°C). Abrosimov et al [8] reported a somewhat larger value of -55μV/°C at the same thickness. In order to check the value of α for our films large thin-film Bi-Sb junctions were made by evaporating bismuth on one half of a glass

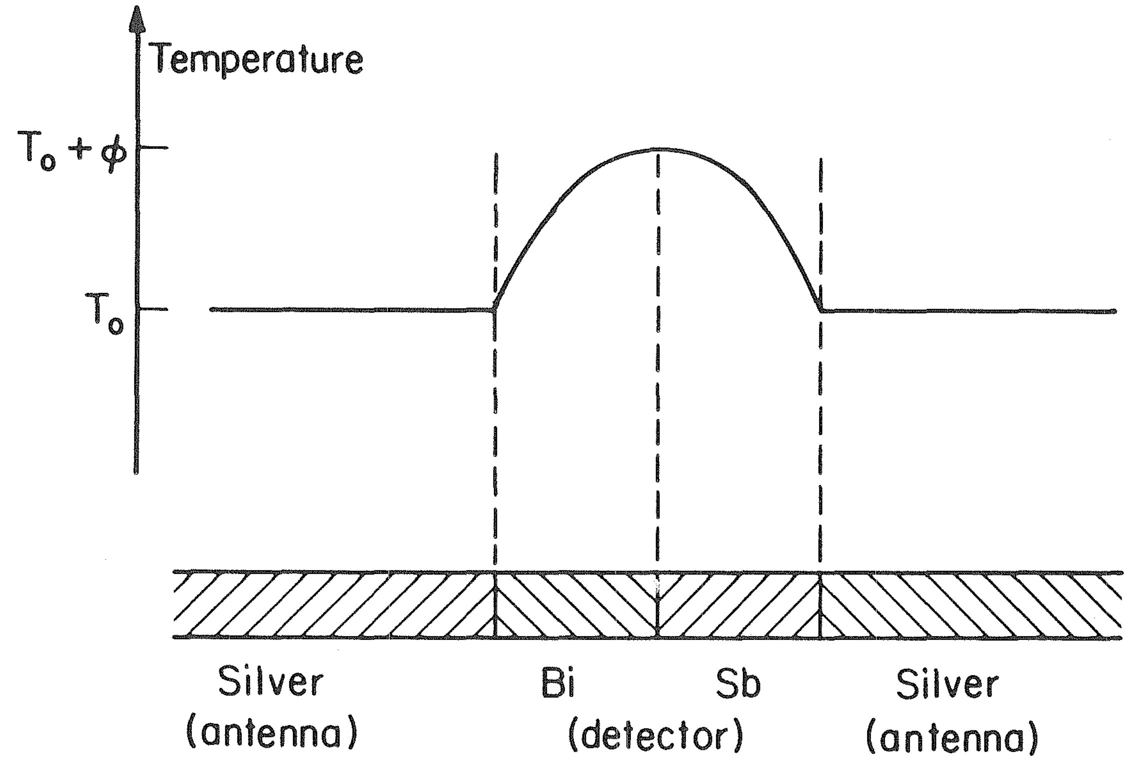

Figure 17: Temperature profile in a microthermocouple detector. The response is proportional to the peak temperature ϕ.

substrate, followed by an antimony evaporation on the other half of the substrate. The substrate was then clamped to an arrangement of copper tubing so that the junction could be heated while the ends of the substrate were cooled (fig. 18). The voltage V across the ends was recorded, and the temperatures of the bismuth cold-end, T_1, Bi-Sb hot junction, T_2, and the antimony cold-end, T_3, measured with a contact thermocouple. The thermal-emf of the bismuth is then given by

$$\alpha_{Bi} = \frac{V - \alpha_{Sb}(T_2 - T_3)}{T_1 - T_2} \quad . \tag{24}$$

Assuming the thermal-emf of antimony is the same as the bulk (Johnson and Harris reported no change in junction thermopower when the thickness of the antimony was varied) the mean value of α_{Bi} for five measurements on 120nm thick films was -73μV/°C (with a standard deviation of 9μV/°C). This value is the same as the bulk, and would give a Bi-Sb thermoelectric power of about 120μV/°C, consistent with the value reported by Lahiji and Wise [22] for similar junctions.

Figure 19 shows the responsivity of the microthermocouple shown in fig. 8, measured with the 150MHz rf network in fig. 14. Also shown is the responsivity of a bolometer the same size as the thermocouple. Figure 20 shows the NEP of these detectors. The devices here were made with a different mask pattern than those in fig. 15, and were about 4μm long, 8μm wide, and 100nm thick. Because of this these detectors have a larger thermal conductance than the

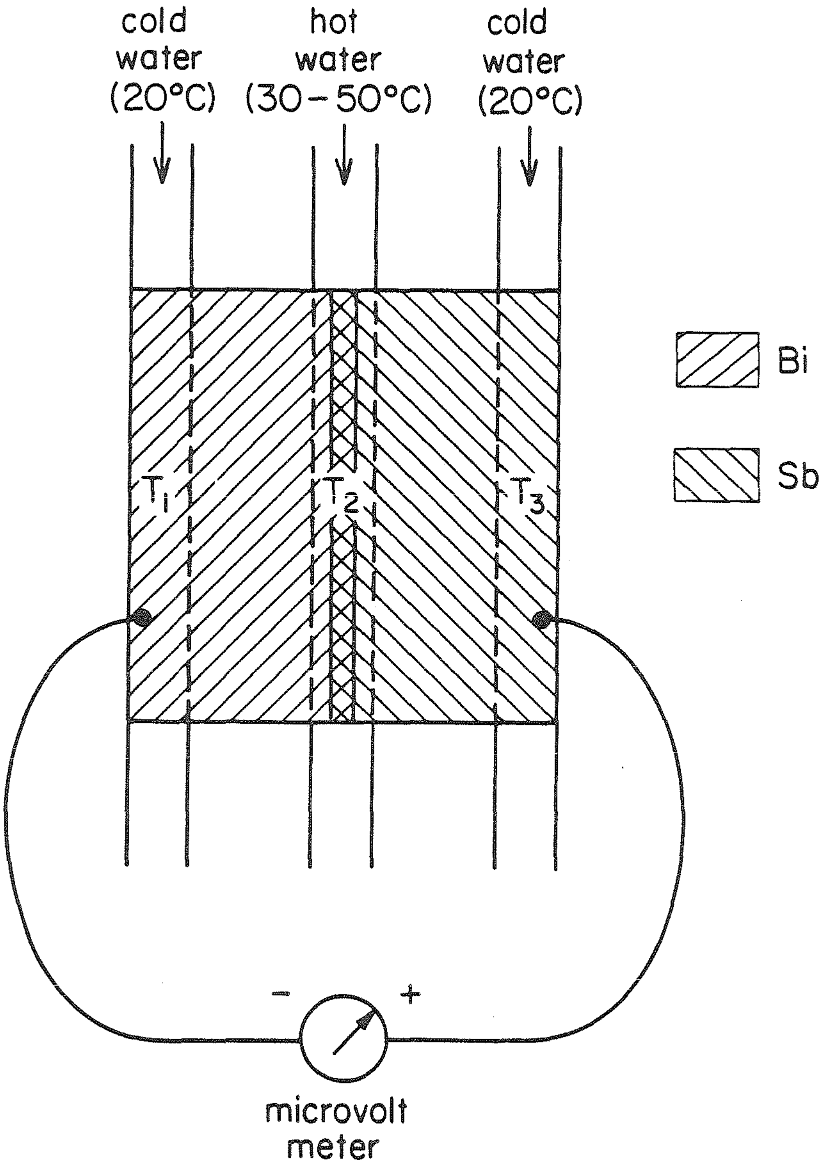

Figure 18: System used to measure the thermopowers of thin film bismuth. Measurements were made for a variety of water temperatures and film thicknesses.

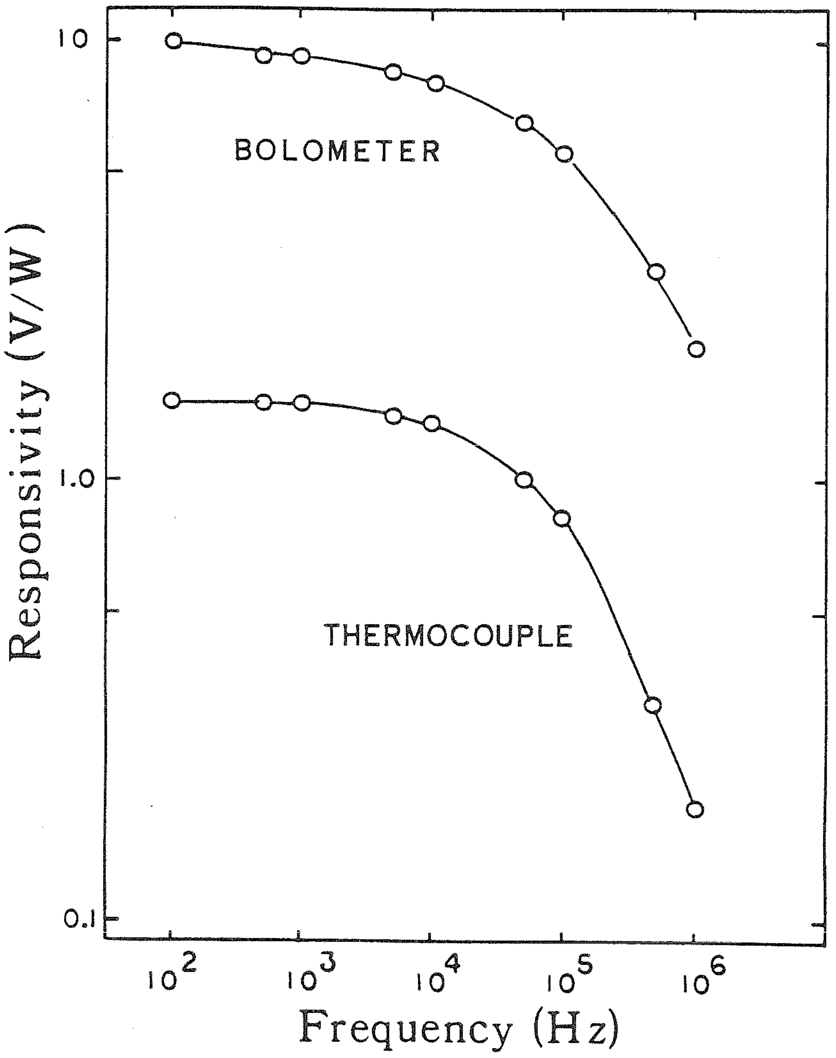

Figure 19: Responsivity of a bismuth-antimony microthermocouple (no bias) and a bismuth bolometer the same size (0.23V bias).

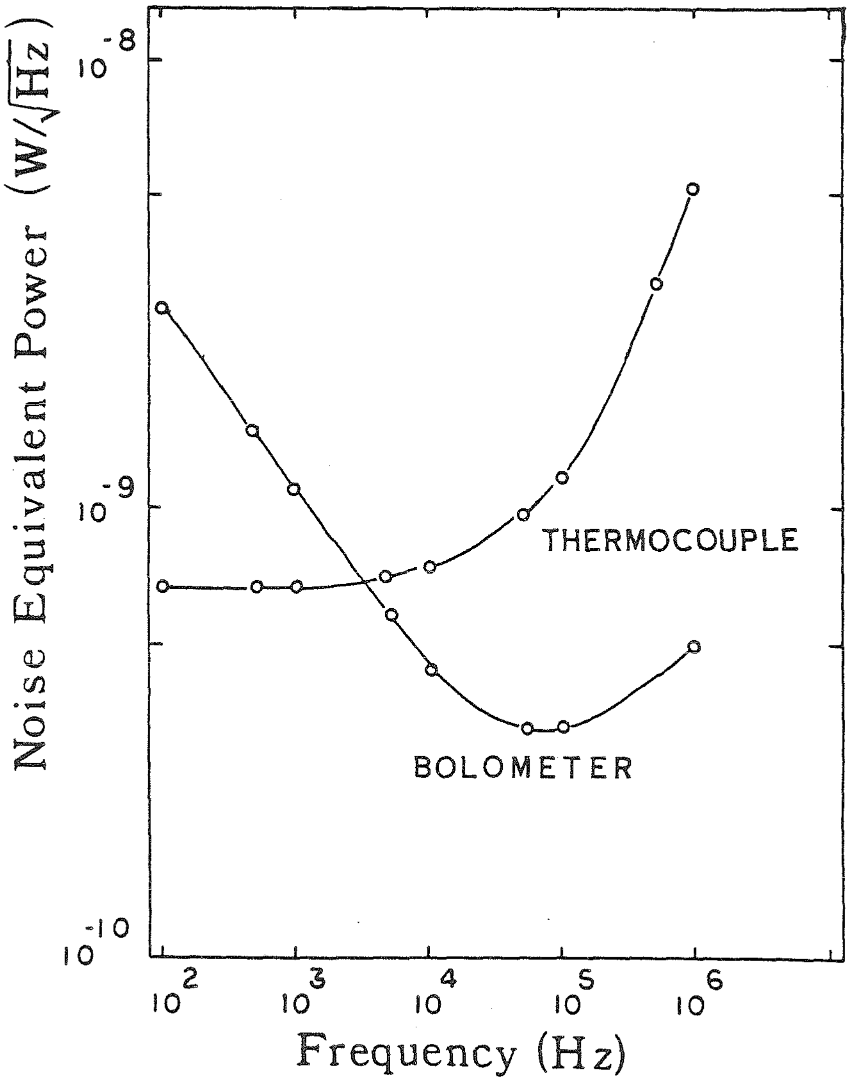

Figure 20: Noise equivalent power for the detectors in fig. 19.

substrate-supported bolometer discussed earlier. For this bolometer the dc responsivity was 10V/W at a bias of 0.23V; using eq. 18 this gives a dc conductance of 7×10^{-5} W/K, a factor of about 4.5 larger than before. Assuming the peak temperature at the Bi-Sb junction scales in the same way as the dc conductance, the responsivity of a thermocouple made with the smaller device dimensions should increase from 1.4V/W here to about 7V/W. This would give a low frequency noise equivalent power of 1.5×10^{-10} W(Hz)$^{-1/2}$, instead of the value 6.7×10^{-10} W(Hz)$^{-1/2}$ in fig. 20.

At present no thermocouples have been made using the air-bridge fabrication techniques. Unlike the substrate-supported devices, however, the thermal model for the air-bridge does give the peak temperature in the device, so we can estimate the performance of such a detector. From the solution to eq. 8 the ratio Z_p of the time-varying temperature at the center of the bridge to the power dissipated in the device is

$$Z_p = \frac{L_b^2}{tw\ell K_b}\left(1 - \operatorname{sech}\frac{\ell}{2L_b}\right) \qquad (25)$$

where L_b is again the thermal diffusion length, $L_b = (K_b/i\omega\rho_b C_b)^{1/2}$. The low frequency limit is $\ell/8twK_b$, a factor of 1.5 larger than the low frequency average thermal impedance Z_t (eq. 10). The high frequency limit is the same as before, $1/i\omega\ell tw\rho_b C_b$. Thus the peak temperature in the device is described by a thermal equivalent circuit consisting of a resistance $\ell/8twK_b$ in parallel with a capacitance $\ell tw\rho_b C_b$.

We can now estimate the performance of an air-bridge microthermocouple. The dc thermal resistance of the device in fig. 15 is 3.3×10^5 K/W, so the peak temperature rise per watt is 5×10^5 K/W, 1.5 times larger. The responsivity of the thermocouple is found from eq. 23,

$$\mathbb{R} = (\alpha_{Sb} - \alpha_{Bi})|\mathbb{Z}_p| \quad . \tag{26}$$

Using a thermoelectric power $(\alpha_{Sb} - \alpha_{Bi})$ of 100μV/°C and the peak temperature above we find a responsivity of about 50V/W. Since the noise of a thermocouple is only Johnson noise, for a 150Ω device the noise voltage in eq. 20 is $1.6\text{nV(Hz)}^{-1/2}$. This gives a NEP of about 3×10^{-11} $\text{W(Hz)}^{-1/2}$, quite close to that measured for the air-bridge bolometer (fig. 16) at 100kHz. With a microthermocouple, however, this performance can be maintained at low frequency, where 1/f-noise in the bolometers seriously degrade their performance. This estimate does assume the thermal conductivity of thin-film antimony will be similar to the bismuth's, but is probably within a factor of two of what can actually be made.

Antenna Impedance Measurements

One unusual application of the bismuth microbolometer is the measurement of the impedance of the antenna used to couple power into the bolometer. This is possible because the impedance of the bolometer can be easily determined: it is just a pure resistance, whose value can be measured at zero frequency. In addition, the resistance can be increased in fairly small steps (a few ohms, over a range of 50Ω -200Ω) by applying a large dc bias current to the device. By measuring the power coupled into the bolometer from the antenna as the resistance is varied the impedance of the antenna can be inferred.

The particular configuration studied here consisted of a bow-tie antenna array and the quasi-optical system described in chapter 2. The array spacing was designed to be $\lambda_d/2$ at 100GHz The actual source used was a 94GHz Gunn diode, which provided the long term power stability necessary for the measurements.

The large dc bias used to increase device resistance does so by actually removing part of the bismuth that makes up the detector. Figure 21a shows a microbolometer before the device has been 'burned out.' At this point the detector had a resistance of 50Ω. By application of about 1mW dc bias power for five to ten seconds the device resistance increased approximately 5Ω. This process was repeated until the resistance had increased to 200Ω; fig. 21b shows almost all the bismuth that made up the detector is no longer present.

Since the responsivity of a microbolometer is a function of its size it would be expected that the detector response would increase as it is burned out. The antenna impedance measurement requires the relative change in power coupled into the device as a function of resistance, so we must carefully normalize out the change in detector response. This can be done using a circuit analogous to the rf circuit

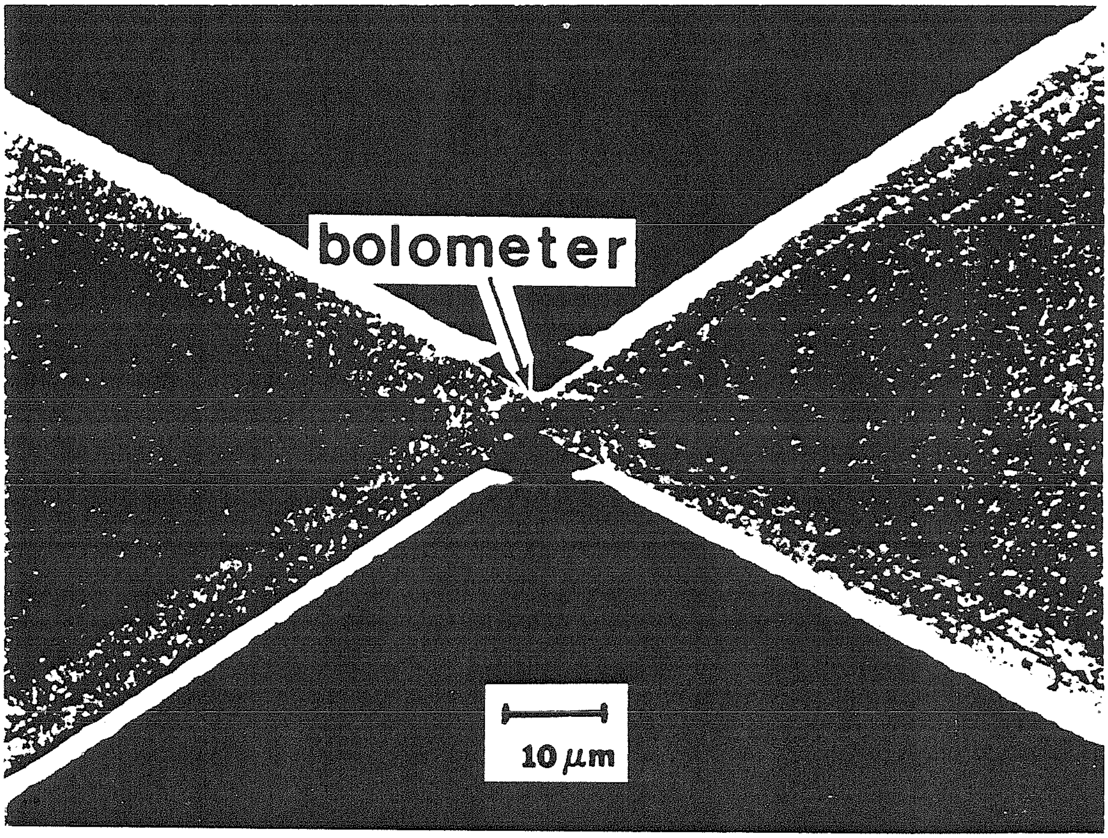

Figure 21a: Photomicrograph of bow tie and bismuth bolometer used for impedance measurement. The device had a resistance of 50Ω at this point.

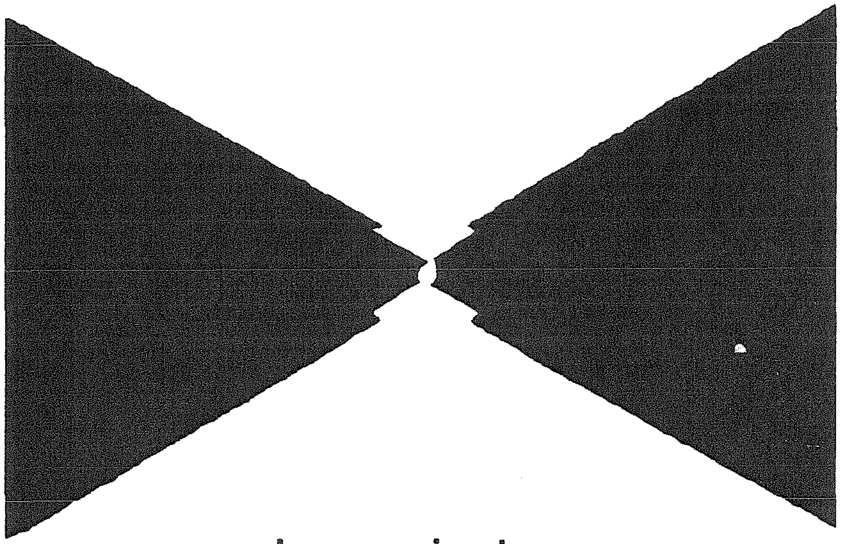

transmission

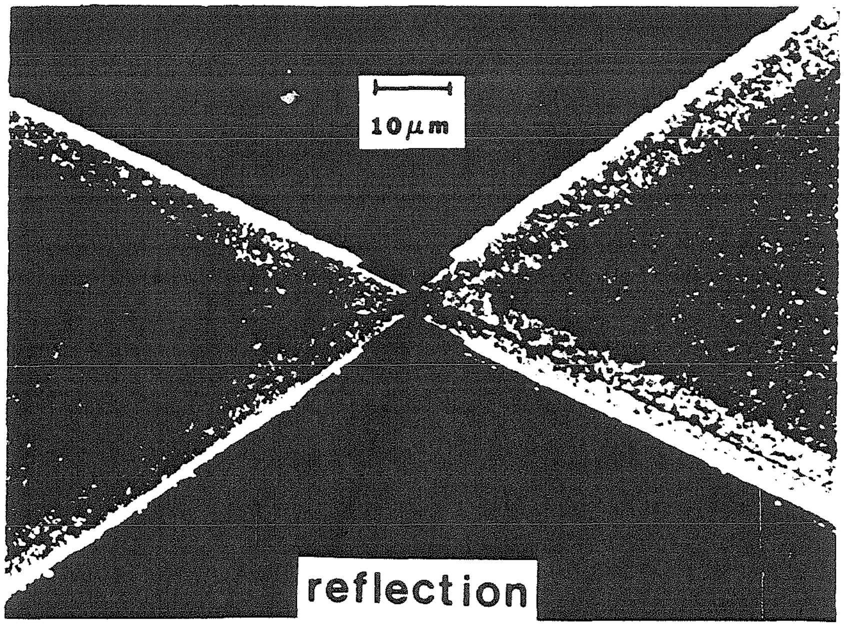

reflection

Figure 21b: Photomicrograph of bolometer after it has been over-biased to increase its resistance to 200Ω.

shown in fig. 14. In this application the optical system containing the detector cannot be disturbed since the optical coupling to the antenna must not be changed. Because of this the carrier frequency of the test circuit has to be low enough to pass through the ribbon cable and chip-package used. The circuit shown in fig. 22 is now used, operating at a carrier frequency of about 1kHz, amplitude modulated at 11Hz. The carrier frequency input voltage is measured, which gives the input power P_{rf}. The low frequency output voltage V_{am} is also measured; the low frequency response is then $R_{lf} = V_{am}/P_{rf}$. This is repeated at each detector resistance and used to correct the 94GHz measurement for the change in detector response. Figure 23 shows the relative increase in response as the device resistance increases.

Some care is required in interpreting the absolute magnitude of the responsivity measured with this circuit. Recall that the 150MHz measurements depended on the fact that the detector was too slow to actually follow the 150MHz frequency. At the low frequency used here this is no longer true. As we have seen (fig. 15) the bolometer can follow the 1kHz signal. The responsivity is now given by

$$R_{lf} = - \frac{\left(\frac{d^2I}{dV^2}\right)}{2\left(\frac{dI}{dV}\right)^2} \quad . \tag{27}$$

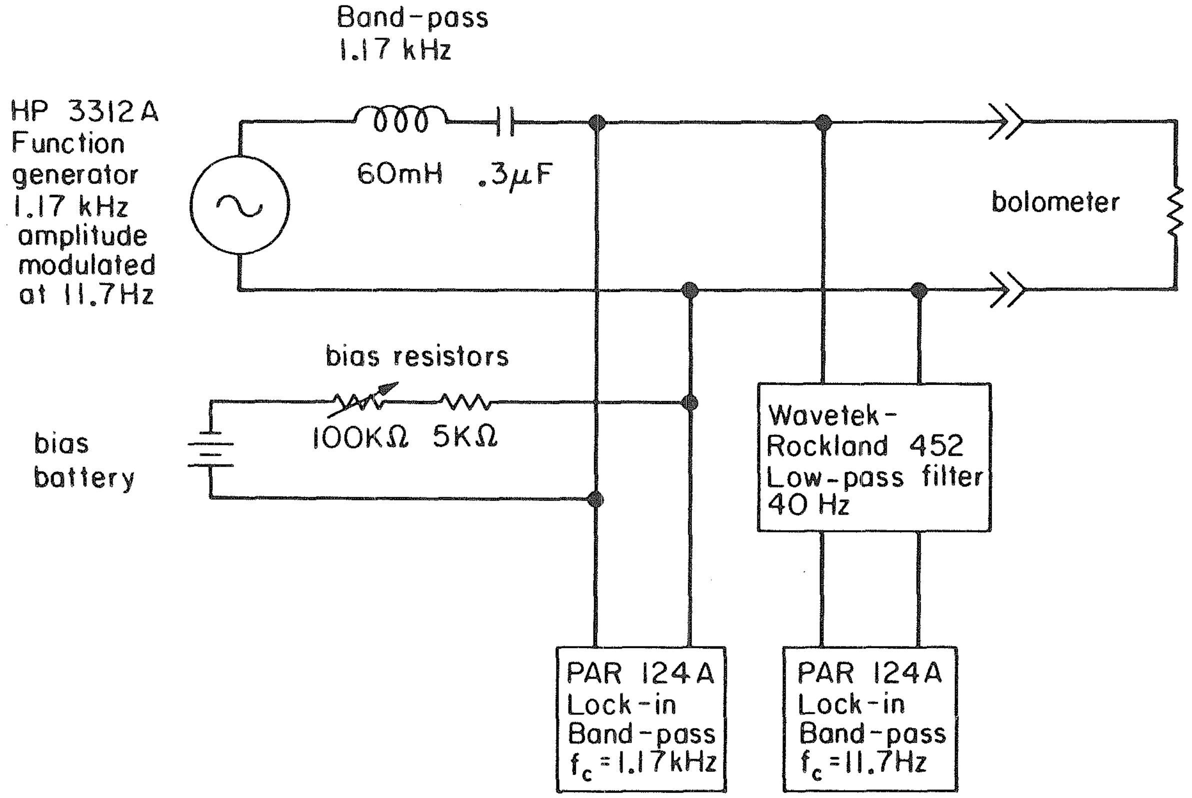

Figure 22: Low frequency circuit used to measure relative responsivity changes as the bolometer resistance is increased.

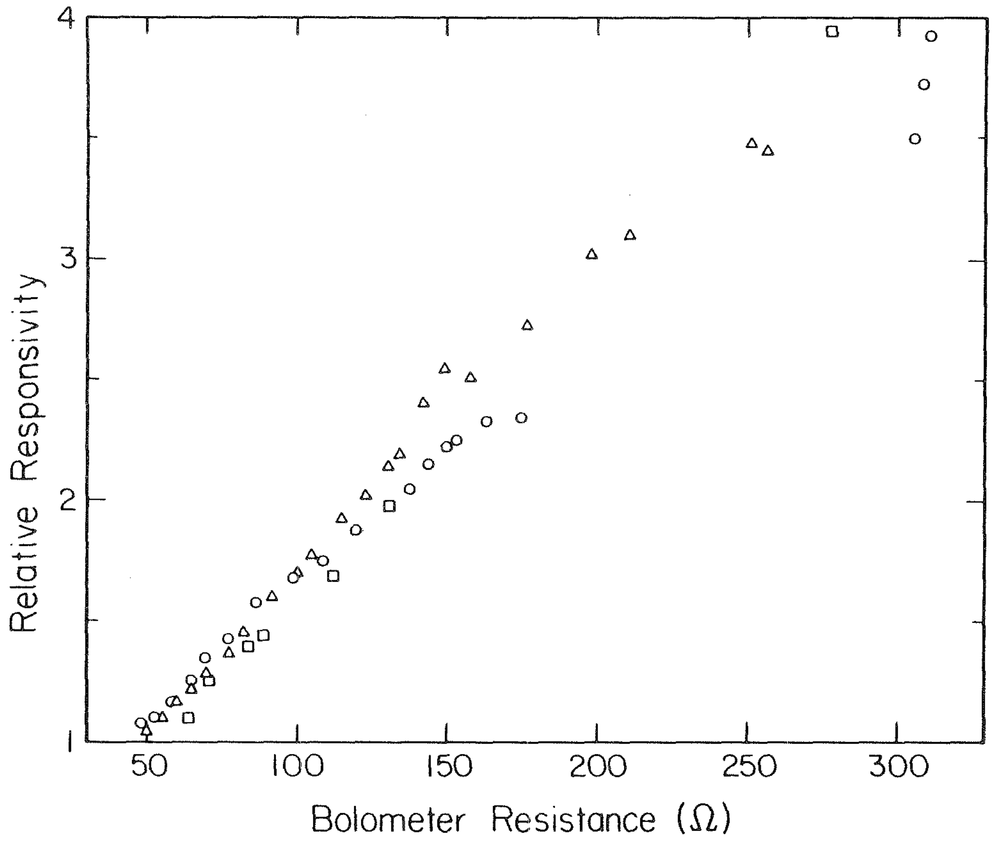

Figure 23: Relative change in detector responsivity as its resistance is increased by over-biasing.

The relation between I and V at low frequency is given by eq. 17, so

$$R_{lf} = -\beta I(\beta I^2 + 3)/[(\beta I^2)^2 - 1] \tag{28}$$

where I is the operating point bias current. For small βI^2 (a typical substrate-supported bolometer has a β of about 10^4 $(\text{amp})^{-2}$, and an operating current of 10^{-3} amp) eq. 28 reduces to $3\beta I$, three times larger than the classical bolometer response βI. Since the low carrier-frequency responsivity is used only for relative corrections this factor does not really affect the 94GHz measurements.

Once the relative response of the detector is known the power coupled from the antenna versus the bolometer resistance can be determined. Figure 24 shows the results for three different antennas in the bow-tie array. This can be interpreted as a plot of the power transmission coefficient $|\tau|^2$,

$$|\tau|^2 = 1 - \left| \frac{Z_{ant} - R_{bol}}{Z_{ant} + R_{bol}} \right|^2 \tag{29}$$

where Z_{ant} is the antenna impedance and R_{bol} is the bolometer resistance. These antennas have a bow angle of 60°, and should have a real impedance of 150Ω [23]; fig. 24 also shows lines found using eq. 29 assuming antenna impedances of 150Ω and 185Ω. The measurements at 94GHz are consistent with the predicted value of 150Ω.

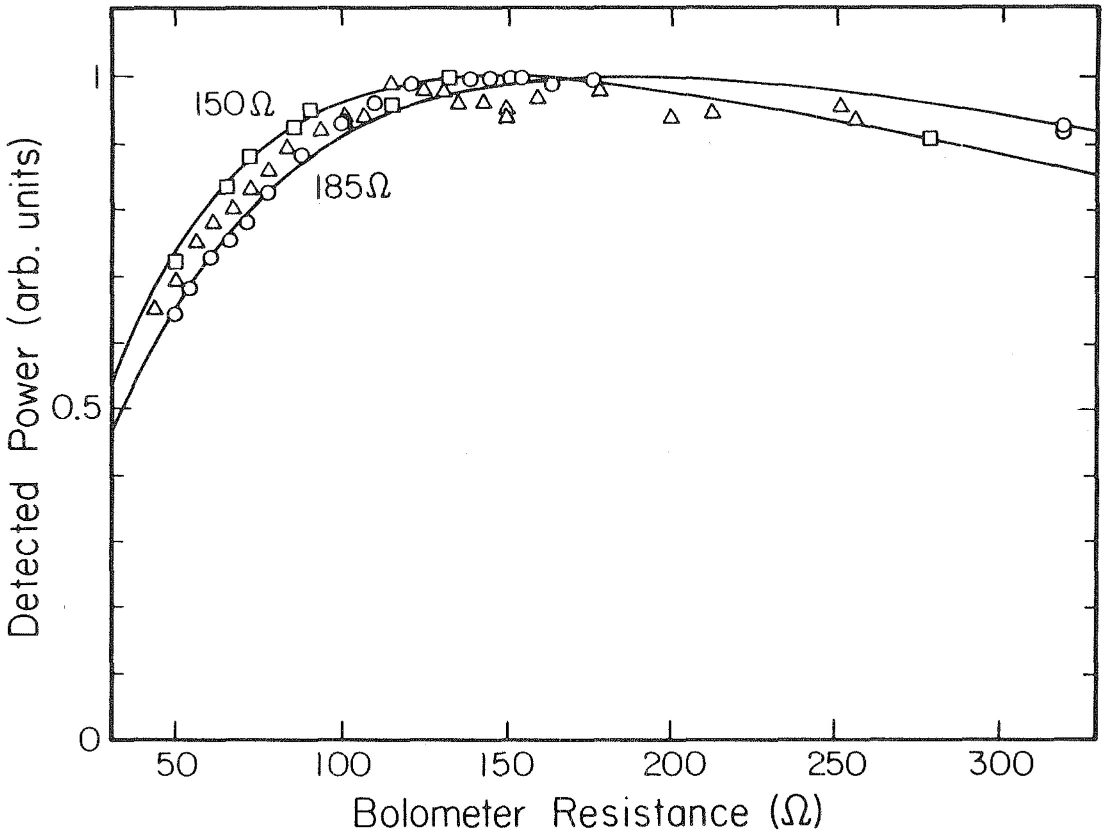

Figure 24: Normalized detected power coupled from the antenna into the bolometer as a function of bolometer resistance. The solid lines are from eq. 29 assuming the antenna impedance is 150Ω or 185Ω.

References

[1] Neikirk, D.P., and D.B. Rutledge, 'Air-bridge microbolometer for far-infrared detection,' submitted for publication, Appl. Phys. Lett.

[2] Hwang, T.-L., S.E. Schwarz, and D.B. Rutledge, 'Microbolometers for infrared detection,' Appl. Phys. Lett. **34**, 773 (1979).

[3] Neikirk, D.P., and D.B. Rutledge, 'Self-heated thermocouples for far-infrared detection,' Appl. Phys. Lett. **41**, 400 (1982).

[4] Ashcroft, N.W., and N.D. Mermin, **Solid State Physics** (Holt, Rinehart, and Winston, New York, 1976) p. 255.

[5] Smith, R.A., F.E. Jones, and R.P. Chasmar, **The Detection and Measurement of Infrared Radiation** (Oxford University Press, London, 1968), p. 85.

[6] Colombani, A., and P. Huet, 'Electromagnetic properties of thin films of bismuth,' International Conference on Structure and Properties of Thin Films, Bolton Landing, N.Y., 1959, (C.A. Neugebauer, J.B. Newkirk, and D.A. Vermilyea, eds., Wiley, New York, 1959).

[7] Komnik, Yu. F., E. Bukhshtab, Yu. Nikitin, and V. Andrievskii, 'Features of temperature dependence of the resistance of thin bismuth films,' Zh. Eksp. Teor. Fiz. **60**, 669 (1971).

[8] Abrosimov, V., B. Egorov, and M. Krykin, 'Size effect of kinetic coefficients in polycrystalline bismuth films,' Zh. Eksp. Teor. Fiz. **64**, 217 (1973).

[9] Kawazu, A., Y. Saito, H. Asahi, and G. Tominaga, 'Structure and electrical properties of thin bismuth films,' Thin Solid Films **37**, 261 (1976).

[10] Joglekar, A., R. Karekar, and K. Sathianandan, 'Electrical resistivity of polycrystalline bismuth films,' J. Vac. Sci. Technol. **11**, 528 (1974).

[11] Dolan, G., 'Offset masks for lift-off photoprocessing,' Appl. Phys. Let. **31**, 337 (1977).

[12] Dunkleberger, L., 'Stencil technique for the preparation of thin-film Josephson devices,' J. Vac. Sci. Technol. **15**, 88 (1978).

[13] Tong, P.P., D.P. Neikirk, P.E. Young, W.A. Peebles, N.C. Luhmann, and D.B. Rutledge, 'Imaging polarimeter arrays for near-millimeter waves,' to be published.

[14] Dolan, G.J., T.G. Phillips, and D.P. Woody, 'Low-noise 115-GHz mixing in superconducting oxide-barrier tunnel junctions,' Appl. Phys. Lett. **34**, 347 (1979).

[15] Danchi, W.C., F. Habbal, and M. Tinkham, 'ac Josephson effect in small area superconducting tunnel junctions at 604GHz,' Appl. Phys. Lett. **41**, 883 (1982).

[16] Dobkin, D.M., and B.D. Cantos, 'Plasma formation of buffer layers for multilayer resist structures,' IEEE Electron Devices Lett. **EDL-2**, 222 (1981).

[17] Neikirk, D.P., P.P. Tong, D.B. Rutledge, H. Park, and P.E. Young, 'Imaging antenna array at 119μm,' Appl. Phys. Lett. **41**, 329 (1982).

[18] Du Pont Co., Technical Bulletin PC-1, 'Pyralin:

polyimide coatings for electronics.'

[19] Neikirk, D.P., W.W. Lam, and D.B. Rutledge, 'Far-infrared microbolometer detectors,'submitted for publication, Int. J. Infrared and Millimeter Waves.

[20] Smith et al, pp. 211-213.

[21] Johnson, E.A., and L. Harris, 'Thermoelectric force of thin films,' Phys. Rev. **44**, 944 (1933).

[22] Lahiji, G.R., and K.D. Wise, 'A batch-fabricated silicon thermopile infrared detector,' IEEE Trans. Electron Devices **ED-29**, 14 (1982).

[23] Rutledge, D.B., and M.S. Muha, 'Imaging antenna arrays,' IEEE Trans. Antennas and Propagat. **AP-30**, 535 (1982).

Chapter 4

Lift-Off Patterning of Thin Films

One necessary step in the fabrication of any integrated circuit is the patterning of deposited thin films. In the simplest case this is just the delineation of metal interconnects, but may also include patterning of a variety of dielectric materials. Conventionally these patterns are formed through the use of photolithography followed by a chemical etch of the deposited film. When desired feature sizes are smaller than about 5μm, however, it becomes difficult to control many of these etches. Undercutting along edges (and sometimes nonisotropic etch rates due to nonuniformities in the material being etched) may seriously affect pattern geometry. These problems have been the driving force behind the extensive efforts to develop 'dry' plasma processing [1] which exhibits a highly directional etch: straight down through the thin film without lateral undercutting of the mask.

There is, however, a technique which avoids the use of any etch step. Here the photolithographic masking is done before the material to be patterned is deposited. The film is then deposited onto the substrate only through the openings in the mask. When the mask is removed (usually with a simple solvent) the unwanted material is carried off with it. Because of this aspect the technique is usually referred to as lift-off processing. In principle the only limit to feature size is set by the resolution of the photolithography. With a good master mask and standard contact printing 2µm features can easily be obtained at this step. The deposition process for the film must also be nondestructive for the photoresist mask (this usually requires that the substrate temperature during deposition be no more than 125°C).

Actually producing 2µm features in the final deposited film, is, however, considerably more difficult than producing them in the mask. The most serious difficulty in lift-off patterning is the generation of an appropriate photoresist edge profile. Figure 1 illustrates this problem. Because of diffraction and imperfect mask-to-resist contact, the profile shown in fig. 1a is almost always produced in standard lithography. When used as a lift-off mask the deposited material will cover the step, either preventing lift-off entirely, or leaving lift-off 'flags' along the edge (fig. 2b) [2]. To achieve good lift-off a photoresist profile similar to that shown in fig. 1b is necessary; such a profile ensures that the deposited film is broken cleanly along the edges.

Chlorobenzene Lift-Off Process

There are several different techniques available to produce photoresist profiles similar to fig. 1b. The most widely used of these involves a surface modification of the photoresist. By soaking positive photoresist such as Shipley 1350J in chlorobenzene it has been found [3] that the

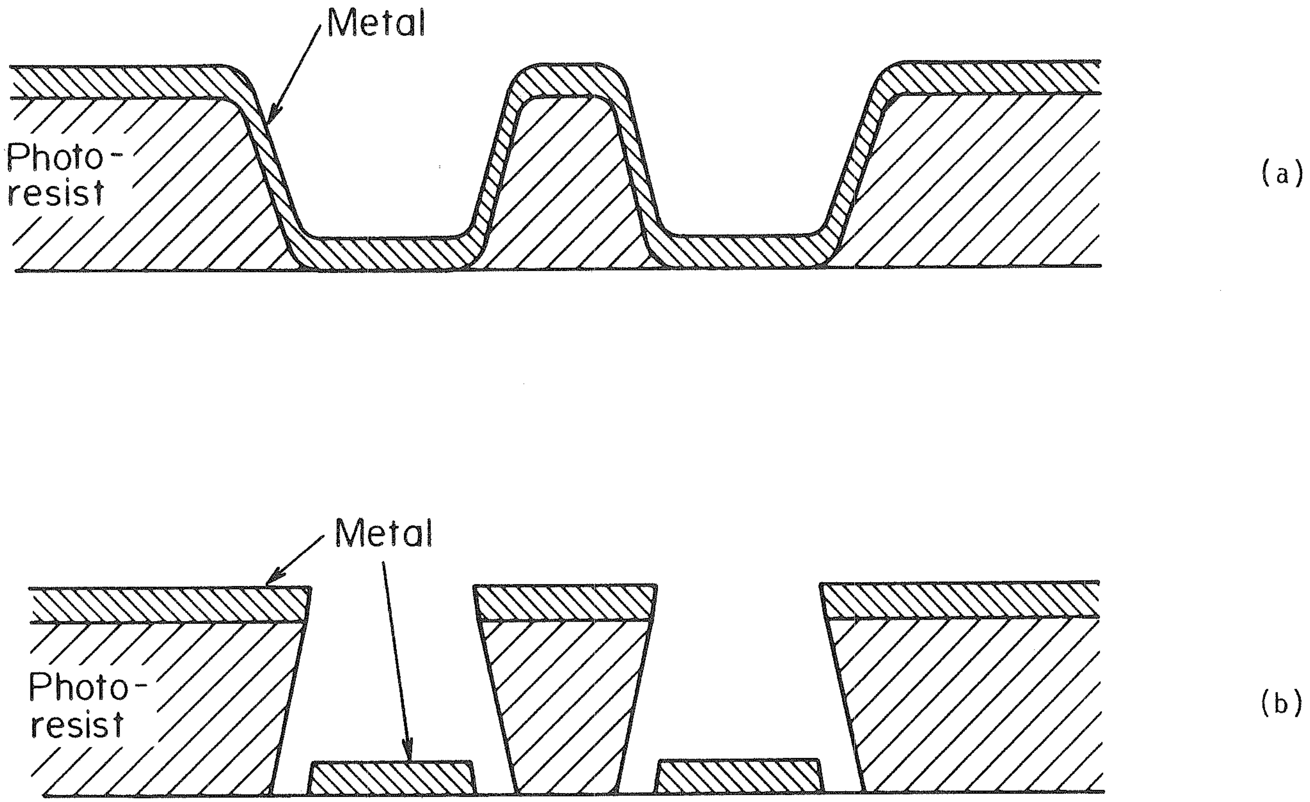

Figure 1: Cross-sectional view of photoresist used for lift-off processing. (a) Typical resist profile; (b) reverse taper necessary for good lift-off.

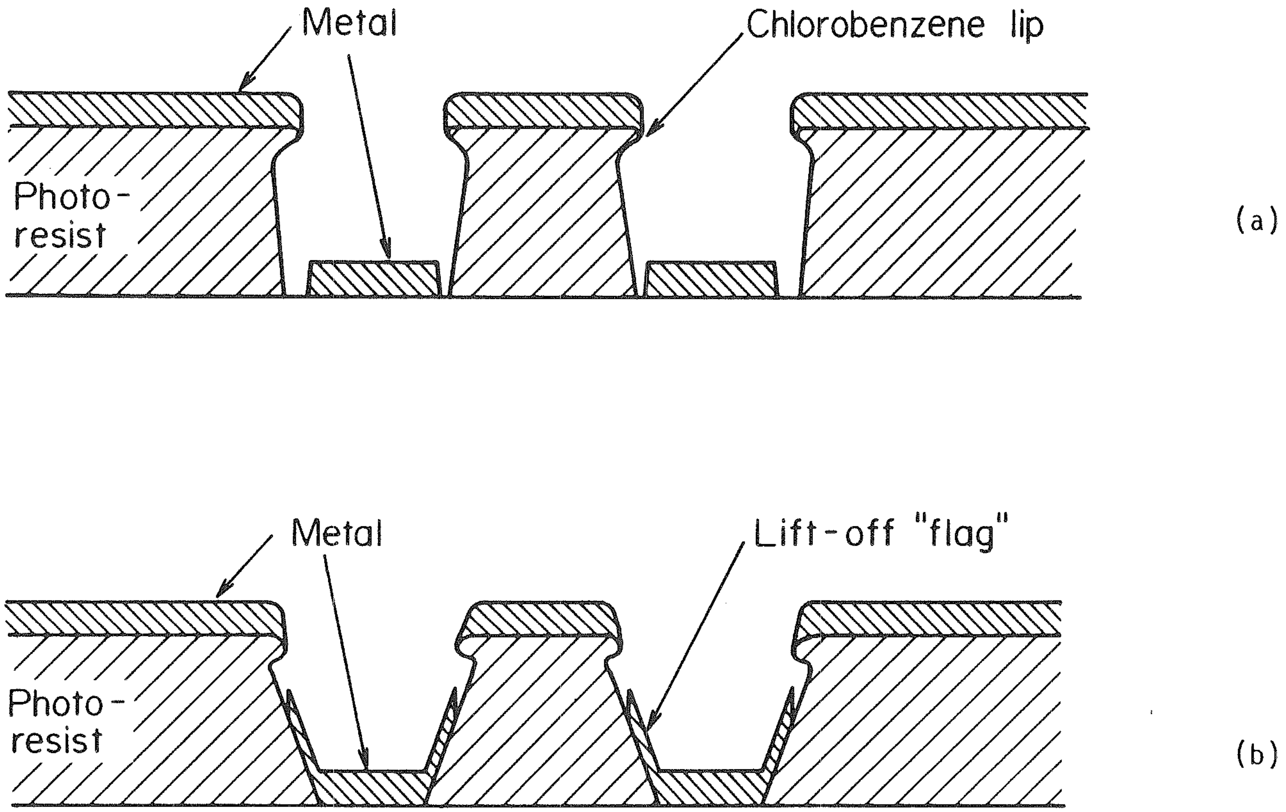

Figure 2: Chlorobenzene treated resist profiles. (a) Lip extends beyond base of resist for good lift-off; (b) formation of lift-off flags.

resist edge shown in fig. 2 can be produced. As long as the lip extends beyond the base of the resist a sharp, clean lift-off will be obtained. Figure 3 shows an SEM of a chlorobenzene-formed lip, and fig. 4 shows the formation of a lift-off flag. The mechanism of this process [4] is fairly complex, but is mainly dependent on the decreased development rate of resist penetrated by chlorobenzene. By adjusting soak time so that the chlorobenzene only diffuses into the surface of the resist the lower portion remains unmodified, and the profile in fig. 2 results. As it affects the photolithographic process, a summary of important steps is provided:

i) Spin: no effect

ii) Prebake: The penetration of the chlorobenzene is strongly influenced by this step. Decreased time or temperature increases penetration, often preventing development; increased time or temperature decreases penetration, reducing the size of the lip.

iii) Exposure: The exposure should produce a resist edge as nearly vertical as possible since chlorobenzene cannot correct gross defects. Typically an exposure producing good profiles in unsoaked resist is best, although a small increase may be necessary.

iv) Chlorobenzene soak: Normally this follows the exposure, although it may precede it. The time should be adjusted to produce a subsequent increase in development of about 1.5 minutes.

v) Dry: Failure to remove the diffused chlorobenzene may prevent development; the resist should either be rinsed in freon or baked dry for a few minutes.

vi) Development: Because of the method of action the development time will be considerably increased; observation should reveal no visible development for the first 1-2 minutes, followed by rapid development for 30-40 sec. Overdevelopment can eventually etch away the lip, and should be avoided.

The basic processing steps using our equipment has been found to be:

i) Prebake: 85°C, 25 min.

ii) Exposure: 15-20 sec at about 300 on exposure meter.

iii) Chlorobenzene soak: 10 min.

iv) Dry: 85°C, 5 min.

v) Develop: Microposit developer, diluted 1:1 with water, about 2-3 minutes, as noted above.

The successful formation of a chlorobenzene lip can be judged with an optical microscope. At a magnification of 500 to 1000 times the edges of the photoresist appear as two distinct lines, one due to the bulk resist and one due to the lip (this often appears as a bright line along the edge). Consistent appearance of this bright edge usually assures good lift-off quality even for relatively thick deposited films.

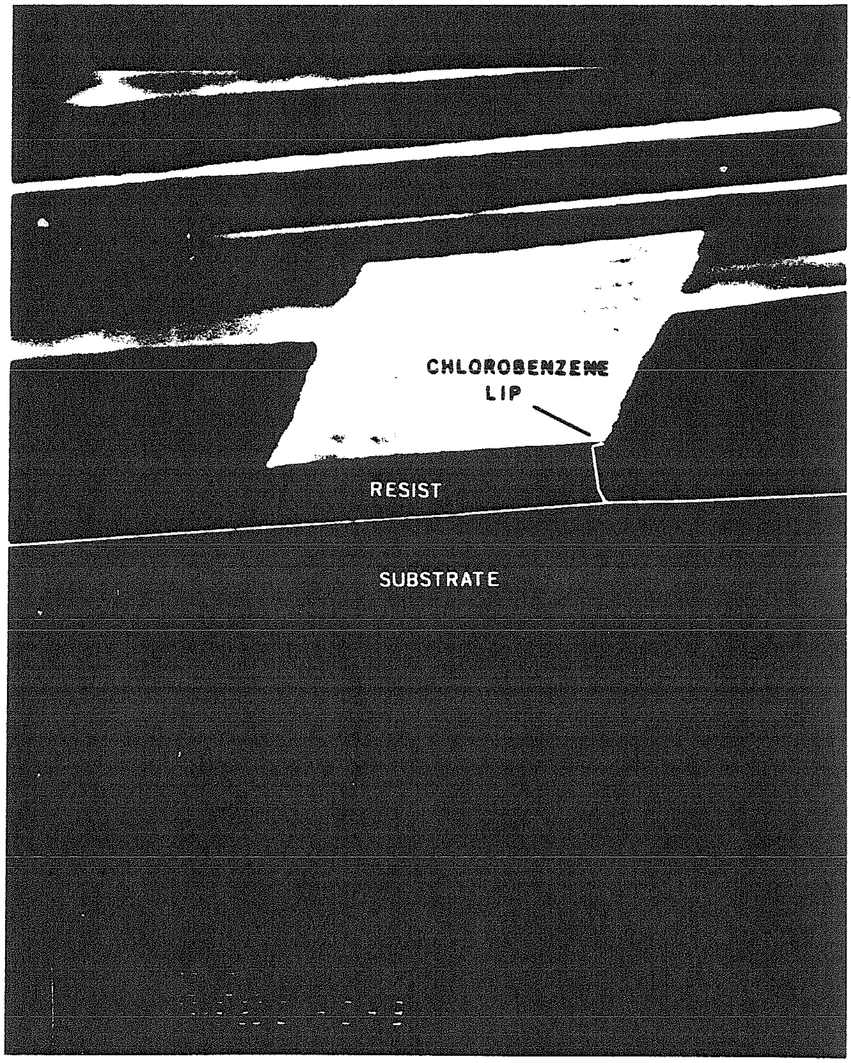

Figure 3: Cross-section of a photoresist pattern treated with chlorobenzene.

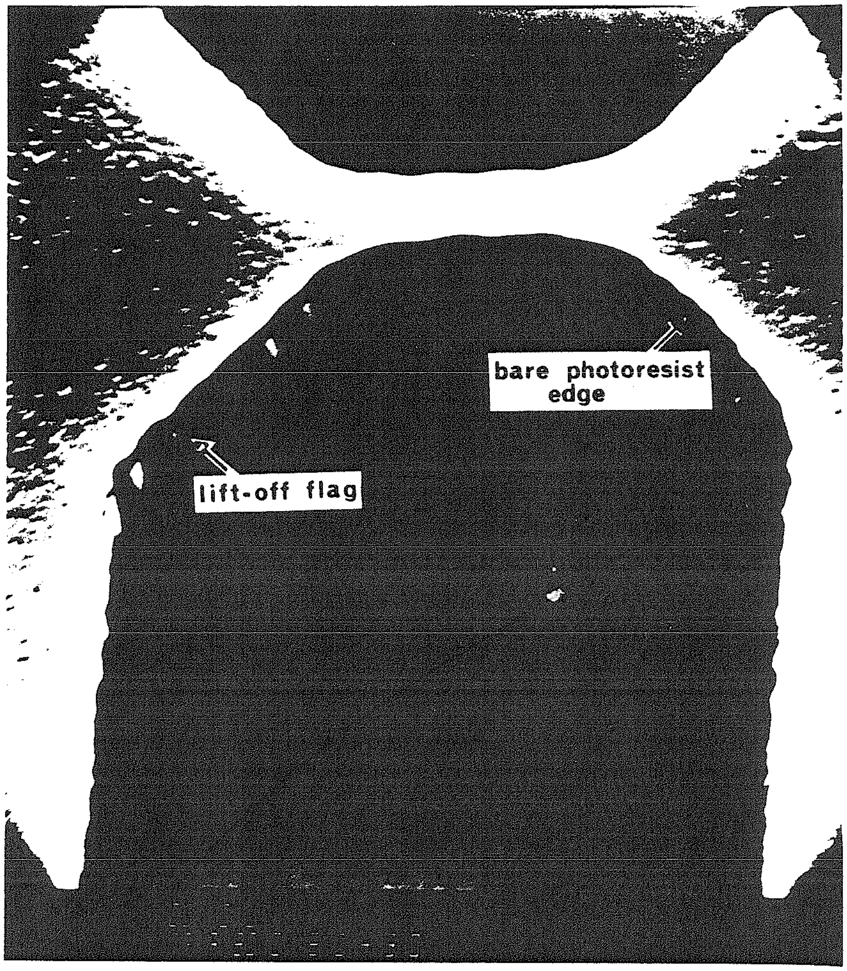

Figure 4: SEM showing the formation of a lift-off flag. The dark edge is bare photoresist shadowed by the chlorobenzene lip; the bright edge is covered with metal because the lip was too small, as in fig. 2b.

Back-Side Flood Exposure for Transparent Substrates

Perhaps one of the simplest ways to produce a reverse-taper photoresist edge profile like that in fig. 1b is the use of a back-side flood exposure. Photoresist does not expose uniformly throughout its thickness; instead a thin layer is completely exposed, bleaches, and then allows the layer underneath to expose [5]. Because of this a very short exposure through the back side of a transparent substrate will expose only a thin layer of resist directly adjacent to the substrate. The substrate is then pattern exposed as usual from the front. There are now two distinct layers, the lower flood exposed as in a conventional bi-layer resist structure (see next section), and the upper containing the pattern. When this is developed the bottom layer undercuts the top, leaving a profile that will give a good lift-off. A typical process is:

i) Spin and prebake as usual.

ii) Back-side flood expose for roughly 1/5 normal time; on our equipment 3 sec. at 300 on the exposure meter.

iii) Pattern expose for about 4/5 of normal time; 12 sec. at 300 on meter.

iv) Develop as usual, inspect for undercut, and if necessary develop again; the increase in development necessary for good undercut is usually not more than 15 sec.

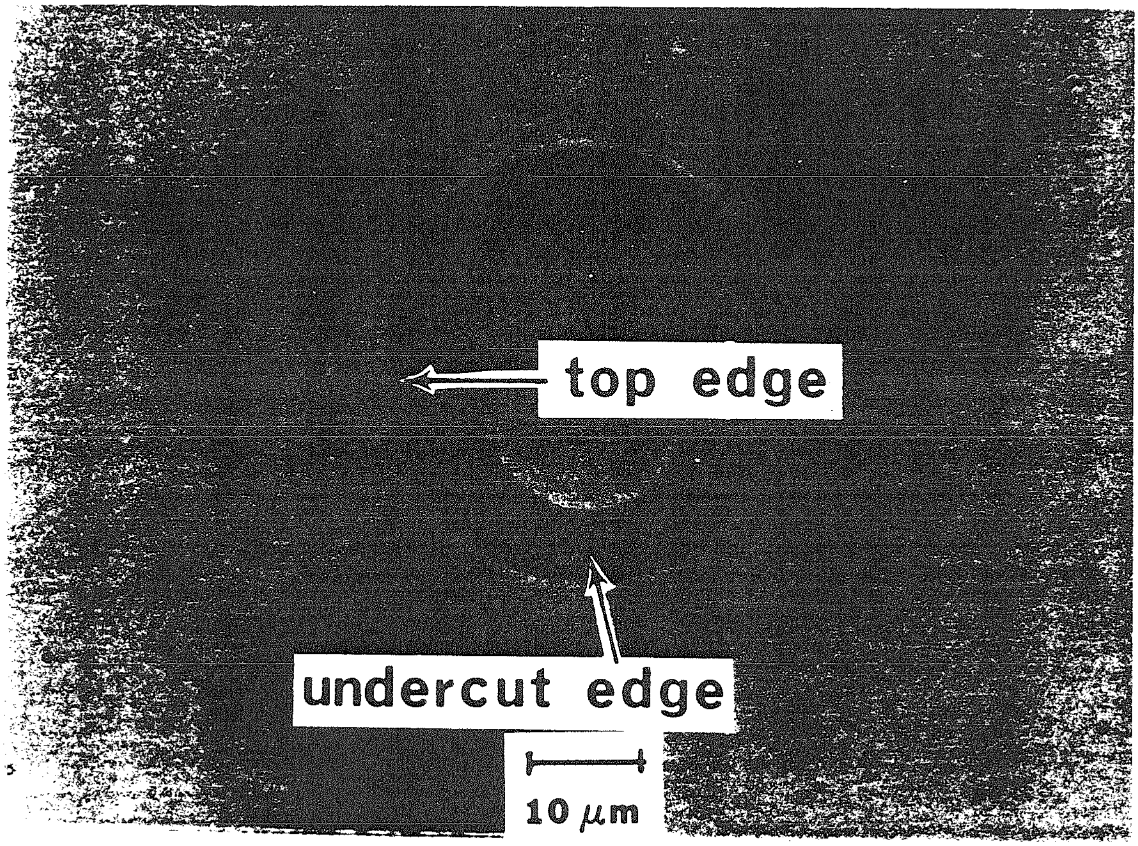

Figure 5: Photomicrograph showing the undercut edge in a back-side flood exposed pattern.

For simple lift-off processing on transparent substrates this has been found to be a very successful technique (fig. 5).

Bi-Layer Resist Processing

The chlorobenzene process produces acceptable lift-off profiles because it produces two different layers in the photoresist, effectively allowing the top layer to be undercut by the bottom layer. This undercutting could be accomplished by actually using two distinct layers, applied sequentially. The top layer would be the usual photoresist, and be patterned with standard contact printing and development. The bottom layer would then be etched through this pattern, undercutting as it etches (fig. 6). It should be noted that unless this layer is carefully chosen the problems in small geometry control inherent in wet etching mentioned earlier once again occur. Fortunately this offset layer can also be photoresist, whose etch characteristics are easily controlled. The advantages offered by lift-off patterning can be maintained, and a variety of applications unique to offset masking gained (for example, see chapter 3).

One possible choice for an offset layer is a polyimide, DuPont Pyralin 2555. This plastic is applied to the substrate by spinning in the same way as photoresist. Its thickness can be varied over a wide range (less than 0.5μm to several micrometers) by varying its viscosity and spin speed during application. With appropriate choice of curing

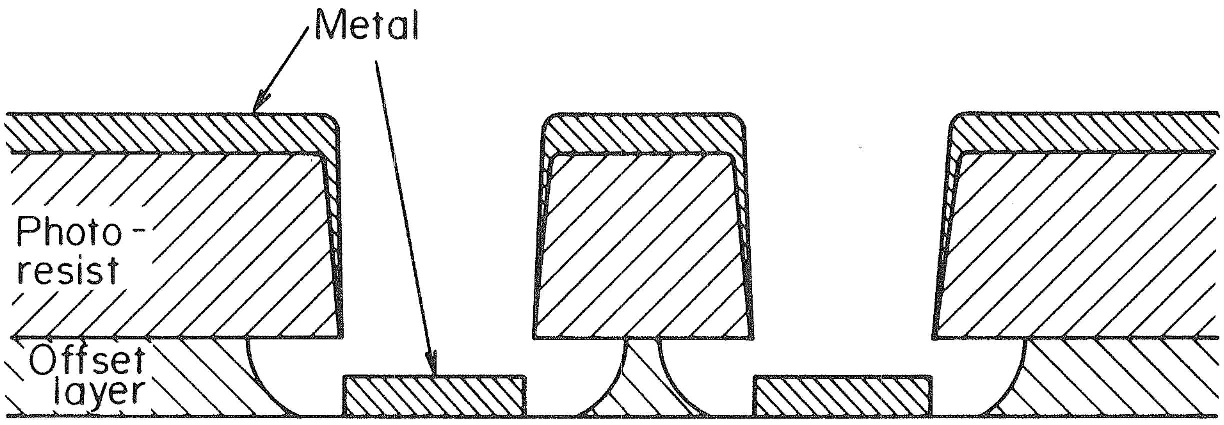

Figure 6: Bi-layer resist structure for lift-off processing.

bake time and temperature the degree of imidization can also be varied. In a partially imidized state Pyralin can be etched quite easily in sodium hydroxide, the same solution used to develop diazo-type photoresists (e.g. Shipley 1350J). It also has the necessary compatibility with the solvent system used in these resists: it is not dissolved by them when the resist is applied to the Pyralin. This allows the formation of the two distinct layers needed for the formation of a profile like that in fig. 6.

A typical processing sequence is given below using 1:1 thinned Pyralin (which produces a layer approximately 0.5μm thick):

i) Spin Pyralin: 4000rpm, 30 sec. Unlike photoresist, polyimide will still be quite fluid after spinning, so care must be used in handling the substrate.

ii) Soft Bake: 125°C, 15 min. This step must usually be optimized for a particular batch of Pyralin.

iii) Apply photoresist and pattern in the normal manner.

iv) Develop pattern and etch Pyralin: the total time required varies depending on soft-bake conditions; visual observation of the polyimide etch is usually necessary.

Figure 7 shows a bi-layer pattern using the process above. The photoresist layer is supported above the substrate by about half a micrometer. One serious problem with Pyralin

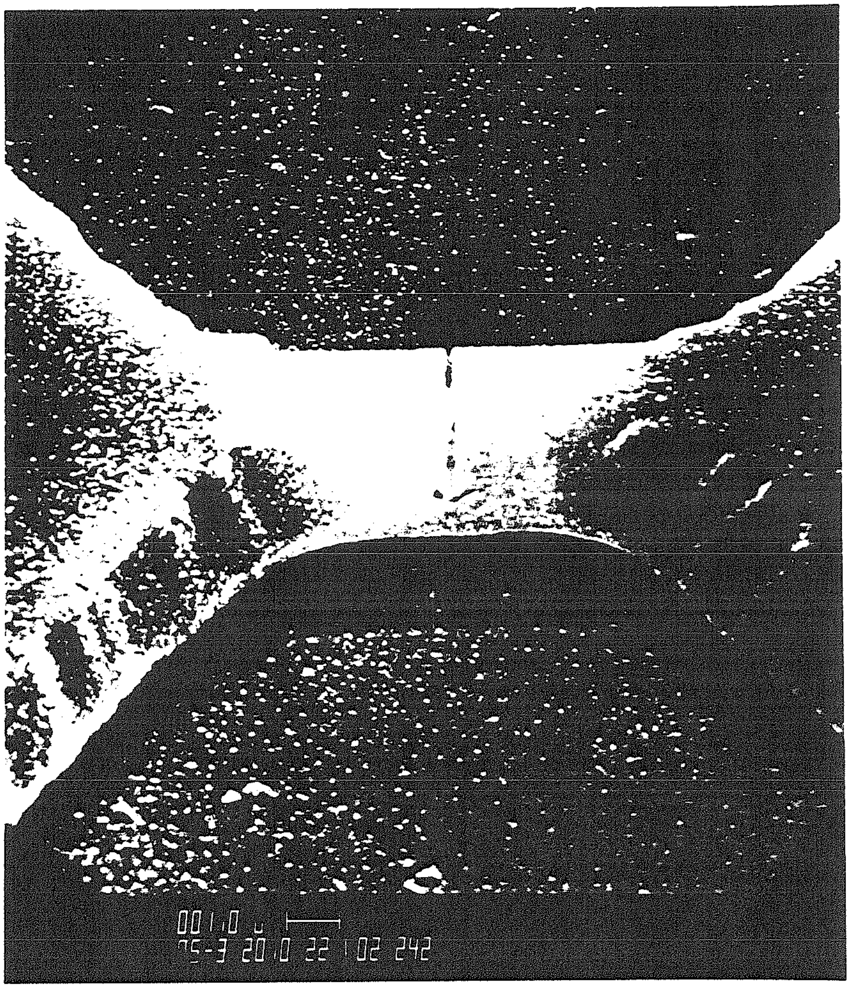

Figure 7: Photoresist pattern suspended above the substrate by a layer of polyimide.

is its tendency to swell during etching. This can often crack the photoresist above, ruining the pattern.

A much more attractive offset layer can be made with photoresist that has been uniformly exposed. This layer can then be uniformly etched, again with the same developer used on the top pattern layer. One problem that must be dealt with, however, is the dissolution of the offset layer during the application of the second layer of photoresist. Early work with these systems [6][7] prevented intermixing of the two layers by evaporating a thin layer of aluminum over the first layer of resist, and then applying the top layer of resist over the aluminum. The top layer was patterned as usual, followed by etching of the aluminum. The offset layer can then be etched by immersion in photoresist developer.

The presence of this aluminum buffer layer can in some cases be a serious disadvantage: when registration between a pattern already on the substrate and the bi-layer pattern is necessary the aluminum prevents observation of the lower level. The buffer layer now must be transparent. A process for preparing such a layer has been described [8][9] which uses a CF_4 plasma treatment to form a fluorinated hydrocarbon on the surface of the photoresist offset layer. Under proper conditions a layer approximately 30nm thick is formed in which fluorine is entirely substituted for the hydrogen originally present [9]. This layer is both insoluble and impermeable to the solvents present when the second photoresist layer is applied. It is also unaffected by the resist developer, and so serves as an etch stop during development of the pattern layer.

The strength and integrity of the CF_4 formed buffer layer is actually quite impressive. It is clearly visible in the SEM of fig. 8 on a substrate that has been through a complete lift-off process (including a very vigorous immersion in acetone). Once a layer of photoresist has been treated it can be immersed in acetone for at least 30 seconds before any effect can be seen. Unfortunately the layer also exhibits another characteristic of fully fluorinated hydrocarbons: it is extremely difficult to get anything to adhere to it. Since another layer of photoresist must be applied over it this adhesion problem is corrected with another plasma treatment. Using a short N_2 plasma it has been found that a small fraction of the surface bonds are once again C-H structures, although very little nitrogen is incorporated [9]. The precise mechanism for this adhesion promotion step remains obscure, but on empirical grounds it works very well. Applying photoresist to a buffer layer untreated by the nitrogen usually leaves no resist behind at all after spinning. When applied to a treated layer, however, the result is a typical uniform layer of resist.

The successful formation of a CF_4 induced buffer layer has been found to be very sensitive to the plasma processing environment. The plasmas used in this study were all formed in a Tegal Plasmod, a small (10cm diameter) barrel reactor,

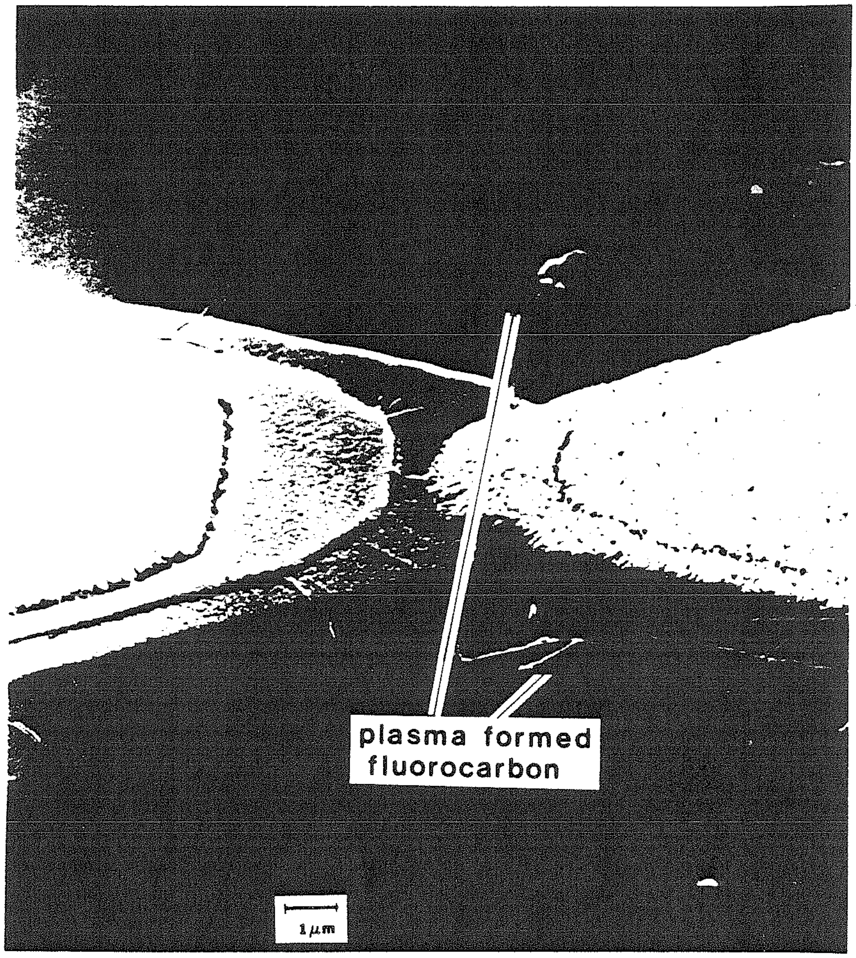

Figure 8: Residue of CF_4-plasma formed buffer layer. The film was left on the substrate even after vigorous agitation in acetone.

at gas pressures between 600mTorr and 700mTorr, and an RF power of about 30 watts. The integrity of the buffer layers formed (on flood exposed 1350J resist) was evaluated by immersion in resist developer; good layers prevent any development for at least 60 seconds. The following aspects have the most pronounced effects:

i) A CF_4 plasma in the standard all glass Plasmod chamber produced very poor layers. A simple liner of Teflon in the outer vacuum vessel and removal of the inner glass cylinder (using a flat Teflon plate to close the vacuum vessel) produced excellent buffer layers. The removal of the glass cylinder decreased the total glass surface area exposed to the CF_4 plasma by about 2/3, which should increase the amount of free fluorine present, thus producing more uniform layers.

ii) The sample position in the plasma is also important. The Plasmod produces a fairly non-uniform plasma environment, with the center region apparently the least excited (using the intensity of optical radiation from the plasma as a measure of excitation). Since the reaction proposed by Dobkin and Cantos [9] relies on fluorine diffusion into the resist they recommend ion bombardment of the sample be avoided. This is most easily done near the center of the chamber, and samples placed there produce the most uniform layers.

iii) The presence of oxygen in the plasma has a very destructive effect since it etches both the fluorinated and unfluorinated photoresist. A leak free vacuum vessel and an extensive CF_4 purge before striking the plasma are therefore essential. An N_2 flush must also precede the N_2 plasma treatment for the same reason.

With the preceding precautions excellent buffer layers have been routinely formed. A typical processing sequence is given below:

i) Spin first photoresist layer; usually 1350J or 1350B.

ii) Prebake: 85°C, 25 min.

iii) Flood expose: 60 sec.; this is about a four times overexposure with our equipment, and will give a rapid undercut rate; lower exposures give lower undercut rates.

iv) CF_4 treatment: in Teflon chamber as noted earlier; flush with CF_4 at 650mTorr for at least 5 min., followed by CF_4 plasma for 3 to 5 min., 1/3 power, 650mTorr.

v) N_2 treatment: remove Teflon liner and replace sample in usual Pyrex chamber; flush with N_2 at 650mTorr, 10 min., followed by N_2 plasma at 650mTorr, 1/2 power, 30-45 seconds.

vi) Apply second (patterning) photoresist layer: normal process and prebake.

vii) Expose pattern: normal time, usually 15 sec. at 300 on exposure meter.

viii) Develop pattern layer: Microposit developer diluted 1:1 with water, 35-45 sec.

ix) Strip buffer layer: in O_2 plasma, 650mTorr, 1/3 power, 4 min.

x) Etch bottom (offset) layer: Microposit developer diluted 1:1 with water, usually for 30 sec. if offset layer is 1350J, or 10-15 sec for 1350B. This time should be optimized to achieve the desired degree of undercut. With 1350B as the offset layer the undercut can easily be held to 2-4μm.

This process has proved to be invaluable in the fabrication of microbolometers, and is used routinely to form a variety of photoresist bridge structures (see fig. 7 and fig. 9, chapter 3).

When patterns containing very small, isolated patches of photoresist are necessary it may be difficult to prevent complete undercutting with the process described above. One way to avoid this is to use an offset layer with higher UV sensitivity and faster development rate than the top patterning layer [8]. When the pattern is exposed the edges of the top layer receive too little energy for adequate exposure, but the higher sensitivity layer below receives enough. When the pattern is developed and etched as described above a small undercut is produced. Here the size of the undercut is limited by the actual dimensions on the mask, preventing complete undercutting of small features. With the use of the fluorinated buffer layer process, this is another example of the various combinations possible.

Angle-Evaporated Narrow Lines

As a final example of a bi-layer resist application, we describe the fabrication of narrow, evaporated metal lines. With this process it is possible to form lines much narrower than the minimum lithographic line-width, and if desired, very small junction areas between two lines. Figure 9 illustrates how this is done. A bi-layer resist is first applied to the substrate, with the bottom layer uniformly flood-exposed. A narrow line is then exposed in the top masking resist, followed by development and undercutting by the bottom layer. If material is now evaporated at a steep angle to the substrate, metal is deposited on the substrate only through the 'shadow' of the mask opening (see fig. 9). For a mask layer thickness t, mask line opening w, and evaporation angle θ (measured from the substrate normal), the metal linewidth d is

$$d = w - t \tan\theta \quad . \tag{1}$$

In order to fabricate small area junctions (for instance, for tunnel-junction detectors) the substrate is rotated 90° after the first evaporation. A second evaporation is then performed through another mask opening that is perpendicular to the first line (fig. 10).

This process has been used to fabricate aluminum-aluminum oxide-aluminum tunnel junctions with junction areas of 1-0.25 $(\mu m)^2$. For a typical photoresist thickness t of

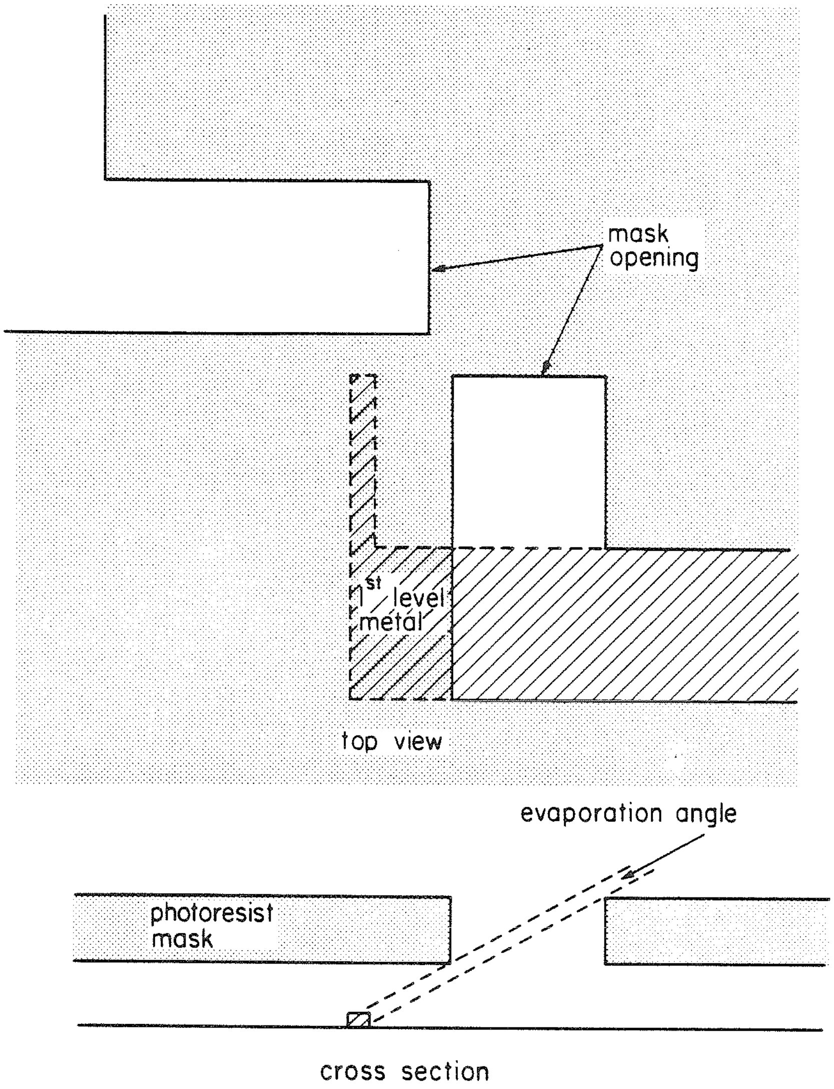

Figure 9: Top and cross-sectional views illustrating the formation of narrow metal lines by evaporating through a photoresist mask.

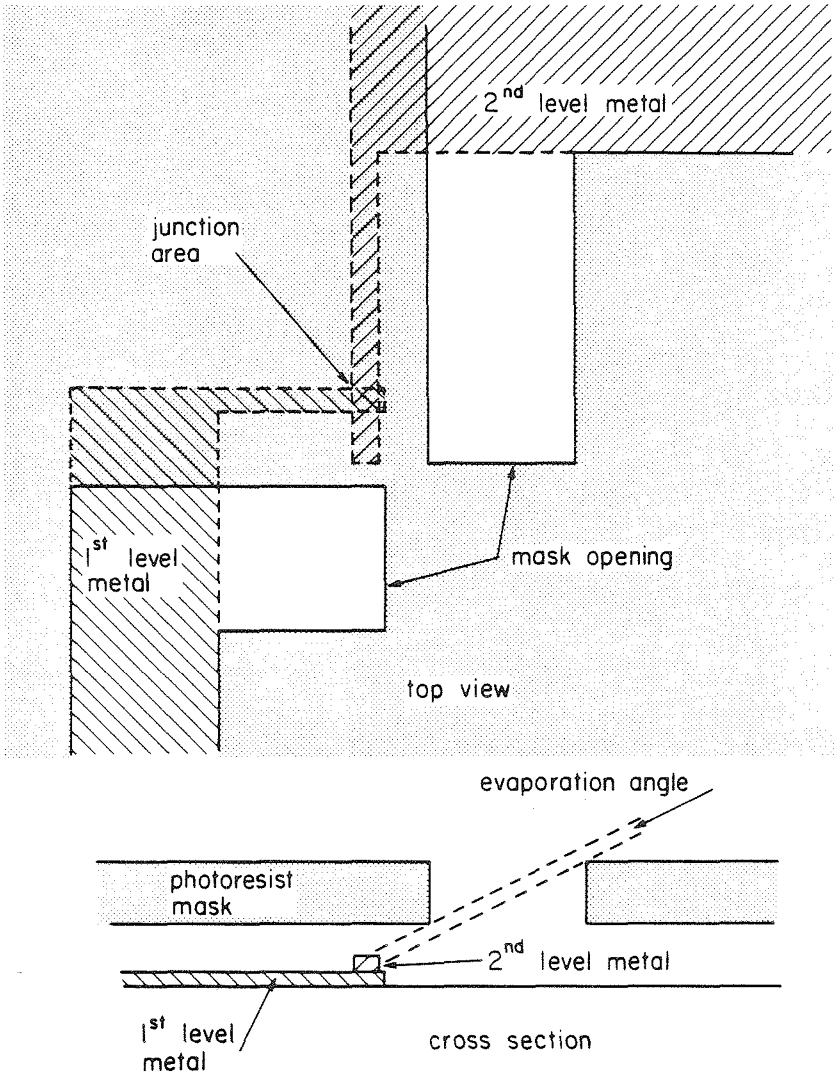

Figure 10: Second step in the evaporation to form a small area overlap between two lines. The top view is rotated 90° relative to fig. 9.

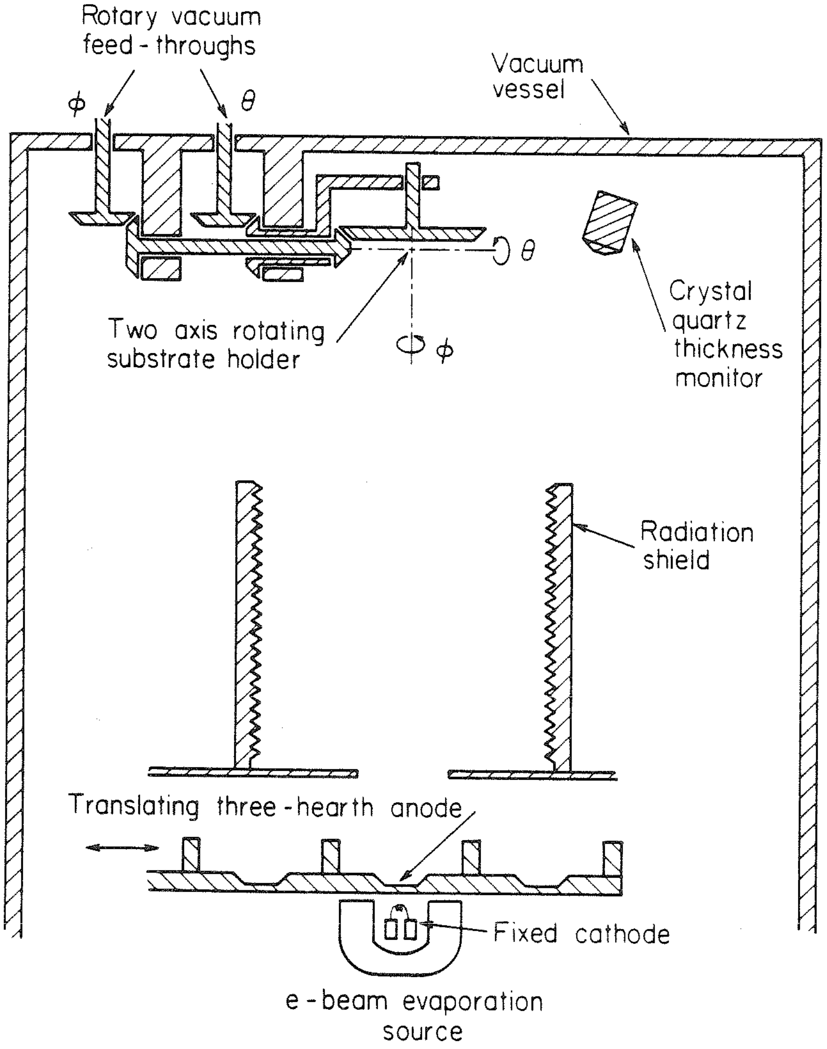

Figure 11: Evaporation system and substrate fixture used to form the small area junctions.

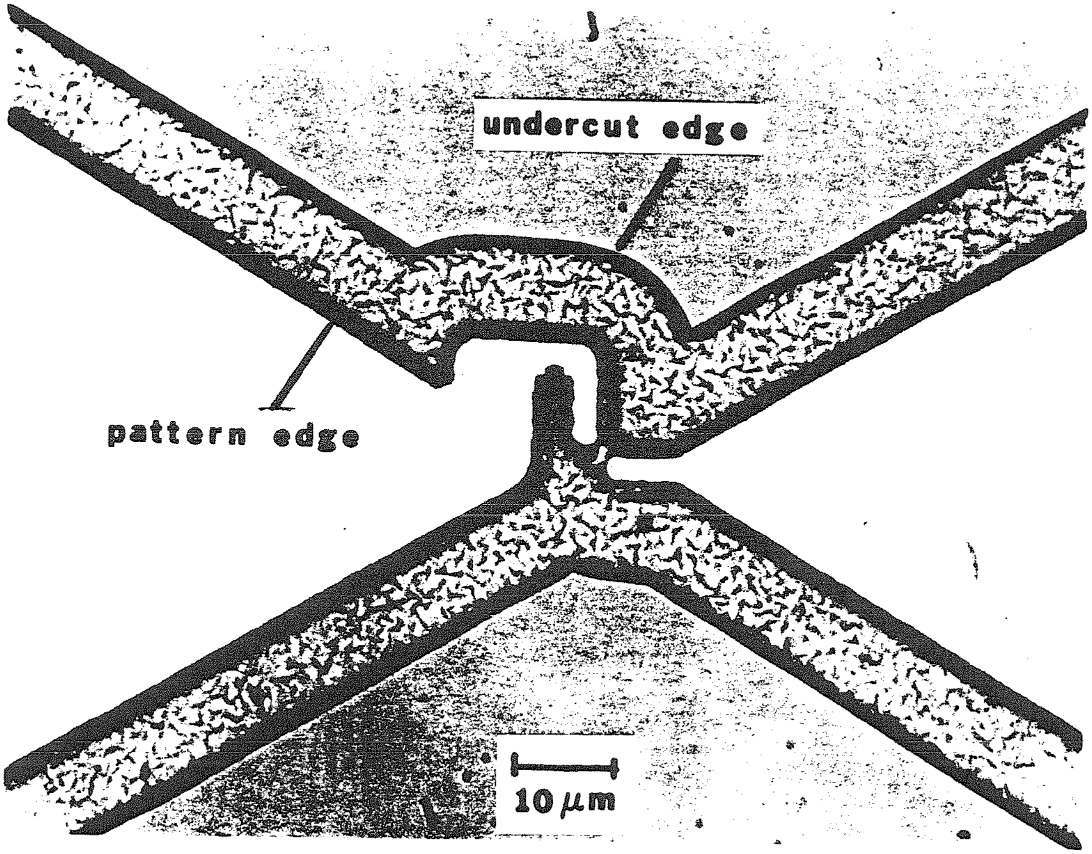

Figure 12: Photomicrograph of the photoresist pattern used to fabricate the small area junctions.

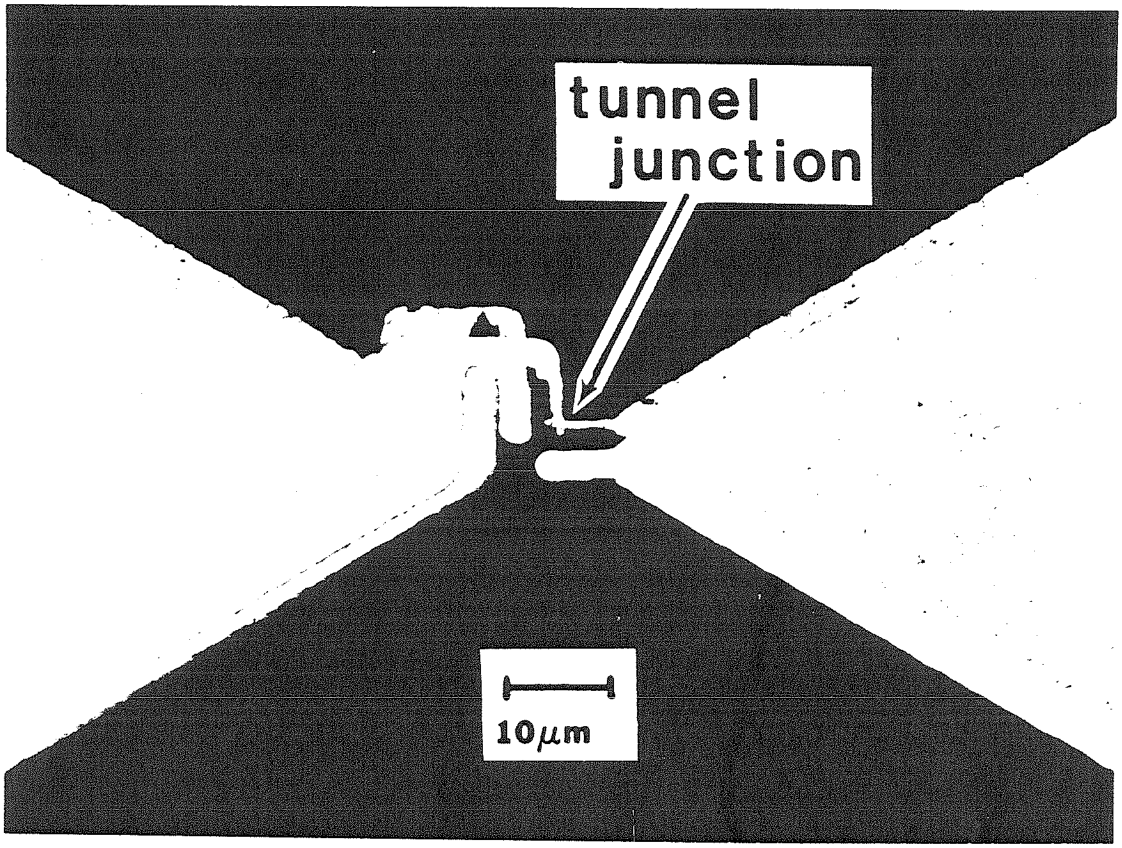

Figure 13: Photomicrograph of a finished tunnel junction fabricated with the angle evaporation technique.

1.75μm and minimum linewidth w of 3μm, an angle of 55° gives a metal linewidth of 0.5μm. Using the vacuum evaporation system shown in fig. 11, it is possible to complete the entire device in a single sequence. The first layer of metal is evaporated (100nm Al) and then 500mTorr of dry oxygen is introduced into the system. After a 30min. oxidation step the system is re-evacuated, the substrate rotated 90° (using the ϕ-axis rotary feedthrough), and the second layer of metal evaporated (another 100nm of Al). A photomicrograph of a typical photoresist pattern is shown in fig. 12, and the resulting device in fig. 13.

References

[1] Flamm, D., V. Donnelly, and D. Ibbotson, 'Basic chemistry and mechanism of plasma etching,' J. Vac. Sci. Technol. **B 1**, 23 (1983).

[2] Frary, J., and P. Seese, 'Lift-off techniques for fine line patterning,' Semiconductor International, Dec. 1981, 72-88.

[3] Hatzakis, M., B.J. Canavello, and J.M. Shaw, 'Single-step optical lift-off process,' IBM J. Res. Develop. **24**, 452-460 (1980).

[4] Halverson, R., M. MacIntyre, and W. Motsiff, 'The mechanism of single-step liftoff with chlorobenzene in a diazo-type resist,' IBM J. Res. Develop. **26**, 590-594 (1982).

[5] Dill, F.H., W.P. Hornberger, P.S. Hauge, and J.M. Shaw,

'Characterization of positive photoresist,' IEEE Trans. Electron Devices **ED-22**, 445 (1975).

[6] Dolan, G., 'Offset masks for lift-off photoprocessing,' Appl. Phys. Let. **31**, 337 (1977).

[7] Dunkleberger, L., 'Stencil technique for the preparation of thin-film Josephson devices,' J. Vac. Sci. Technol. **15**, 88 (1978).

[8] Li, C., and J. Richards, 'A high resolution double layer photoresist structure for lift-off technology,' International Electron Devices Meeting, Wash.,D.C., Dec. 8-10, 1980, 412-414.

[9] Dobkin, D.M., and B.D. Cantos, 'Plasma formation of buffer layers for multilayer resist structures,' IEEE Electron Devices Lett. **EDL-2**, 222 (1981).

Chapter 5

Future Work in Far-Infrared Detectors

There has been much recent progress made in the area of far-infrared detection. Despite this, the field is still relatively young, and much work remains to be done. For instance, there are several areas where real improvements can be made in microbolometer performance. Perhaps the most obvious way to do this is by making the bolometers smaller; this requires the use of somewhat more sophisticated photolithographic techniques. The thermal model for the air-bridge predicts a significant improvement in speed if the minimum feature size is reduced from about 4µm to only 1µm. Since the speed scales like $1/\ ^2$, a 1µm air-bridge should be sixteen times faster (about 1.6MHz) than the device in chapter 3, with no decrease in the low frequency responsivity. In addition, for these smaller dimensions the performance of a polyimide-supported bolometer should be even closer to the air-bridge. Polyimide-supported detectors 2.5µm square have been made, which gave a low frequency responsivity of 100V/W, and an NEP of $3.2 \times 10^{-11} W(Hz)^{-1/2}$ at 100kHz [1].

The techniques used to fabricate air-bridge microbolometers could also be improved. At present, the process involves the flood exposure of one layer of photoresist without exposing another layer beneath it. This is quite difficult, and the yield of good resist bridge structures is quite low. To solve this problem, a material for the second layer should be used which is easily etched without requiring flood exposure. One possibility is a layer which is chemically similar to exposed positive photoresist: a Novolak-type resin (such as AZ Protective Coating made by American Hoechst Corporation) containing indenecarboxylic acid (the major product formed when the photoactive component in positive resist is exposed [2]).

Another way to improve microbolometer sensitivity would be through the use of materials with a larger figure of merit $\alpha\sigma/K$. I have only discussed the cases for elemental conductors and common semiconductors. There are other compound materials, however, which may have significantly larger values of $\alpha\sigma/K$. For example, vanadium dioxide, which undergoes a semiconductor-metal phase transition at about $60^{\circ}C$, has an extremely large temperature coefficient of resistance α at the transition, and its use as a thermal detector has been proposed in the past [3]. The electrical conductivity of this material may be too low, however, to allow efficient coupling to an antenna. If this is the case, a composite structure could be used [4]. Here the antenna would be coupled to an appropriate terminating resistance (perhaps a bismuth strip) which would act as an absorber of the far-infrared radiation. The VO_2 would be in intimate thermal contact with the absorber, and measure its temperature change. Care must be taken to avoid increasing the thermal conductance of such a structure because of the corresponding increase in the fluctuation limited noise equivalent power. Nonetheless, such a material may allow the fundamental limits for the microbolometer to be reached.

Besides room temperature microbolometers, there are a variety of other detectors which could be antenna coupled. For instance, two types of tunnel junctions have been studied extensively: the metal-oxide-metal (MOM) junction [5], and the superconductor-insulator-superconductor (SIS) junction [6][7][8][9]. These devices do have parasitic capacitance, and so must have very small areas. By using the angle evaporation technique described in chapter 4, perhaps in conjunction with an edge-type junction [5], detectors small enough to work at frequencies above 300GHz might be made. The SIS junction could provide very sensitive detection in the millimeter range; its performance at submillimeter wavelengths is unknown.

A final example of an antenna coupled detector is a variation of the superconducting transition-edge bolometer. The basic idea is to use the very large temperature coefficient of resistance of a superconductor operated near its transition temperature. The use of such bolometers is well established, and has been used in a composite structure for submillimeter detection [10]. It should be possible, however, to directly couple the bolometer to an integrated antenna. If the device is close to its transition temperature the gap frequency will be quite small, and it will not really appear as a superconductor at far-infrared frequencies. The resistive part of the bolometer impedance will cause heating to occur when the FIR power is applied, and the subsequent temperature rise detected. Such a self-heated transition-edge bolometer could be very sensitive, and operate throughout the far-infrared.

References

[1] Neikirk, D.P., W. Lam, and D.B. Rutledge, 'Far-infrared microbolometer detectors,' submitted for publication, Int. J. Infrared Millimeter Waves.

[2] Pacansky, J., and J.R. Lyerla, 'Photochemical decomposition mechanisms for AZ-type photoresists,' IBM J. Res. Develop. **23**, 42 (1979).

[3] Jelks, E.C., R.M. Walser, R.W. Bené, and W.H. Neal II, 'Response of thermal filaments in VO_2 to laser-produced thermal perturbations,' Appl. Phys. Lett. **26**, 355 (1975).

[4] Nishioka, N.S., P.L. Richards, and D.P. Woody, 'Composite bolometers for submillimeter wavelengths,' Applied Optics **17**, 1562 (1978).

[5] Heiblum, H., S. Wang, J.R. Whinnery, and T.K. Gustafson, 'Characteristics of integrated MOM junctions at dc and at optical frequencies,' IEEE J. Quantum. Electron. **QE-14**, 159 (1978).

[6] Dolan, G.J., T.G. Phillips, and D.P. Woody, 'Low-noise 115-GHz mixing in superconducting oxide-barrier tunnel junctions,' Appl. Phys. Lett. **34**, 347 (1979).

[7] Irwin, K.E., S.E. Schwarz, and T. Van Duzer, 'Planar antenna-coupled SIS devices for detection and mixing,' 6th Int. Conf. Infrared Millimeter Waves, IEEE cat. no. 81CH1645-1 MTT, M-4-2 (1981).

[8] Habbal, F., W.C. Danchi, and M. Tinkham, 'Photon-assisted tunnelling at 246 and 604 GHz in small-area superconducting tunnel junctions,' Appl. Phys. Lett. **42**, 296 (1983).

[9] Danchi, W.C., F. Habbal, and M. Tinkham, 'ac Josephson effect in small area superconducting tunnel junctions at 604GHz,' Appl. Phys. Lett. **41**, 883 (1982).

[10] Clarke, J., G.I. Hoffer, P.L. Richards, and N.-H. Yeh, 'Superconductive bolometers for submillimeter wavelengths,' J. Appl. Phys. **48**, 4865 (1977).